



Università degli Studi di Trento

Scuola di Dottorato in Fisica

XXV Ciclo

Second order nonlinear optical phenomena in strained silicon waveguides

PhD Candidate: **Federica Bianco**

Supervisor: **Prof. Lorenzo Pavesi**

Anno Accademico 2011/2012

*This work is licensed under the
Creative Commons Attribution Non-commercial No Derivatives 3.0 Unported
(CC BY-NC-ND 3.0)
To view a copy of this license, visit
<http://creativecommons.org/licenses/by-nc-nd/3.0/>*



To Pietro, papà, mamma and Francesca.

Contents

Acknowledgements	1
Introduction	3
1 Strained silicon waveguides: fabrication and description	10
1.1 Strained silicon waveguide used for stress characterization and in the first SHG experiment	10
Insertion losses characterization	13
1.2 Strained silicon waveguide in the second SHG experiment	16
Insertion losses characterization	19
2 Mechanical characterization of silicon crystalline structure	20
2.1 Definition of stress and strain tensors	21
2.2 Mechanical stress in thin films	23
2.2.1 Thin films stress model	24
2.2.2 Stress origins in thin films	25
2.2.3 Examples of stress measurement techniques	30
2.3 Micro-Raman spectroscopy for stress measurements	32
2.3.1 General theory of micro-Raman spectroscopy for stress measurements	34
2.3.2 Theoretical model for stress measurements in silicon waveguide	37
2.3.3 Description of stress measurements method	40
A. Experimental and data analysis procedure	40

B. Stress tensor determination accuracy	43
2.4 Stress characterization experimental results	45
2.4.1 Unpolarized measurements	46
2.4.2 Polarized measurements	48
2.5 Conclusions	50
3 Second harmonic generation in strained silicon waveguides	53
3.1 Introduction to nonlinear optics	54
3.1.1 Properties of the nonlinear susceptibility	59
3.2 Introduction to second harmonic generation	61
3.3 Second harmonic generation from silicon surface	68
3.4 Second harmonic generation in strained silicon waveguides: experi- mental results	73
3.4.1 Experimental set-ups	73
A. Fundamental signal at ns regime	73
B. Fundamental signal at fs regime	74
3.4.2 Second harmonic generation results: first experiment	76
3.4.3 Second harmonic generation results: second experiment	81
3.5 Conclusions	86
4 Second order nonlinearity: analysis and discussion	89
4.1 Analysis of possible modal phase matching	89
4.2 Theoretical analysis of conversion efficiency	93
4.3 Conclusions	98
Conclusions	100
A Experimental characterization of the laser source	103
A.1 Beam waist and divergence	104
A.2 Pulse duration	107

B	Experimental characterization of the detection system	110
B.1	F/# matcher	110
B.2	Spectral response	113
B.3	Spurious signals	118
B.4	Conversion factor from a.u. to Watts	119
C	Experimental characterization of the principal optical elements	121
C.1	Neutral optical filters characterization	122
C.2	Reflective objective characterization	123
	Bibliography	130

Acknowledgements

The work carried out in this thesis has been supported by the FU-PAT (Provincia Autonoma di Trento) project NAOMI and by a grant from Fondazione Cariplo no 2009-2730.

I would like to thank my supervisor Prof. L. Pavesi for the precious support during my PhD training and the period spent at the Univeristy of Trento, for his passion for the research activity, for his helpfulness despite of his very busy agenda and for giving me the opportunity to work in his group.

I would like to thank all the researchers whom I have collaborated with: Dr. M. Cazzanelli, Dr. M. Ghulinyan, Mr. C. Schriever, Dr. E. Moser, Dr. A. Yeremyan, Dr. B. Dierre, Dr. K. Fedus, Dr. F. Enrichi, Dr. R. Pierobon, Dr. G. Pucker, Dr. E. Degoli, Dr. E. Luppi, Dr. D. Modotto, Prof. S. Wabnitz, Prof. S. Ossicini, Prof. H. K. Haugen and Prof. R. Morandotti.

I would like to thank all the guys of the Nanoscience Group: Andrea, Nikola, Tanya, Paolo, Laura, Mattia, Alessandro, Eveline, Fernando, Fabrizio, Romain, Philip, Oleksiy, Curro, Massimo and Davide for the support, the sympathy and the funny times spent together.

*Let us be grateful to people who make us happy;
they are the charming gardeners who make our souls blossom.*

(Marcel Proust)

A hearty thanks to Ilaria and Alessandra, who have made me appreciating the life here in Trentino.

A particular thanks to Tanya for the great support she has shown me in the sad moments!

A special thanks to Andrea and Riccardo (Ilrota) for their precious friendship, their help to recover my smile in the difficult moments and in general for the happy moments spent together! Thanks guys!!!

I would like also to thank my Canadian friends, who have made my stay in Canada an unforgettable adventure! Thanks Dom(ingo)enico, Manoj, Melanie, Mehrnoosh, Sze Phing, Cathy, Eugene, Kevin, Run, Semen, Obi, Romain, Lee-Anne... and of course Pantoufle!!!

Finally, but not last at all, a very hearty thanks to my family for supporting and motivating me every moment of my life and to Pietro for his infinite patience, the immense support, the encouragement and the magic moments spent together in these three years!

Introduction

Thanks to extensive efforts spent by academic and industrial researchers all around the globe, silicon photonics is a constantly growing technology. Its many applications in diverse research fields, such as photonic interconnect, telecommunication, data communication, nonlinear optics, signal processing, biosensing, etc., have determined the development of many high performance photonic devices over the last fifteen years [1–11]. The high compatibility with the mature complementary metal-oxide semiconductor (CMOS) technology offers, in fact, the advantage of reliable manufacturing with nanoscale precision and guarantees the necessary versatility which allows building silicon photonic devices with complex functionalities. Nowadays, the list of silicon photonic devices comprises a high variety of functionalities, which include the detection (e.g. thanks to high-performance germanium-on-silicon photodetectors or avalanche photodetectors [5]), modulation (e.g. thanks to carrier-based, active high speed ring resonator or photonic-crystal-based slow-light Mach-Zehnder interferometer modulators [4]) and lasing/amplification (e.g. thanks to silicon Raman laser, germanium on silicon and hybrid silicon microring and microdisk laser [3]).

A relevant contribution in the explosion of the silicon photonics has come from its nonlinear optics branch (the nonlinear silicon photonics). This research area exploits the tight confinement of the light, allowed by the high contrast index in the silicon sub-micron-structures, and the large third order nonlinearity of silicon to realize novel active devices on the chip scale. For example, silicon exhibits a Kerr coefficient and a Raman gain that are more than 100 and 1000 larger than

in silica in the telecommunication band, respectively [12–14]. Therefore, the high variety of nonlinear optical phenomena offered by silicon enables the realization of devices with functions such as amplification and lasing, wavelength conversion and all-optical processing [6]. For example, the high Raman gain has been exploited for the light amplification both at telecommunication [12, 15–18] and mid-infrared [19] wavelength region and in the realization of lasing silicon devices [20, 21]. In fact, in addition to the nanostructured silicon approach [22, 23], the Stimulated Raman Scattering (SRS) is currently considered one of the possible solutions to the silicon drawback represented by the indirect band gap, which inhibits an efficient spontaneous light emission and thus the fabrication of silicon-based lasers. Instead, the Kerr effect has been applied in optical phase modulation [24, 25] and supercontinuum generation, where a spectral width beyond 350 nm has been demonstrated [26–28]. Furthermore, by making use of four-wave-mixing (FWM) broadband light amplification [29, 30] and frequency conversion [31–34] have been also demonstrated.

However, despite of the plenty of nonlinear optical phenomena, silicon lacks a fundamental nonlinearity, the second order nonlinear response. In fact, owing to the inversion symmetry of its crystalline structure, silicon is characterized by a zero bulk second order nonlinear susceptibility ($\chi^{(2)}$) in electric-dipole approximation. As a consequence, essential nonlinear phenomena such as sum- or difference frequency generation (SGF, DFG) for the generation of new spectral components (especially in the mid- and far-infrared via DFG) and Pockels effect are forbidden. In particular, Pockels effect would allow the electro-optical modulation and, thus, the fabrication of modulators that do not suffer from the limitations imposed by the carrier-related speed. Considering also that third order nonlinear-loss mechanisms, such as two-photon absorption (TPA) and two-photon induced free-carrier absorption (TP-induced FCA), compete and, in some cases, become obstacles for the aforementioned third order nonlinear effects, a second order nonlinearity in bulk silicon would be highly preferable.

The necessary condition to have a bulk second order nonlinear response in silicon

is the breaking of its centrosymmetry. This can be obtained by deforming the crystalline structure, for example, by means of a mechanical strain. In microelectronics, the impact of mechanical strain on the silicon electronic properties is a well known effect. In fact, thanks to its influence on the energy band structure and the carrier mobilities [35–38], the strain is currently used to enhance and tune the properties of MEMS (Micro Electro-Mechanical Systems) and CMOS devices [39]. In addition, strain also modifies the linear optical properties of photonics devices [40, 41] by inducing the birefringence in waveguiding structures. Strained-induced birefringence can be used, for example, for polarization independent or polarization splitting photonic components [2].

Nevertheless, probably the most relevant effect of the strain has been observed on the second order nonlinear optical properties of silicon devices.

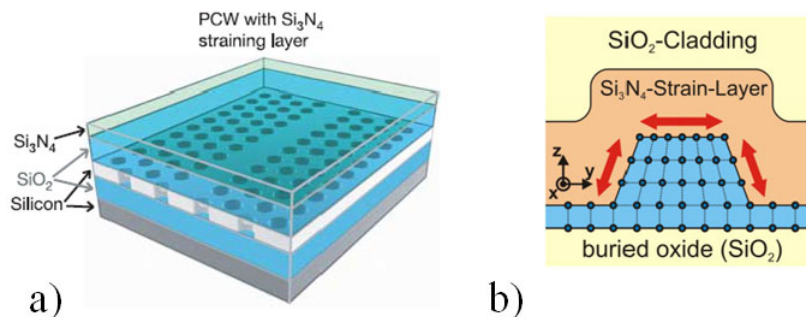


Figure 1: Silicon electro-optic modulators: a) demonstration structure used in [42]; b) demonstration structure used in [43].

In fact, in 2006, thanks to the deposition of a stressing layer on the active part of a silicon device, the linear electro-optic effect has been observed for the first time, allowing the demonstration of the first silicon electro-optic modulator [42]. The demonstration of the electrically-induced change of the silicon refractive index has been achieved in Mach-Zehnder interferometer made by inhomogeneously strained slow light photonic crystal waveguides (Fig. 1.a). The induced material second order nonlinearity has been deduced from the measurements of the $\chi^{(2)}$ enhancement ($\chi_{\text{enh}}^{(2)}$) caused by the enlarged group index of the structure ($\chi_{\text{enh}}^{(2)} = n_g \chi^{(2)} / n$, where n_g is the

group index and n is the silicon refractive index) [42]. Two different structures have been investigated. In the first sample the strain has been applied by a compressive stressing layer of silica and a small $\chi_{\text{enh}}^{(2)}$ has been observed and quantified as high as 60 pm/V. In the second structure, instead, a tensile stressing silicon nitride layer deposited on top of the silica layer has produced a $\chi_{\text{enh}}^{(2)} \sim 830$ pm/V, corresponding to a material $\chi^{(2)} \sim 15$ pm/V. More recently a further improvement of strained silicon Mach-Zehnder interferometer has been reported in [43], where rib waveguides have been directly strained by a tensile silicon nitride layer, that completely covers the structure (Fig. 1.b), achieving a refractive index change of 2.4×10^{-5} at 30 V modulation voltage, that corresponds to a $\chi^{(2)} \sim 122$ pm/V.

The natural step forward beyond the electro-optic modulation is then represented by the possibility to achieve a frequency conversion via $\chi^{(2)}$ processes in all-silicon devices. This thesis has the general goal to demonstrate the possibility to perform an all optical experiment of frequency conversion by making use of the second order nonlinear response induced in strained silicon waveguides.

Based on an idea similar to the one proposed by [42], silicon-on-insulator (SOI) waveguides have been mechanically deformed by using a stressing cladding layer deposited on the waveguide core. Although the strain is expected to be inhomogeneous inside the waveguide, its actual distribution has been never directly measured. In this thesis the mechanical characterization performed by micro-Raman spectroscopy has allowed to reconstruct for the first time the two dimensional spatial distribution of the strain across the waveguide cross-section and study its inhomogeneity by varying the stress exerted by the cladding overlayer.

The demonstration of the frequency conversion process via strain-induced $\chi^{(2)}$ has been accomplished by means of experiments of Second Harmonic Generation (SHG), that have allowed to estimate the order of magnitude of the induced effective $\chi^{(2)}$ (~ 40 pm/V). Moreover, the influence of the strain and the specific properties of the stressing layer has been experimentally investigated and theoretically analyzed, pointing out the strict dependence of the $\chi^{(2)}$ on the extent and inhomogeneity of

the strain field.

Due to the complexity of the experimental set-up used in the SHG experiment at fs regime, a careful characterization has been carried out in order to set the apparatus for reliable measurements and avoid artifacts or unwanted contributions originated by inappropriate set-up conditions.

In Chapter 1 the strained silicon waveguides involved in the various experiments are presented. In particular, the device fabrication, the geometry and the optical properties of samples are illustrated. Since various samples have been produced, they are described by dividing them in two main categories, according to the experiment where they have been employed.

Chapter 2 is devoted to the mechanical characterization of the strain field in the cross-section of the strained silicon waveguides. In particular, a brief overview on the mechanical stress in thin film is given, introducing the concept of stress and strain tensors and the mathematical model, that describes the stress in thin films. Moreover, the stress origins and its effects on a thicker substrate are explained. Before describing in detail the stress measurements by micro-Raman spectroscopy, two common techniques for the stress determination in thin film are illustrated. Afterward, the general theory of micro-Raman spectroscopy concerning stress measurements is reported in detail, which is then applied to the specific crystallographic orientation of the waveguide silicon used in this thesis. Finally, the experimental method, the data analysis and the experimental results are presented and discussed.

In Chapter 3 the experimental results of all optical SHG experiments carried out in strained silicon waveguides are presented. Before discussing the experimental results, a brief introduction on the basic concepts of the nonlinear optics and the second harmonic generation process are discussed, as well as the problem of the material dispersion for the conversion efficiency and the relative common solutions. Moreover, a brief overview of the SHG process on silicon surface reported in literature is given, focalising in the enhancement of the second harmonic signal by means of mechanical stress. Finally, the details of the set-ups and the experimental results

are presented and discussed.

Chapter 4 has the goal to present generical theoretical studies for a better comprehension of the second order nonlinear response induced in strained silicon waveguides. Particularly, the studies explore the possibility of an intrinsic phase-matching mechanism arising from the multimodal property of the measured waveguides and investigate the influence of the strain distribution in the conversion efficiency of the SHG process.

Finally, a general overview of the results achieved in this thesis and the perspectives for future works are given in the Conclusions chapter.

In Appendix A the experimental results on the characterization of the laser source are presented, describing the experimental methods and reporting the estimation of both beam waist radius and temporal width of the pulses of the fs pump laser.

In Appendix B the experimental results on the characterization of the detection system are illustrated. In particular, the effect of the optical system used to match the $F/\#$ of the collection objective and the optical element at the entrance of the FTIR spectrometer is studied as well as the spectral response of the detection system by means of a conventional calibration procedure. Moreover, due the high powers involved in the experiments, the results on the investigation of undesired spurious nonlinear signals generated by the detection system are discussed. Finally, the calibration of the detection system to convert the a.u. of the spectra into average power units is presented.

In Appendix C the characterization of the optical density of the reflective filters, used to control of the fs pump laser power and the study of a low loss selective coupling of the light with a single waveguide are illustrated. In particular, the general description of the reflective objectives in Schwarzschild configuration and the comparison of their performances with those one of standard microscope objectives are given.

This work results from several collaborations, where I have had during my thesis. In particular, I did the stress characterization in collaboration with CIVEN (Coor-

dinamento Interuniversitario Veneto per le Nanotecnologie, Venice (Italy)), where I have performed the micro-Raman spectroscopy experiments together with Dr. F. Enrichi and Dr. R. Pierobon.

The SHG experiment at ns pump regime has been performed by Dr. M. Cazzanelli and Ms. E. Borga. I have subsequently analyzed and interpreted their data; Dr. M. Cazzanelli has contributed also in the setting up of the fs experimental apparatus; Advanced Photonics and Photovoltaics Group of Bruno Kessler Foundation (Trento, Italy) has fabricated the measured samples.

The second SHG experiment has been performed in collaboration with SiLi-nanoMartin group from Luther-Universität (Halle-Wittenberg, Germany), which has fabricated the measured samples.

Chapter 1

Strained silicon waveguides: fabrication and description

This chapter is devoted to the description of the strained silicon waveguides involved in the experiments presented in this thesis. In particular, the methods for the device fabrication and the sample geometry and optical properties are illustrated.

Since several samples have been produced, they are divided in two main categories according to the experiment where they have been employed.

1.1 Strained silicon waveguide used for stress characterization and in the first SHG experiment

These samples have been fabricated by the Advanced Photonics and Photovoltaics Group of Bruno Kessler Foundation (Trento, Italy).

The strained silicon waveguides have been realized on $4'$ (001)-oriented silicon-on-insulator (SOI) substrates with $h_1 \simeq 2.2 \mu\text{m}$ thick silicon device layer isolated from the handle (silicon substrate) by a $h_2 \simeq 2 \mu\text{m}$ thick buried oxide (BOX, SiO_2) layer. The strained condition has been achieved by using several thin layers deposited on the wafer and made of silicon nitride that stress the silicon core of the waveguide.

These stressing layers have been deposited by using two different chemical vapour deposition (CVD) systems that have allowed to obtain thin films with different mechanical properties. In fact, as it will be explained in the next chapter, the total stress inside a thin film is determined by the experimental conditions of its deposition. Therefore, the overlayer stresses have been produced with different extents and signs by using different deposition recipes.

The degree of stress induced by the silicon-nitride layers has been measured in unpatterned wafer by using the curvature method (see Section 2.2.3 for the details of the method), i.e. by depositing the films on bare silicon substrates and measuring the film thickness and wafer curvature before and after deposition with a mechanical profilometer.

A low pressure chemical vapour deposition (LPCVD) reactor has been used for the deposition of high tensile stressed stoichiometric silicon nitride (Si_3N_4). A 150 nm-thick layer of LPCVD- Si_3N_4 has been deposited at 780 °C from NH_3 and SiH_2Cl_2 . This over-layer induces a 1.25 GPa tensile stress on the SOI wafer. This type of samples is called **SOI1**.

The second deposition chamber used is a parallel-plate plasma enhanced chemical vapour deposition (PECVD) system. This system allows to control the stress of the final film by varying the frequency and power of the plasma during deposition (see Section 2.2.2 for the details of the technique). Two different deposition recipes have been used. With the first recipe a 500 nm thick SiN_x layer has been deposited at 300 °C with a low plasma frequency (308 kHz), resulting into a -500 MPa average compressive stress (samples called **SOI2**).

With the second recipe, a stress-compensated SiN_x overlayers has been produced by means of an alternation between high and low plasma frequencies (13.56 MHz for 50 sec and 308 kHz for 10 sec) [44]. Measurements yield a residual stress of -60 MPa (samples called **SOI3**).

Waveguides have been also realised on blank SOI wafer without silicon-nitride top layer as a reference (samples called **SOI0**). The residual stress in the SOI substrates

due to the Si device layer and the BOX has been also evaluated by measuring the wafer curvatures after step by step removal of the device layer and of the BOX. These measurements show that the stress of the Si device layer is negligible in SOI0 samples, while the oxide layer (BOX) induces a stress of -318 MPa.

The Table 1.1 summarizes the fabrication details of the various samples.

Sample	Technique	Temperature	Thin film thickness	Stress
SOI1	LPCVD	780 °C	150 nm	+1.2 GPa
SOI2	PECVD (recipe 1)	300 °C	500 nm	-500 MPa
SOI3	PECVD (recipe 2)	300 °C	500 nm	-60 MPa

Table 1.1: Silicon nitride deposition parameters and measured film stress for the fabricated samples.

Subsequently to the deposition of the stressing layer on the SOI substrate, the waveguides have been defined by a photolithography process and by etching with reactive-ion etching. The device layer has been etched down to the BOX layer to yield strip silicon waveguides (Fig. 1.1.a).

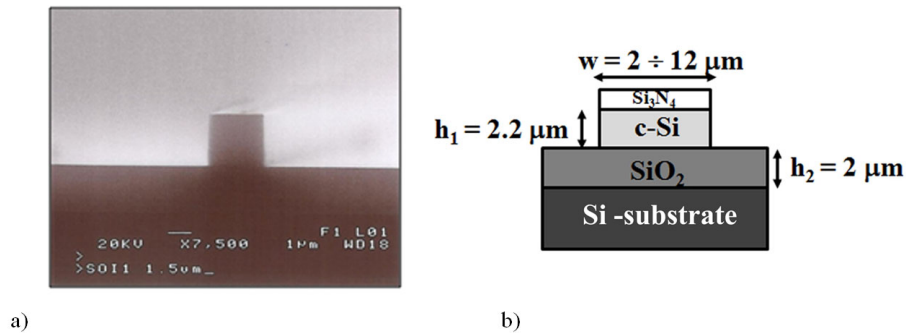


Figure 1.1: a) SEM image of waveguide cross-section; b) schematic of sample structure, where w is the waveguide width and h_1 and h_2 are the height of silicon waveguide and BOX layer, respectively [67].

For each type of sample (SOI0, SOI1, SOI2 and SOI3) the waveguides have been prepared with the same height ($h_2 = 2 \mu\text{m}$) but with different widths, ranging from

2.0 μm to 12 μm (Fig. 1.1.b). The actual dimensions of the waveguides cross-section have been finally measured using a Scanning Electron Microscope (SEM).

The waveguides have been produced with two different lengths, i.e. 1 cm and 2 mm, according to the temporal duration of the pump pulse used in the SHG experiment. In fact, the pulse duration determines the temporal walk-off between the pump and the generated signals. Particularly, the fs pump laser has been coupled into the 2 mm-long waveguides, while the 1 cm-long waveguides have been used in combination with the ns pump, where the temporal walk off is less critical.

Insertion losses characterization

The insertion losses of the strained silicon waveguides have been characterized by using a standard experimental set-up composed by a laser source, tunable between 1260 and 1630 nm (SANTEC full-band tunable laser, TSL-210F), a tapered optical fibre for the insertion of the light into the waveguide and a microscope objective (10 \times) coupled to a germanium photodetector for the measurement of the power of the transmitted signal. The waveguide alignment has been performed by maximizing the power measured by the detector and checking the modal distribution of the guided radiation by using an infrared camera (Sensor Unlimited, SU-320M).

The coupling and propagation losses for the 1 cm-long waveguides have been measured by using the cut-back method, that allows to simultaneously estimate the propagation and coupling losses by measuring the total losses for different lengths of the waveguide. As a result, these waveguides exhibit linear propagation losses (α_p) of 1-3 dB/cm and coupling losses (α_c) of about 13 dB for an input light at 1260 nm and in the 10 μm wide waveguide [45].

Instead, for the 2 mm-long waveguide the two components of insertion losses (α_p and α_c) have been measured separately by using other two different methods. In fact, no waveguides with different lengths were available and thus the cut-back method has not been applicable.

The propagation losses have been estimated by using the scattering light col-

lection method, which allows to measure the propagation loss coefficient α_p independently on the coupling loss. With this method the light scattered from the top surface of the waveguide is measured, as it is assumed to be proportional to the light traveling inside the waveguide. In this way, a spatial exponential decay of the intensity is directly related to the attenuation of the light propagating along the waveguide length. By using an infrared camera, top view images of the scattered light at 1550 nm have been acquired, as shown in Fig. 1.2.a,b.

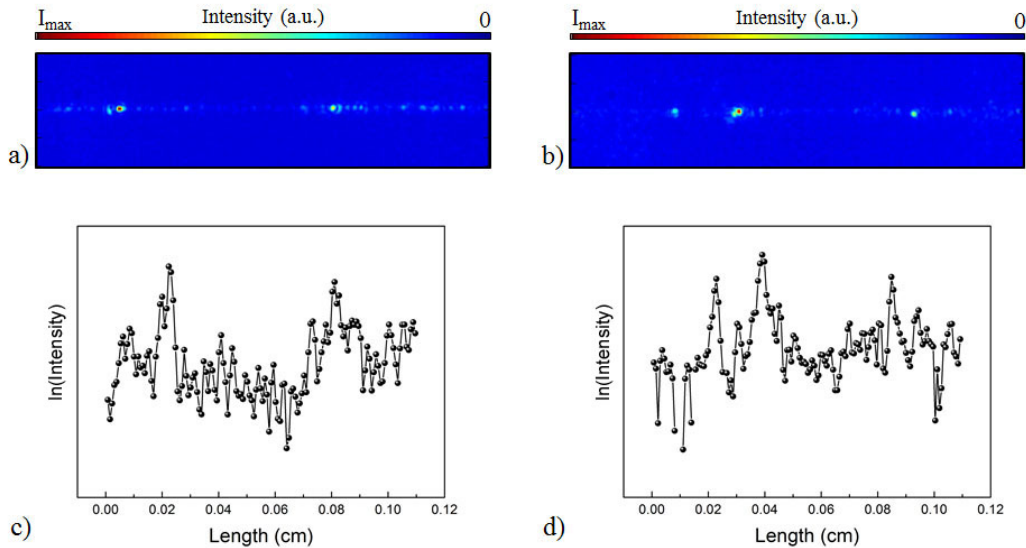


Figure 1.2: Propagation losses measurement by using the scattering light collection method at 1550 nm (TE-polarized): a-b) infrared images in false colors of the scattered light from ~ 1 mm-long top surface of a) $2.6 \mu\text{m}$ - and b) $10.4 \mu\text{m}$ -wide waveguides; c-d) Intensity of the scattered light in natural logarithm scale as a function of the length of c) $2.6 \mu\text{m}$ - and d) $10.4 \mu\text{m}$ -wide waveguides.

From the analysis of scattered light intensity along the waveguide length, the typical exponential decay of the intensity ($I = I_0 \exp(-\alpha_p l)$, where I_0 is the intensity at $l = 0$ and l is the distance from the input facet of the waveguide along the propagation direction) is not measurable both in $10.4 \mu\text{m}$ - and $2.6 \mu\text{m}$ -wide waveguides, as shown in Fig. 1.2.c,d. In fact, the scattered light intensities show an almost flat trend with few maxima only in correspondence of certain positions along the waveguide length, that may be attributed to imperfections inside the structure or

to dust grains on the top surface. Consequently, with this method the propagation loss coefficient in uniformly stressed waveguides can not be estimated. However, an upper bond value can be evaluated. In fact, by applying the same method to a 10.4 μm -wide waveguide covered with a periodic alternation of different cladding layers, the scattered light intensity exponentially decays along the waveguide length allowing to quantify the propagation loss coefficient, that results about 0.6 dB/mm (Fig. 1.3.a). Furthermore, if the intensities of the scattered light from the two different waveguides are compared, the light scattered from a uniformly stressed waveguide has intensity approximately one order of magnitude lower than that from the periodically stressed waveguide (Fig. 1.3.b).

In this way, the propagation loss coefficient of uniformly stressed waveguide can be assumed much lower than 0.6 dB/mm and therefore negligible for all the widths of the waveguides.

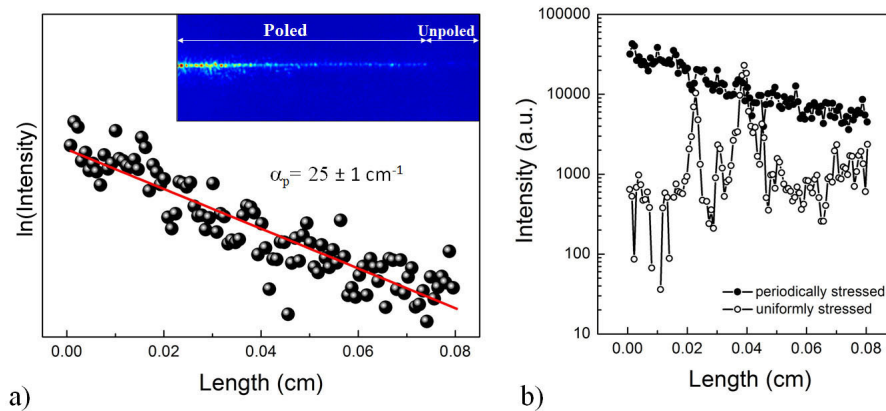


Figure 1.3: a) propagation losses measurement by using the scattering light collection method at 1550 nm (TE-polarized) for a 10.4 μm -wide waveguides with a periodic alternation of different cladding layers (poling). The linear fit (red line) of the natural logarithm of the scattered light intensity as a function of the length gives a propagation loss coefficient of $25 \pm 1 \text{ cm}^{-1}$ (~ 0.6 dB/mm). The inset shows the comparison of the IR images in false color for a poled waveguide and uniform waveguide; b) comparison of scattered light intensity for a periodically (solid circle) and uniformly (open circle) stressed 10.4 μm -wide waveguide.

As a consequence of the negligible propagation loss, the coupling loss can be directly estimated by measuring the output power (P_{out}) of the transmitted radia-

tion, knowing the input power (P_{in}), as $\alpha_c = -10\log(P_{out}/P_{in})$. Table 1.2 shows the coupling losses measured for several waveguides widths at 1550 nm in the sample SOI2. Similar values have been obtained also for the SOI1,3 samples. Instead, the SOI0 sample has coupling loss that is approximately 5 dB lower.

Polarization	Waveguide width		
	10.4 μm	5.1 μm	2.6 μm
TE	(14 \pm 2) dB	(16 \pm 2) dB	(20 \pm 3) dB
TM	(14 \pm 2) dB	(14 \pm 5) dB	(20 \pm 3) dB

Table 1.2: Coupling losses of the sample SOI2 for 2 mm-long waveguides with different widths measured at 1550 nm for the TE- and TM-polarization.

1.2 Strained silicon waveguide in the second SHG experiment

These samples have been produced within the collaboration with C. Schriever of the SiLi-nanoMartin group from Luther-Universität (Halle-Wittenberg, Germany).

The strained silicon waveguides have been fabricated on a (001) SOI wafer by depositing the stressing overlayer in two distinct covering configurations. Two diverse materials with two different thicknesses have been used. Therefore, these samples can be divided into two main categories depending on the covering configuration, that are in turn classified based on the typology of the stressing layer.

In the first category, the devices have been realized such that the stressing layer covers only the top surface of the waveguide, similarly to the structures presented in the previous section. These are called **top covered** samples, as shown in Fig. 1.4.a,b. Within this typology, the thickness of the stressing layer has been varied in order to deposit a **thin film** that is 50 nm high (Fig. 1.4.a) and a **500 nm-thick film** (Fig. 1.4.b). The materials used to produce these layers are silicon

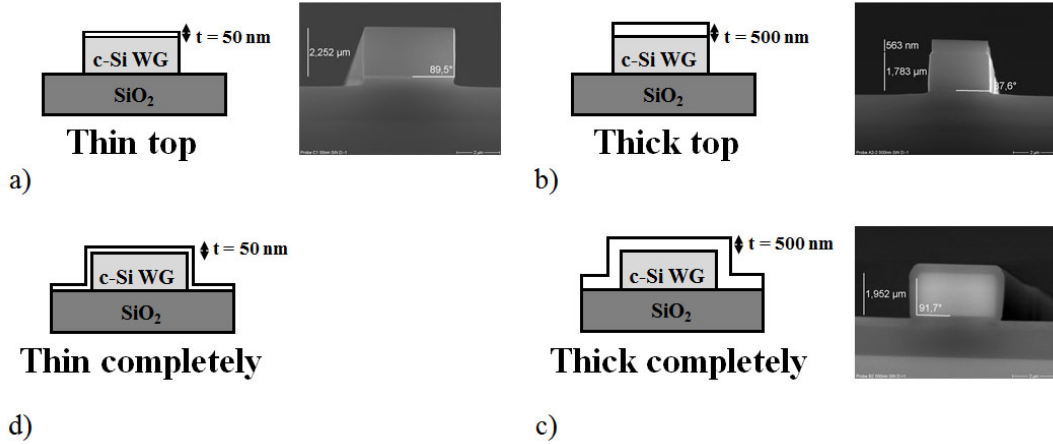


Figure 1.4: Samples classification: a-b) sketches and relative SEM images (silicon nitride layer) of top covering configuration with a thin (50 nm-high) or thick (500 nm-high) stressing layer; c-d) sketches and relative SEM images (silicon nitride layer) of completely covering configuration with a thin (50 nm-high) or thick (500 nm-high) stressing layer.

nitride and silicon oxide.

The second category of samples is called **completely covered** (Fig. 1.4.c,d). In this case, the stressing cladding has been deposited after the waveguide definition process, so that it covers the top and the lateral surfaces of the waveguide. Also in this category, the overlayer thickness has been tuned in 50 nm (Fig. 1.4.c) and 500 nm (Fig. 1.4.d). In this case, only silicon nitride has been used as material of the thin film.

Finally, standard silicon-on-insulator waveguides without stressing cladding have been produced and they are named as **reference** samples.

The stressing layers made of silicon nitride have been deposited by using a parallel plate reactor (Oxford Plasmalab 80) for a PECVD deposition at Paderborn University (Germany). The recipe has comprised ammonia (NH_3) and silane (SiH_4) as source gases that have a gas flow of 30 sccm and 400 sccm, respectively. The pressure and temperature have remained constant for all the samples at 1000 mTorr and 300 °C, respectively. The applied plasma power has been 20 W for both low (100 kHz) and high (13.56 MHz) plasma frequency. The overlayer stress has been

tuned by varying the duty cycle (ψ) of the two frequencies (see Section 2.2.2 for the details of the technique). A duty cycle $\psi = 1$ has resulted in a tensile stress in the layer of +226 MPa, $\psi = 0$ to -7 MPa and $\psi = -1$ to -880 MPa.

The samples covered by a silicon oxide stressing layer have been realized by means of thermal oxidation process at Max-Planck-Institute for Microstructural Physics (Halle, Germany). The samples have been processed in a Tempress oven by wet oxidation at a temperature of 1050 °C.

Table 1.3 summarizes the details of the various waveguides:

Covering configuration	Sample	Overlayer material	Overlayer thickness	Stress
Top	SiNthn-t	silicon nitride	50 nm	-880 MPa
	SiNthk-t	silicon nitride	500 nm	+226 MPa
	SiO ₂ thk-t	silicon oxide	500 nm	-300 MPa
Completely	SiNthn-c	silicon nitride	50 nm	-7 MPa
	SiNthk-c	silicon nitride	500 nm	+226 MPa

Table 1.3: Summary of the produced strained silicon waveguides.

The waveguide definition has been performed before the overlayer deposition in the case of the completely covered samples and after the deposition for the top covered samples. The process has consisted in coating the wafer with chromium and in the subsequent structuring through a photolithographic process. Afterwards the chromium has been removed and the waveguide etching has been carried out by using SF₆ + C₄F₈ plasma. Finally, the samples have been cleaved and cleaned.

The waveguide geometry has been kept similar to the previously described samples. For each type of samples, the waveguides have a common height of 2 μ m and different widths between 2.0 μ m and 10 μ m. In this fabrication run, the waveguides have been produced with a single length, i.e. they are 2 mm-long.

Insertion losses characterization

The coupling and propagation losses coefficients of these waveguides have been separately characterized (measurements carried out by C. Schriever of the SiLi-nanoMartin group from Luther-Universität (Halle-Wittenberg, Germany)).

The propagation loss coefficient has been measured by using the Fabry-Perot resonance method, giving a α_p value lower than 1 dB/mm.

Instead, the coupling loss coefficient has been estimated by measuring the input and output power and by applying $\alpha_c = -10\log(P_{out}/P_{in})$. Average coupling loss of about 12 dB have been measured for all the samples.

Chapter 2

Mechanical characterization of silicon crystalline structure

When mechanical stress is used to improve the existing functionalities or to enable novel ones in a photonic structure, such as a silicon waveguide, a careful stress engineering is required and the study of strain distribution is necessary before full device fabrication. For this purpose micro-Raman measurements have been performed on strained silicon waveguide facets in order to map the stress distributions in the (110) cross-section of strained SOI waveguides. The stress induced by silicon nitride thin films has been varied by process parameters yielding flexible stress engineering [44, 46]. Therefore, in this chapter the influence of different deposition procedures such as low-pressure chemical vapour deposition (LPCVD) and plasma-enhanced chemical vapour deposition (PECVD) on the stress distribution is studied. Moreover, the stress variations due to the different waveguide geometries are also investigated.

Before discussing the experimental results on the stress characterization, a brief overview on the mechanical stress in thin film is given. The first section introduces the concept of stress and strain tensors, as they are the tools commonly used for the mathematical description. After that, the mathematical model, the origins and the effects of the stress into a thin film are explained as well as two common techniques

for the stress measurements.

The general theory of micro-Raman spectroscopy concerning stress measurements is reported in detail. Then, the micro-Raman theory is applied to the specific crystallographic orientation of the waveguide silicon. Finally, the experimental method, the data analysis and the experimental results are presented and discussed.

2.1 Definition of stress and strain tensors

In the theory of elasticity if a solid body is not deformed, all its internal parts are in mechanical equilibrium state, i.e. the resultant of the forces acting on each portion of the body is zero [47]. Therefore, the resultant force is defined as the sum of all the forces exerted on all the infinitesimal volume elements dV of the portion of the body ($\mathbf{F}dV$). Since in the theory of elasticity a body is regarded as a continuum medium, the i th component of total force is $\int_V F_i dV$. However, the resultant force can also be represented as the sum of the forces acting on the infinitesimal surfaces dS enclosing each volume element dV . Consequently, the i th component of the resultant force is rewritten as $\int_S \sigma_{ij} dS_j$, $i, j = 1, 2, 3$, where dS_j is the j th component of the surface element vector orthogonal to the surface dS and σ_{ij} is one of the nine elements of the tensor of rank two, called *stress tensor* [47]. Based on this definition, every element of the stress tensor (σ_{ij}) describes the i th component of the force on unit area perpendicular to the x_j axis (Fig. 2.1) that is distinguished in *normal* elements for $i = j$ and *shear* elements for $i \neq j$.

When the equilibrium state is destroyed by an external force, internal stresses are created to return the solid to equilibrium. As a consequence, the body changes in shape and volume due to the displacement of every points constituting the body and thus it is deformed. A tensor of rank two can be introduced to describe the induced body deformation. This tensor is called *strain tensor* and its elements quantify the gradient of the displacement of each point of the body relative to its initial position.

In case of small deformations, stress and strain tensors are linearly related

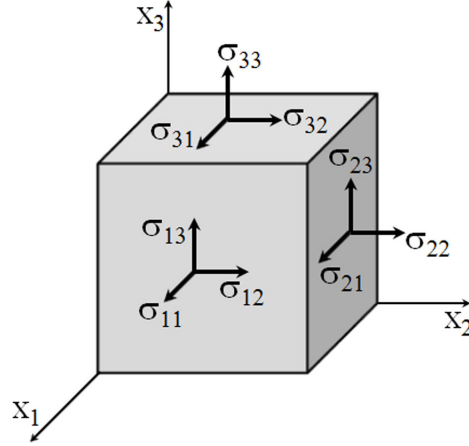


Figure 2.1: Spatial representation of the stress tensor elements σ_{ij} .

through proportionality constants, characteristic of every solid, as established by following equation, called generalized Hooke's law

$$\sigma_{ij} = C_{ijkl}\epsilon_{kl} \quad (2.1.1)$$

where C_{ijkl} are the elastic coefficients belonging to a tensor of rank 4. The tensor \mathbf{C} is named the *stiffness* tensor and quantifies the resistance of the solid to deformation. In general, \mathbf{C} is composed by 81 elements, but due to symmetry reasons they can be reduced to 21 independent elements [48, 49]. Consequently, thanks to the Voigt Kelvin notation a compact form of Eq. 2.1.1 can be deduced:

$$\sigma_i = C_{ij}\epsilon_j \quad (2.1.2)$$

Since the stress-strain relation is assumed to be invertible, the explicit relation of the strain tensor elements with the stress tensor elements can be written as

$$\epsilon_i = S_{ij}\sigma_j \quad (2.1.3)$$

where S_{ij} are the elements of the tensor of rank four, referred as *compliance*, which is the inverse of the stiffness tensor ($\mathbf{S}=\mathbf{C}^{-1}$).

Unlike isotropic materials, where the elastic coefficients have the same values in every direction of the body, in a material as silicon the stiffness and compliance

tensors elements are dependent on the direction of the crystal. However, the elastic properties of a material are generally described by more practical engineering parameters. The first of these parameters is the Young modulus (E), defined as [48]

$$E_i = \frac{\sigma_i}{\epsilon_i} \quad (2.1.4)$$

The Young modulus represents a measure of how much a material is deformed along a i direction under the action of an uniaxial stress σ_i . Thus, the lower the Young modulus value, the more deformable the material.

When a material is squeezed (or stretched) in one direction, a dilation (or compression) is induced in the orthogonal direction. The parameter that quantifies this phenomenon is the Poisson's ratio (ν) [48]

$$\nu_{ij} = -\frac{\epsilon_j}{\epsilon_i} \quad (2.1.5)$$

with $i \neq j$, where i is the longitudinal direction to σ_i and j is the transversal one. This ratio is always positive and for most materials it typically ranges between 0 and 0.5 [47]. A material with $\nu \simeq 0.5$ is perfectly incompressible, like a rubber, while when $\nu \simeq 0$, the material exhibits only a very weak deformation on the orthogonal direction.

In case of silicon, the Young modulus and the Poisson's ratio are generally reported as about 150 GPa and about 0.3, respectively. However, these moduli largely vary in the crystal. Fig. 2.2 shows an example of the dependence of the Young modulus (Fig. 2.2.a) and Poisson's ratio (Fig. 2.2.b) on the crystallographic directions in the (110) plane for the silicon and germanium.

2.2 Mechanical stress in thin films

As definition, a thin film is a layer deposited on a thicker substrate, where the lateral dimensions of film/substrate pair are much larger than the sum of the film and substrate thicknesses [50, 51]. Nowadays, thin films are usually employed for

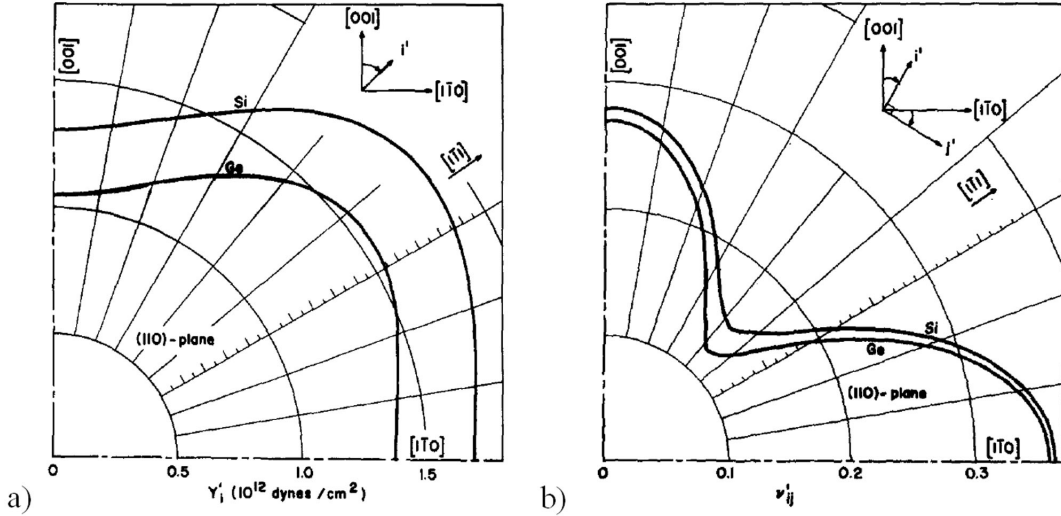


Figure 2.2: Example of Young modulus (a) and Poisson's ratio (b) as a function of the directions in the (110) plane for silicon and germanium [48].

the fabrication of microelectronics and optical devices as well as for the coating of optical components (such as mirrors, filters or solar cells) or more in general for protection of tools and critical parts of industrial machines.

2.2.1 Thin films stress model

During the deposition processes, stresses are developed inside the film due to its adhesion to the substrate. The magnitude and the sign of such internal stresses depend on the technique of deposition and, in particular, on process steps. These stresses are generally modeled as biaxial stress state [50–54], i.e. the state when $\sigma_{xx}, \sigma_{yy} \neq 0$ and $\sigma_{zz} = \sigma_{xy} = \sigma_{yx} = 0$, where the general subindexes $i, j = 1, 2, 3$ of Section 2.1 are now substituted with $i, j = x, y, z$. In fact, the stress generally lies only in the film plane, because both film and substrate are allowed to freely move in the normal direction (z). Instead, the shear components (σ_{xy} and σ_{yx}) are considered negligible because they act only at the edges of the film/substrate pair and rapidly decrease with the distance from the edge (typically over a distance larger than 5 times the film thickness) [50]. However, in case of patterned films the stress

state may become more complex and thus, the biaxial model is a schematization valid mainly for blanket films.

As a consequence of the substrate elasticity and the absence of mechanical equilibrium in the thin film, a stress with opposite sign generates in the substrate to compensate the forces exerted by the film. Furthermore, the substrate is also curved by the action of bending moments generated at the edges where the system tries to achieve an equilibrium state.

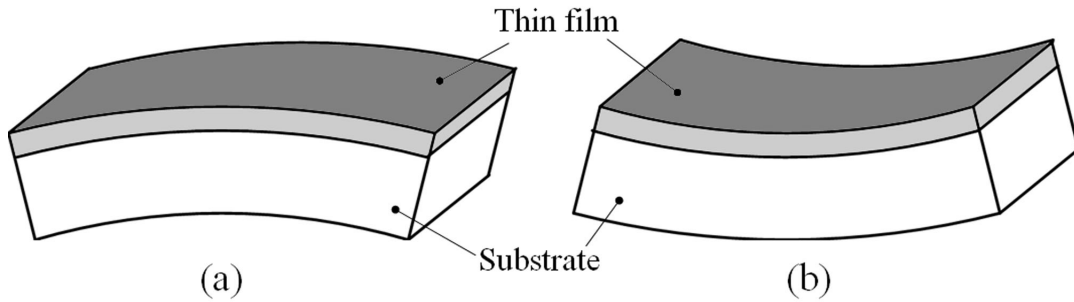


Figure 2.3: Stressed thin film effect: (a) if the thin film has a compressive stress, the substrate is bent downward; (b) if the thin film has a tensile stress, the substrate is bent upward.

Hence, if a compressive stress is present inside the thin film, a tensile stress acts in the substrate, which is bent downward (as shown in Fig. 2.3.a). Instead, in case of stretching film, the substrate is compressed and its surface is concave upward (as shown in Fig. 2.3.b).

2.2.2 Stress origins in thin films

The stress in a thin film may have several causes that can be distinguished in *extrinsic* factors, which are related to the interaction of the thin film with the substrate, and in *intrinsic* factors, which are determined by physical and chemical variations of the thin film during the deposition processes. The contributions of such factors superimpose each others, thus the total thin film stress can be written as

$$\sigma = \sigma_{ext} + \sigma_{int} \quad (2.2.1)$$

where σ_{ext} is the stress related to extrinsic origins and σ_{int} is the stress caused by intrinsic factors.

One of the main sources of the extrinsic stress is the mismatch in the thermal expansion coefficients (CETs) between the film and the substrate. The thin film deposition is usually carried out at high temperature with subsequent cooling down of the produced structure to room temperature, where most devices work at. If the cooling down is rapid, thin film and substrate change their sizes in different way as result of the difference in CETs (α), that can be defined as [52]

$$\alpha = \frac{d\epsilon}{dT} \quad (2.2.2)$$

where ϵ is the strain and T is the temperature. Assuming a CET weakly dependent on temperature, the strain dependence on the CET can be derived from Eq. 2.2.2 as

$$\epsilon \simeq \alpha \Delta T \quad (2.2.3)$$

where ΔT is the difference between the deposition and room temperature.

Therefore, a stress with thermal origin is induced inside the structure when materials with different CETs are bonded to each other, causing a dependence of the stress state on the thermal history of the device. For example, when a tensile stressed thin film (f) is attached to a substrate (s), the compatibility condition requires that the strain of thin film attached is equal to the strain of the substrate ($\epsilon_{f,att} = \epsilon_s$), thus

$$\epsilon_{f,att} = -\alpha_s \Delta T \quad (2.2.4)$$

where the minus sign represents the compression in the substrate. However, if the film was unattached, after the cooling it would have a strain

$$\epsilon_{f,unatt} = -\alpha_f \Delta T \quad (2.2.5)$$

Consequently, the difference in the film strain at room temperature ($\epsilon_{f,th}$) after the deposition due to the presence of the substrate is

$$\epsilon_{f,th} = \epsilon_{f,att} - \epsilon_{f,unatt} = (\alpha_f - \alpha_s) \Delta T \quad (2.2.6)$$

This thermal mismatch strain leads to the called *thermal stress*

$$\sigma_{f,th} = \frac{E}{1 - \nu}(\alpha_f - \alpha_s)\Delta T \quad (2.2.7)$$

As it can be seen from Eq. 2.2.7, by using the convention that a positive stress is tensile and a negative one is compressive, when $\alpha_f > \alpha_s$, a tensile stress is induced in the film or a compression otherwise.

Let us now consider the materials involved in this thesis. Their CET values are reported in Table 2.1, thus the expected magnitude and sign of the thermal stress can be deduced from Eq. 2.2.7.

	Silicon	Silicon oxide	Silicon Nitride
α ($^{\circ}\text{C}^{-1}$)	$2.61 \cdot 10^{-6}$	$0.52 \cdot 10^{-6}$	LPCVD $\sim 2 \cdot 10^{-6}$ PECVD $\sim 3 \cdot 10^{-6}$

Table 2.1: Thermal expansion coefficient values for silicon [55], silicon oxide [55] and silicon nitride [56,57].

While silicon and silicon nitride have similar CET values, thus the resulting thermal stress may be considered negligible in cases where the intrinsic stress is large, the silicon oxide has a much lower CET. This means that when silicon and silicon oxide are attached, a compressive thermal stress of the silicon oxide gives rise to a stretching of the silicon crystalline structure.

The intrinsic stress may arise due to many factors, which are mainly determined by the experimental conditions of deposition. In fact, depending on technique but also on the selected deposition recipe, the intrinsic stress may be tuned in sign and extent, especially in case of silicon nitride. For example, in silicon nitride films the total stress can range between -3 GPa to 1.6 GPa [58].

The silicon nitride is commonly deposited by using two different techniques: Low-Pressure Chemical Vapour Deposition (LPCVD) and Plasma-Enhanced Chemical Vapour Deposition (PECVD).

The parameters that mainly define the resulting intrinsic stress in a silicon nitride film deposited by LPCVD are the temperature, the pressure and the input gas ratio inside the reactor, as they determine stoichiometry, chemical bonding and mechanical properties of the film [46, 56]. For example, as observed in [56], the silicon nitride film that has tensile stress can be assumed as bulk silicon nitride (Si_3N_4) that is structurally perturbed. Due to the chemistry imposed by deposition recipe, the film chemical composition is close to the stoichiometry of Si_3N_4 , so the resulting Si/N concentration ratio leads to a constrained structure with Si-N bonds stretched relative to the equilibrium state [58]. This results in films that have intrinsic tensile stress, but characteristic similar to stoichiometric silicon nitride, i.e. smaller refractive index, higher atomic density and smaller Si/N concentration ratio. Instead, the compressively stressed films can be considered as perturbed silicon-like structures and thus with larger refractive index, smaller atomic density and larger Si/N ratio. In this case, the intrinsic stress is not particularly large, hence the final stress is the superimposition of intrinsic and thermal stresses ($\alpha_{\text{SiN}_{LPCVD}} < \alpha_{\text{Si}}$).

Unlike the LPCVD technique, where the chemical reactions of the precursors occur thanks to the high temperature, the PECVD deposition technique employs a discharge in the source gases to generate the reactants that subsequently interact to form the deposition layer. Such discharge is induced by an electric field that is commonly generated by a RF source. It has been seen that plasma frequency has an important role on the intrinsic stress in the film as well as the temperature [44, 59]. Particularly, it has been found that a tensile intrinsic stress is achieved when the plasma frequency and the temperature are high, while low frequency and low temperature yield to a compressive stress. When the frequency is low, the ions of the plasma are able to follow the alternation of the electric field and thus they can bombard the growing silicon nitride layer leading to an ion implantation. As a consequence of the densification and the presence of defects, the film results in a compression state. In case of high temperature, this effect is reduced because the defects are removed. On the other hand, when frequency is high, the ions are not

able to oscillate with the electric field, thus the ion implantation does not occur. However, the combination with the high temperature causes the desorption of the hydrogen accumulated in the film during the process, which reduces the density of the film. The creation of a tensile intrinsic stress is added up to the tensile thermal stress ($\alpha_{SiN_{PECVD}} > \alpha_{Si}$) [40, 59].

As demonstrated in [44], a suitable PECVD method to achieve intermediate stress values is to use two plasma excitation frequencies. By fixing the low and high plasma frequencies at certain values (for example, at 380 KHz and 13.56 MHz as in [44]), the stress value is tuned by mixing low and high plasma frequencies. In particular, stress ranging from compressive to tensile is obtained by changing the duty cycle (ψ) of the two frequencies

$$\psi = \frac{t_{HF} - t_{LF}}{t_{HF} + t_{LF}} \quad (2.2.8)$$

where t_{HF} and t_{LF} are the time intervals in one deposition cycle of high and low frequency, respectively. A maximum compressive stress is observed for $\psi = -1$ (i.e. for $t_{HF} = 0$) and intermediate compressive values for $-1 < \psi \lesssim 0.5$. Intermediate tensile stress values are achieved when $\psi \gtrsim 0.5$, reaching a maximum value for $\psi = 1$ (i.e. for $t_{LF} = 0$).

It is worth noting that unlike a LPCVD silicon nitride layer, an as-deposited PECVD silicon nitride layer has a critical mechanical stability. In fact, post thermal treatments above the the deposition temperature have shown that a LPCVD layer maintains the as-deposited mechanical and optical properties, showing only small variations in total stress, Young modulus and refractive index [58]. Instead, due to the heating, the defects that are inside a PECVD layer are annealed out. This causes a variation of the refractive index. The stress increases when it is tensile or changes into tensile, when it is compressive [58].

In a silicon oxide layer grown by oxidation process, an intrinsic stress is determined by the oxidation temperature and is originated by the molar volume change in converting silicon in silicon oxide [40, 55]. For temperature higher than 950 °C, the

volumetric expansion of silicon oxide created during the oxidation is relieved, since the film viscosity is sufficiently low to allow a free movement in the normal direction to the layer surface [55]. Instead, when the temperature is lower than 950 °C, the film viscosity is so high, that, in combination with the adhesion to the substrate, a relaxation of the silicon oxide volumetric expansion is not allowed. This yields the generation of a compressive intrinsic stress.

2.2.3 Examples of stress measurement techniques

Before describing the stress measurement techniques, it is important to underline that in all possible methods, a direct measure of the stress is never possible. The reason is that when the structure reaches the equilibrium state, the stress relaxes and vanishes giving rise to a relaxed strain. This means that the stress state in the film can be only deduced by the deformation that takes place when the system finds an equilibrium.

In addition to the micro-Raman technique, whose measurements principles will be describes in detail in the next sections, there are two other techniques commonly used to gather information on the stress state of a thin film.

The first technique is the *curvature method*. As mentioned in Subsection 2.2.1, when a stressed thin film is bonded to an elastic substrate, the structure is curved upward or downward depending on the thin film stress. As the thickness of the film is much thinner than the substrate one, the curvature radius can be assume to be the same for the bent thin film/substrate pair (Fig. 2.4).

In this way, by measuring the curvature radius the stress in the thin film can be deduced from the Stoney's Equation [60]

$$\sigma_f = \frac{1}{6R} \frac{E_s d_s^2}{d_f (1 - \nu_s)} \quad (2.2.9)$$

where R is the curvature radius, d_f is the film thickness (typically measured by optical ellipsometry) and d_s is the substrate thickness.

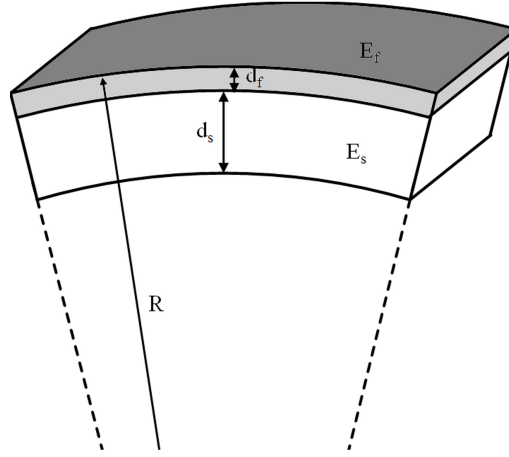


Figure 2.4: Curvature method measures the stress in a thin film with Young modulus E_f and thickness d_f attached to a substrate with Young modulus E_s and thickness d_s by measuring the curvature radius R of the bent film/substrate pair.

To take into account possible bending of substrate before the deposition due to a non-perfect planar surface, Eq. 2.2.9 can be generalized as [52]

$$\sigma_f = \frac{E_s d_s^2}{6 d_f (1 - \nu_s)} \left(\frac{1}{R_{af}} - \frac{1}{R_{bf}} \right) \quad (2.2.10)$$

where R_{af} and R_{bf} are the curvature radii after and before deposition, respectively.

Although this technique is fast and practical, it can be applied only in unpatterned wafer and yields only an average value of the stress without giving information on the local stress distribution.

A technique allowing an accurate local stress measure with a good spatial resolution (even below $1 \mu\text{m}$ [61]) in crystalline materials is the *X-ray diffraction method*. In presence of elastic strain, the crystal lattice constant is altered in relation to its unperturbed value. Hence, by estimating from the diffraction pattern the lattice constant in stress and unstressed film, the film stress is calculated as [60]

$$\sigma_f = -\frac{E}{2\nu} \left(\frac{\bar{a}_0 - a_0}{a_0} \right) \quad (2.2.11)$$

where \bar{a}_0 is the deformed lattice constant and a_0 is the lattice constant in unstressed film.

Although this technique allows a non-destructive investigation of the stress distributions with high accuracy, high control and good spatial resolution, its main disadvantage is the requirement of an expensive and delicate apparatus, which generally is not easily accessible.

2.3 Micro-Raman spectroscopy for stress measurements

A stress measurement method combining accessible apparatus and good accuracy is the Micro-Raman spectroscopy. This technique uses an optical microscope coupled with a high resolution optical spectrometer to detect the photon remitted after an inelastic scattering of an incident photon from an optical phonon of the material. Therefore, it is non-destructive, relatively fast and it does not require any particular sample preparation. Furthermore, thanks to routine analysis implementable in the laboratory apparatus, a 2D mapping of the local stress distribution can be performed with micrometric spatial resolution.

The inelastic scattering involved in this method is the Raman scattering. Consider an electromagnetic radiation with wavevector \mathbf{k}_i and frequency ω_i incident in the medium

$$\mathbf{F}(\mathbf{r}, t) = \mathbf{F}_i(\mathbf{k}_i, \omega_i) \cos(\mathbf{k}_i \cdot \mathbf{r} - \omega_i t) \quad (2.3.1)$$

When the medium is at a finite temperature, atomic vibrations (or phonons) are thermally excited and the atomic displacement can be described as plane waves, having wavevector \mathbf{q} and frequency ω_0 ,

$$\mathbf{Q}(\mathbf{r}, t) = \mathbf{Q}(\mathbf{q}, \omega_0) \cos(\mathbf{q} \cdot \mathbf{r} - \omega_0 t) \quad (2.3.2)$$

As a consequence, the electrical susceptibility χ is modified and it can be assumed a function of \mathbf{Q} [62]. As the amplitude of the vibrations are generally small compared to the lattice constant, the electrical susceptibility χ can be expanded in a Taylor

series of $\mathbf{Q}(\mathbf{r}, t)$

$$\chi(\mathbf{k}_i, \omega_i, \mathbf{Q}) \simeq \chi_0(\mathbf{k}_i, \omega_i) + \left(\frac{\partial\chi}{\partial\mathbf{Q}}\right)_0 \mathbf{Q}(\mathbf{r}, t) + \dots \quad (2.3.3)$$

The term χ_0 is the electric susceptibility in absence of atomic vibrations and it is responsible for the Rayleigh scattering. The second term in the right hand side is the oscillating part of susceptibility caused by the phonons and is responsible for the Raman scattering at the first order.

When an electromagnetic wave travels into a medium, the interaction induces a polarization. In this case, the polarization can be distinguished in a linear component, which is in phase with the incident radiation, and in a component induced by the phonons ($\mathbf{P}_{ph}(\mathbf{r}, t, \mathbf{Q})$). This component can be expressed as [62]

$$\mathbf{P}_{ph}(\mathbf{r}, t, \mathbf{Q}) = \left(\frac{\partial\chi}{\partial\mathbf{Q}}\right)_0 \mathbf{Q}(\mathbf{q}, \omega_0) \cos(\mathbf{q} \cdot \mathbf{r} - \omega_0 t) \mathbf{F}_i(\mathbf{k}_i, \omega_i) \cos(\mathbf{k}_i \cdot \mathbf{r} - \omega_i t) \quad (2.3.4)$$

or

$$\mathbf{P}_{ph}(\mathbf{r}, t, \mathbf{Q}) = \frac{1}{2} \left(\frac{\partial\chi}{\partial\mathbf{Q}}\right)_0 \mathbf{Q}(\mathbf{q}, \omega_0) \mathbf{F}_i(\mathbf{k}_i, \omega_i) \{ \cos[(\mathbf{k}_i + \mathbf{q}) \cdot \mathbf{r} - (\omega_i + \omega_0)t] + \cos[(\mathbf{k}_i - \mathbf{q}) \cdot \mathbf{r} - (\omega_i - \omega_0)t] \} \quad (2.3.5)$$

As consequence of the interaction of the incident radiation with the atomic vibrations of the medium, the induced polarization \mathbf{P}_{ph} generates two waves: the wave called *Stokes* with frequency $\omega_S = \omega_i - \omega_0$ and the wave called *Antistokes* with frequency $\omega_A = \omega_i + \omega_0$.

Silicon is a Raman active material, i.e. its phonons can be optically excited in Raman scattering and its spectrum is shown in Fig. 2.5

The silicon Raman spectrum is centered at 15.6 THz (or in wavenumber at 521 cm^{-1}) from the frequency of incident radiation (this frequency distance is usually referred as *Raman shift*) and its full-width at half maximum (FWHM) is 105 GHz, which, for example, is much narrower than the 40 THz Raman bandwidth of silicon oxide.

Hence, thanks to the physics of the Raman scattering, the scattered photon contains information on the crystalline structure of the medium and thus, it can be used as a probe of structural deformations.

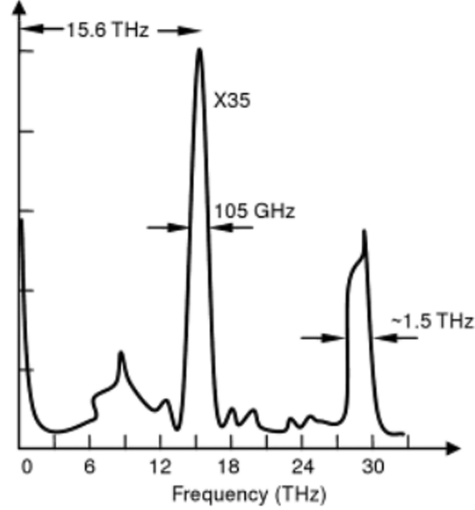


Figure 2.5: Raman spectrum of silicon [1]

2.3.1 General theory of micro-Raman spectroscopy for stress measurements

The description of stress effect on the first order Raman scattering for crystals with diamond structure has been introduced in 1970 by Ganesan et al. [63]. In a diamond crystal, the triply degenerate optical phonons of the zone center are Raman active and they can be represented by the Raman tensors. These are tensors of rank two obtained by a contraction of the vector displacement \mathbf{Q} and of the derivative of χ with respect to \mathbf{Q} as [62]

$$R = \left(\frac{\partial \chi}{\partial \mathbf{Q}} \right)_0 \hat{\mathbf{Q}}(\omega_0) \quad (2.3.6)$$

where $\hat{\mathbf{Q}}$ is the unit vector of \mathbf{Q} . In a diamond crystal the Raman tensors have the following matrix representation:

$$R_1 = \begin{pmatrix} 0 & 0 & 0 \\ 0 & 0 & d \\ 0 & d & 0 \end{pmatrix} \quad R_2 = \begin{pmatrix} 0 & 0 & d \\ 0 & 0 & 0 \\ d & 0 & 0 \end{pmatrix} \quad R_3 = \begin{pmatrix} 0 & d & 0 \\ d & 0 & 0 \\ 0 & 0 & 0 \end{pmatrix} \quad (2.3.7)$$

where d is a constant that depends on the polarizability of material [64].

The intensity of scattered photons can be calculated from the time averaged power radiated by the induced polarization \mathbf{P}_{ph} into unit solid angle. This intensity

depends on the polarization of incident and scattered radiations ($\mathbf{e}_0, \mathbf{e}_s$), i.e. it is proportional to $|\mathbf{e}_0 \cdot \mathbf{P}_{ph} \cdot \mathbf{e}_s|^2$. Therefore, the intensity of the scattered photon from the i th phonon is calculated as

$$I_i \propto |\mathbf{e}_0 \cdot \mathbf{R}_i \cdot \mathbf{e}_s|^2 \quad (2.3.8)$$

This equation sets the selection rule for the Raman scattering and it predicts the intensity of the scattered photon by the i th phonon measurable in a given experimental condition.

The presence of a stress-induced deformation of the lattice lowers the crystal symmetry, so that the directions of phonon vibrations ($\mathbf{v}_1, \mathbf{v}_2, \mathbf{v}_3$) are changed and the threefold degeneracy of their frequencies is partially lifted [63,65]. Consequently, the Raman frequencies are shifted with respect to their value in undeformed structure.

The equation describing the stress effect on the optical properties of a diamond crystal has been developed by using the lattice theory of morphic effects [63]. In presence of strain, the phonons frequencies are given by the solutions of the eigenvalue problem

$$\sum_j K_{ij} \eta_j = \omega^2 \eta_i \quad (2.3.9)$$

where $i, j = x, y, z$, K_{ij} are the elements of the force constant tensor, η_j are the Cartesian coordinates of the eigenvectors and ω is the Raman frequency of the strained mode. Assuming a small strain, the K_{ij} elements can be linearly expanded in terms of strain powers as

$$K_{ij} \simeq K_{ij}^{(0)} + \sum_{k,l} \epsilon_{kl} K_{ijkl}^{(\epsilon)} \quad (2.3.10)$$

$$\text{with } K_{ij}^{(0)} = \omega_0^2 \delta_{ij}$$

$$K_{ijkl}^{(\epsilon)} = \frac{\partial K_{ij}}{\partial \epsilon_{kl}}$$

where K_{ij} are the elements of the force constant tensor in absence of strain, ω_0 is the Raman frequency in unstrained crystal, δ_{ij} is the Kronecker delta and ϵ_{kl}

are the strain tensor elements. The strain effect on the crystal is included into the anharmonicity parameters $K_{ijkl}^{(\epsilon)}$, that describe the modification of the effective harmonic force constant in presence of a small strain (quasi harmonic approximation) and they are referred as *phonon deformation potentials*. In a diamond crystal, $K_{ijkl}^{(\epsilon)}$ are only three independent nonzero elements:

$$\begin{aligned} K_{xxxx}^{(\epsilon)} &= K_{yyyy}^{(\epsilon)} = K_{zzzz}^{(\epsilon)} = p \\ K_{xxyy}^{(\epsilon)} &= K_{xxzz}^{(\epsilon)} = K_{yyzz}^{(\epsilon)} = q \\ K_{xyxy}^{(\epsilon)} &= K_{yzyz}^{(\epsilon)} = K_{zxzx}^{(\epsilon)} = r \end{aligned} \quad (2.3.11)$$

where p, q, r are phenomenological constants, whose values strictly depend on the crystal material.

By replacing Eq. 2.3.10 in Eq. 2.3.9, the eigenproblem is rewritten as

$$\sum_j \sum_{kl} \epsilon_{kl} K_{ijkl}^{(\epsilon)} \eta_j = (\omega^2 - \omega_0^2) \eta_i \quad (2.3.12)$$

or rather in matrix form as

$$\begin{vmatrix} p\epsilon_{xx} + q(\epsilon_{yy} + \epsilon_{zz}) - \lambda & 2r\epsilon_{xy} & 2r\epsilon_{xz} \\ 2r\epsilon_{xy} & p\epsilon_{yy} + q(\epsilon_{xx} + \epsilon_{zz}) - \lambda & 2r\epsilon_{yz} \\ 2r\epsilon_{xz} & 2r\epsilon_{yz} & p\epsilon_{zz} + q(\epsilon_{xx} + \epsilon_{yy}) - \lambda \end{vmatrix} = 0 \quad (2.3.13)$$

that is a *secular equation*. By calculating the eigenvalues of this equation ($\lambda_i = \omega_i^2 - \omega_0^2$, with $i= 1, 2, 3$), the Raman frequency shift ($\Delta\omega_i$) of i th mode caused by the strain can be obtained as

$$\Delta\omega_i = \omega_i - \omega_0 \simeq \frac{\lambda_i}{2\omega_0} \quad (2.3.14)$$

Furthermore, the corresponding three eigenvalues describe the polarization vectors of the phonons in the presence of strain (\mathbf{v}_{i-st}) and thus, the strained Raman tensors can be calculated as

$$\mathbf{R}_{i-st} = \sum_{k=1,2,3} \mathbf{R}_k \frac{\partial \mathbf{v}_k}{\partial \mathbf{v}_{i-st}} \quad (2.3.15)$$

Hence, the effect of the strain on a crystal can be simply evaluated by performing a Raman scattering experiment to measure the Raman frequency and by solving the secular equation (rewritten for the specific material and crystallographic reference system) to relate the measured Raman frequency shift with the strain.

2.3.2 Theoretical model for stress measurements in silicon waveguide

Let us now consider the silicon waveguides described in Section 1.1 and show how the model has been adapted to map the stress distribution in their cross-section.

The waveguide guiding direction is longitudinal to $X'=[110]$ crystallographic axis, while the cross-section lies on the plane formed by the $Y'=[-110]$ and $Z'=[001]$ axes. As it is usually done, this reference system will be referred as sample system (in the following the prime sign (') indicates the sample system) [66] and it will be distinguished from the reference system ($X=[100]$, $Y=[010]$, $Z=[001]$), which is typically used for describing the Raman effect in silicon (see Fig. 2.6).

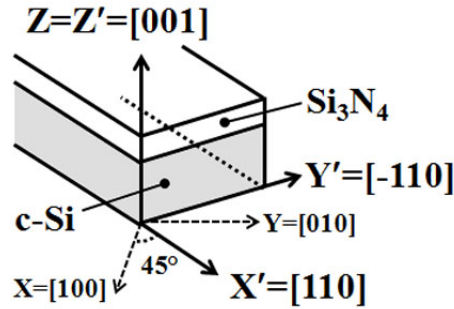


Figure 2.6: Definition of the reference ($X=[100]$, $Y=[010]$, $Z=[001]$) and the sample ($X'=[110]$, $Y'=[-110]$, $Z'=[001]$) coordinates system for the investigated waveguide [67]

Since the secular equation (Eq. 2.3.13) is written considering the reference coordinates system, there are two methods to solve it for a stress oriented in a different coordinates system. One method is to directly calculate the secular equation in the sample system, the other one is to calculate the strain in the reference system and

then solve the secular equation [66]. Although both methods provide the same results, the first is generally preferable in case of complex stress tensor. Nevertheless, in the present experiments only one Raman peak has been observed, indicating that the stress is too small to cause a clear phonon splitting. So, although the contribution of the stress tensor elements should be considered, not all the unknown stress components can be measured with accuracy by the experiment. As a result, a stress model is necessary to reduce the number of the stress components.

Since the micro-Raman experiment has been performed from the facets of silicon strip waveguides, a series of assumptions helps to simplify the treatment:

1. the laser is absorbed close to the surface, e.g. the penetration depth is about 770 nm in silicon at 514 nm [68], so that only the near plane state can be determined [69]. Consequently, the normal stress σ'_{XX} can be omitted.
2. owing to the high refractive index contrast between silicon ($n_{Si} \simeq 3.5$) and silicon oxide or silicon nitride ($n_{SiO_2} \simeq 1.5$ and $n_{SiN} \simeq 2$), a good confinement of the propagation modes inside the waveguide core is achieved. Thereby, the shear stresses (σ'_{IJ} with $I \neq J$) have been neglected because they are relevant mainly in the vicinity of the waveguide edges [66] that are not probed by the propagating radiation.

The complexity and the local distribution of the stress tensor can be reduced to one principal element oriented along Y' axis (σ'_{YY}). This identifies the uniaxial stress model which is commonly used [66,68] and is sufficient for a qualitative insight into the stress distribution.

Within this assumption, the secular equation can be easily solved also in the reference coordinates system by expressing the strain components ϵ_{ij} in the reference system in terms of the strain components ϵ'_{ij} in the sample system.

Therefore, as the stress tensor is now known, the strain components ϵ'_{ij} are calculated by using the Hooke's law in the sample system $\epsilon' = \mathbf{S}'\sigma'$, where \mathbf{S}' is the

compliance tensor in sample system

$$\epsilon'_{XX} = \left(\frac{S_{11} + S_{12}}{2} - \frac{S_{44}}{4} \right) \sigma'_{YY} \quad (2.3.16a)$$

$$\epsilon'_{YY} = \left(\frac{S_{11} + S_{12}}{2} + \frac{S_{44}}{4} \right) \sigma'_{YY} \quad (2.3.16b)$$

$$\epsilon'_{ZZ} = S_{12} \sigma'_{YY} \quad (2.3.16c)$$

where $S_{11} = 7.68 \cdot 10^{-12} \text{ Pa}^{-1}$, $S_{12} = -2.14 \cdot 10^{-12} \text{ Pa}^{-1}$ and $S_{44} = 12.7 \cdot 10^{-12} \text{ Pa}^{-1}$ are the elastic compliance elements of silicon [48]. Instead, the components ϵ'_{XY} , ϵ'_{YZ} , ϵ'_{XZ} are equal to zero.

Thus, the Raman peak shift as a function of the uniaxial stress in the sample system are derived as follows

$$\Delta\omega_1 = \frac{1}{2\omega_0} \left\{ \left[\left(\frac{p+q}{2} \right) (S_{12} + S_{22}) + qS_{12} - \frac{rS_{44}}{2} \right] \sigma'_{YY} \right\} \quad (2.3.17a)$$

$$\Delta\omega_2 = \frac{1}{2\omega_0} \left\{ \left[\left(\frac{p+q}{2} \right) (S_{12} + S_{22}) + qS_{12} + \frac{rS_{44}}{2} \right] \sigma'_{YY} \right\} \quad (2.3.17b)$$

$$\Delta\omega_3 = \frac{1}{2\omega_0} \left\{ [pS_{12} + q(S_{12} + S_{11})] \sigma'_{YY} \right\} \quad (2.3.17c)$$

The linearity of these relations shows that a compressive stress ($\sigma'_{YY} < 0$) results in an increase of the Raman frequency, while a tensile stress ($\sigma'_{YY} > 0$) yields a decrease.

The eigenvectors of the secular equation describing the new polarizations of the phonons are represented by the set of vectors $\mathbf{v}_{1.st} = 1/\sqrt{2}(110)$, $\mathbf{v}_{2.st} = 1/\sqrt{2}(-110)$ and $\mathbf{v}_{3.st} = 1/\sqrt{2}(001)$. Since they are expressed in the reference system, they are parallel to the X', Y' and Z' axes of the sample system, respectively. Instead, the strained Raman tensors are given as

$$R_{1.st} = \frac{d}{\sqrt{2}} \begin{pmatrix} 0 & 0 & 1 \\ 0 & 0 & 1 \\ 1 & 1 & 0 \end{pmatrix} \quad R_{2.st} = \frac{d}{\sqrt{2}} \begin{pmatrix} 0 & 0 & 1 \\ 0 & 0 & -1 \\ 1 & -1 & 0 \end{pmatrix} \quad R_{3.st} = \frac{d}{\sqrt{2}} \begin{pmatrix} 0 & 1 & 0 \\ 1 & 0 & 0 \\ 0 & 0 & 0 \end{pmatrix} \quad (2.3.18)$$

Substituting these tensors into Eq. 2.3.8, the polarization selection rule in the presence of stress is obtained. For the backscattering configuration from the (110)

surface only the transversal optical phonons (TO) can be observed (i.e. $I_{2-st}, I_{3-st} \neq 0$). No Raman signal comes from the longitudinal phonon (LO) for any random settings of light polarization (\mathbf{e}_0 versus \mathbf{e}_s) in $Y' - Z'$ plane.

2.3.3 Description of stress measurements method

A. Experimental and data analysis procedure

The experiments have been carried out at room temperature in a confocal backscattering configuration from the (110) crystal plane by using a WITec alpha300 S Scanning Near Field Optical Microscope (SNOM) in Raman imaging mode, as shown in Fig. 2.7.a.

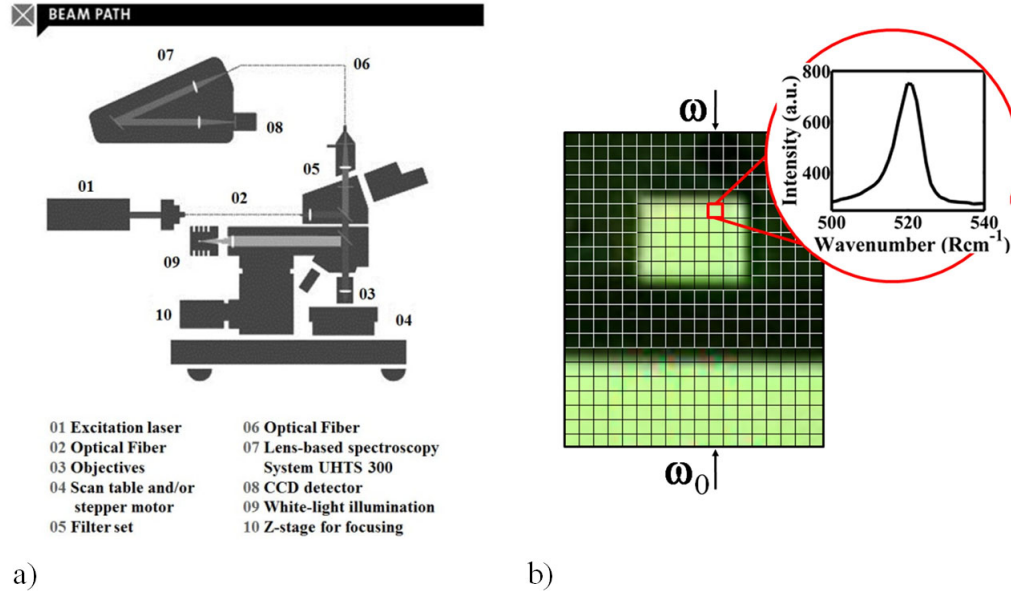


Figure 2.7: a) Micro-Raman set-up: WITec alpha300 S Scanning Near Field Optical Microscope (SNOM) in Raman imaging mode (Adapted from [70]); b) Scanning grid (not to scale) over imposed to an optical image of the waveguide facet. The inset shows a typical Raman spectrum. The two arrows point to the areas of strained and unstrained bulk silicon, where the shifted Raman frequency ω and the reference Raman frequency ω_0 are measured, respectively [67].

The Raman scattering has been excited by a linearly polarized CW Argon laser at a wavelength of 514 nm. The laser power has been adjusted to be as low as possible

in order to avoid a down-shift of the Raman peak due to thermal effects. The scattered light has been detected with the help of an optical spectrometer equipped with a 1800 grooves/mm grating enabling the acquisition of Raman spectra in the 400-850 nm range. In fact, the narrow notch filter, which is typically utilized to attenuate the wavelengths in the excitation laser region, has not been included in order to acquire the Rayleigh scattered line used as internal reference to monitor the set-up stability.

The incident laser light has been focused onto the sample surface through a 100× microscope objective resulting in a focused spot with a diameter of $\sim 0.5 \mu\text{m}$. Because of the confocal configuration, a preparation treatment of the sample has been necessary, otherwise focusing problems could affect the measurements. After the perpendicular cleaving to the waveguide direction, the facets of the waveguides have been lapped to optical quality by using different grades of abrasive papers and polishing with diamond and $0.06 \mu\text{m}$ aluminium oxide suspensions. Finally, the samples have been cleaned and sonicated in ethanol for three minutes at room temperature and dried with a gentle nitrogen flux.

The mapping of the stress distribution has been performed by scanning the sample facet with $0.25 \mu\text{m}$ steps in Y' - and Z' -directions acquiring for each probed area the spectrum in the 400-850 nm range (Fig. 2.7.b). The scanned surface has been selected in order to probe also the bulk silicon far from the interface with the silicon oxide. In this way, the measured Raman frequency has been used as representative of the silicon phonon frequency in unstrained condition. Moreover, only the Raman spectra centred at 521 cm^{-1} have been considered, therefore the contributions of Si_3N_4 and SiO_2 claddings have been neglected.

All the data analysis has been performed by a code written in MatLab. The first step has been the Lorentzian fit of the Raman peaks of every scanned area that has yielded the frequency with a resolution below 0.05 cm^{-1} . Only the Raman spectra having intensity 10 counts higher than the background level have been subsequently selected. The next step has been the creation of two different matrices. The first

one is the matrix where the intensities of the peaks have been saved. This matrix has been used to identify the pixels belonging to the waveguide cross section.

The second one is the matrix where Raman shifts have been saved after the correction to remove shifts caused by the mechanical instability as well as instability of the laser and/or the spectrometer by means of the Rayleigh line peak position. After that, this Raman shift matrix has been used to calculate the Raman peak shift. The calculation has been done working with the column of the matrix and computing the Raman peak shift ($\Delta\omega$) as the difference between the Raman frequency ω of the elements of each column and the mean value ω_0 of the last five elements of every column corresponding to the Raman peak wavenumbers of the unstrained silicon.

In order to build the stress maps with relatively small errors in the cross section dimensions, particularly at the edges of waveguides, the $0.5 \mu\text{m}$ size of laser focal spot in the micro-Raman measurements has to be taken into account. Assuming a perfect rectangular shape of the waveguide cross section (boxcar function $H = \theta(x) - \theta(x-w)$, where θ is the Heaviside function and w is the waveguide width) and a Gaussian profile of the laser beam (G), a convolution between the boxcar and the Gaussian function has been calculated for a $2.33 \mu\text{m}$ wide waveguide (Fig. 2.8.a) and for a $10.7 \mu\text{m}$ wide waveguide (Fig. 2.8.b).

Based on the convolution results an intensity threshold for the scattered light has been fixed at about half of the mean value of the intensity maxima measured at each map column. Considering this threshold, pixels of waveguide cross-section maps with lower intensities have been neglected.

The selection of pixels used to generate the maps is sketched out in Fig. 2.8.c. The solid black line indicates the area of the waveguides cross section where the intensity of the scattered line is higher than the fixed threshold. The pixels out of this region have been neglected obtaining a well define shape of the waveguide cross section as shown in Fig. 2.8.d, where the map of Raman peak shift is reported. As a result, the pixels that are located mainly in the central part of waveguide are taken into account for the analysis of the maps presented in the forthcoming sections.

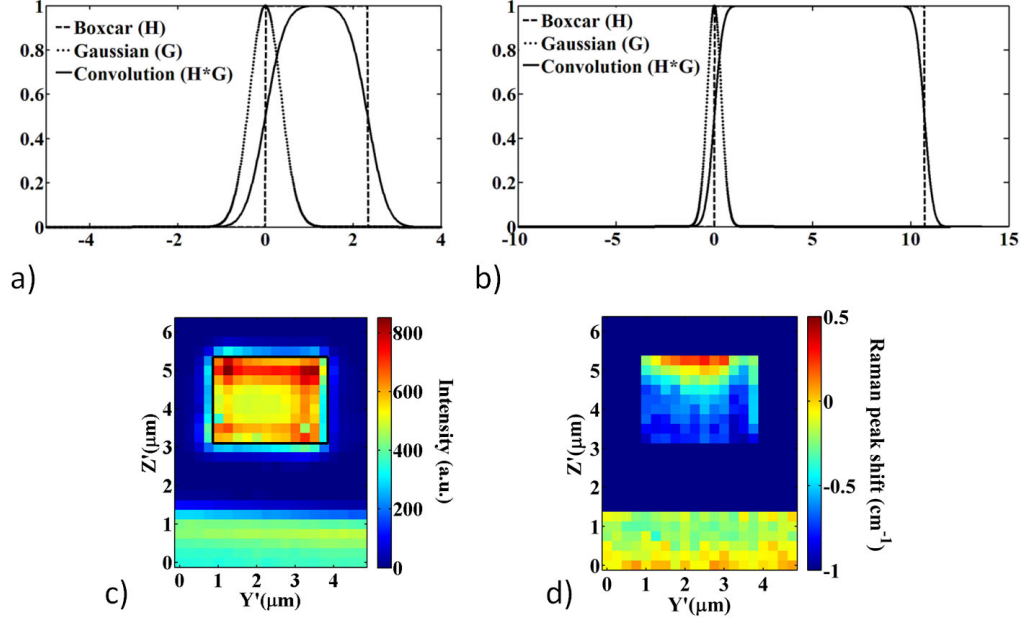


Figure 2.8: a-b) Estimation of intensity threshold. The plot shows the convolution (solid line) between a Gaussian function (dotted line) representing the laser beam with a boxcar function (dashed line) representing the cross section of the waveguide for (a) 2.33 μm wide waveguide and (b) 10.7 μm wide waveguide; c) intensity map of the scattered light. The solid black line indicates the waveguide area found by selecting only the pixels with the intensity of scattered light higher than a threshold value; d) map of the Raman peak shift [67].

B. Stress tensor determination accuracy

The stress tensor element evaluation has been performed by solving Eq. 2.3.17 for every scanned area. This equation depends both on the measured $\Delta\omega_i$ values and the knowledge of the compliance tensor elements (S_{ij}) and the phonon deformation potentials p, q and r. Therefore, the overall accuracy of the stress tensor determination is imposed by the experimental error related to the micro-Raman measurement and by the accuracy of the silicon deformability-related parameters.

In the presented experiment, the main error sources have been the spectral resolution and the environmental conditions. Although neither the resolution of the spectrometer nor the pixel density of the CCD are particularly high, the repeatability of the spectral measurements is excellent because of the high signal-to-noise

	PDPs of Chandrasekhar et al. [78]	PDPs of Anastassakis et al. [74]
p/ω_0^2	-1.49 ± 0.07	-1.85 ± 0.06
q/ω_0^2	-1.97 ± 0.09	-2.31 ± 0.06
r/ω_0^2	-0.61 ± 0.03	-0.71 ± 0.02

Table 2.2: The most common values of silicon phonon deformation potentials used in literature.

ratio ($\sim 10^3$). As a result, by fitting the Raman spectra with a Lorentzian function, the central position of the silicon Raman peak has been extracted with a resolution lower than 0.05 cm^{-1} , as mentioned before. Moreover, the Rayleigh scattering line used as internal reference has allowed to evaluate the shift of the silicon Raman peak induced only by the applied stress, because it is sensitive to the overall setup stability but insensitive to strain inside the sample [68].

To evaluate the stress sensitivity of the measurements, Eq. 2.3.17 can be used to show that a 0.05 cm^{-1} Raman peak shift corresponds to a minimal detectable stress of about 25 MPa.

Unlike the elastic constants (S_{ij}) that have been measured with high accuracy and confirmed by several independent measurements [71–73], the phonon deformation potentials (PDPs) are known with less accuracy. The reason for this uncertainty has been widely discussed (see for example Ref. [74–77]). The causes have been found into the methods used for the values extraction and in the experimental conditions, e.g. different excitation wavelengths, methods for the stress application, environmental conditions and measurement techniques. Therefore, in the literature an universal agreement on PDPs values is absent and two sets of values are commonly used [74, 78]. As it can be seen in Table 2.2, these values differ by up to 20% and, therefore, they cause uncertainty on the stress values derived by the Raman measurements. In fact, by making use of Eq. 2.3.17 and the $\Delta\omega_i$ values measured in a scan line along the Z' direction and by evaluating the σ'_{YY} -profile with the two sets of PDP values reported in Table 2.2 (see Fig. 2.9), the maximum difference has

been quantified to be approximately 13%.

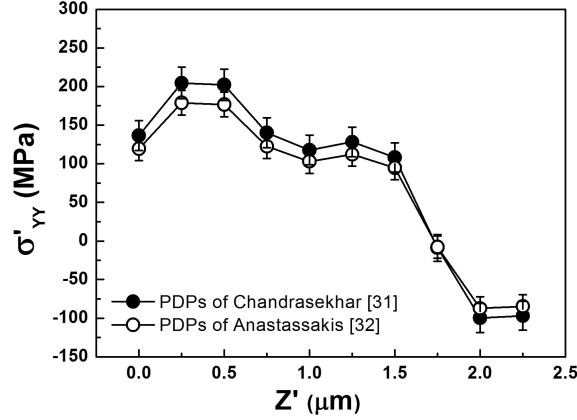


Figure 2.9: σ'_{YY} -profile along Z' evaluated with PDP values of Chandrasekhar [78] (full circle) and PDP values of Anastassakis [74] (empty circle). The error bars have been calculated by error propagation taking into account the experimental errors of $\Delta\omega_3$ and PDP values [67].

Very recently, Miyatake et al. [77] has revisited the measurements of PDP and confirmed the experimental values reported in [74]. Therefore, by substituting the S_{ij} and PDPs values of [74] in Eq. 2.3.17, the relation between the Raman peak shift ($\Delta\omega_i$) and σ'_{YY} stress tensor component is reduced to

$$\Delta\omega_1 = -1.04\sigma'_{YY} \times 10^{-12}\omega_0 \quad (2.3.19a)$$

$$\Delta\omega_2 = -5.54\sigma'_{YY} \times 10^{-12}\omega_0 \quad (2.3.19b)$$

$$\Delta\omega_3 = -4.42\sigma'_{YY} \times 10^{-12}\omega_0 \quad (2.3.19c)$$

Hence, by taking into account the experimental errors and the uncertainty of the PDPs values, the accuracy of stress determination in this thesis can be quantified to 15%.

2.4 Stress characterization experimental results

The micro-Raman experiments have been performed in two different configurations. In the first, no polarization settings for incident and scattered light have been used.

In the second, polarization-dependent measurements have carried out to determine quantitatively the stress tensor element.

2.4.1 Unpolarized measurements

In this experiment, only one Raman peak has been observed in each scanned area (Fig. 2.8.b). Thus, the stress-induced splitting of phonon frequencies is within the resolution of the experimental apparatus. For unpolarized measurement this means that the observed frequency shift ($\Delta\omega_{obs}$) is the weighted average of the individual peak shifts ($\Delta\omega_i$) with their relative intensities (I_i) [77, 79]

$$\Delta\omega_{obs} = \frac{\sum_{i=1}^3 \Delta\omega_i I_i}{\sum_{i=1}^3 I_i} \quad (2.4.1)$$

In the studied configuration and within the uniaxial stress approximation (see Eq. 2.3.19), $\Delta\omega_{obs}$ is linearly proportional to the effective stress experienced by the TO phonons:

$$\Delta\omega_{obs} = \frac{\Delta\omega_2 I_2 + \Delta\omega_3 I_3}{I_2 + I_3} = -C\sigma'_{YY}\omega_0 \times 10^{-12} \quad (2.4.2)$$

Hence, the uniaxial stress can be deduced from the measured $\Delta\omega_{obs}$ within an accuracy to some constant positive prefactor $C=(5.54I_2+4.42I_3)/(I_2+I_3)$.

By calculating σ'_{YY} with Eq. 2.4.2, the two-dimensional maps of stress distribution for different waveguide widths of the **SOI0** (waveguide without stressing layer), **SOI1** (waveguide stressed by a tensile stressing SiN overlayer), **SOI2** (waveguide stressed by a compressive stressing SiN overlayer) and **SOI3** (waveguide with a stress-compensated SiN overlayer) samples have obtained.

As shown in Fig. 2.10, for the same type of samples the maps are qualitatively similar, independently on the width of the waveguides. These results show the repeatability of the stress variations related to the same deposition procedure of SiN films.

Instead, analysing in details each type of sample, one can see that the reference **SOI0** waveguides (Fig. 2.10.a,b) are characterized by a small tensile-like deformation ($\sigma'_{YY} > 0$), which is visibly higher in the vicinity of the interface with SiO₂.

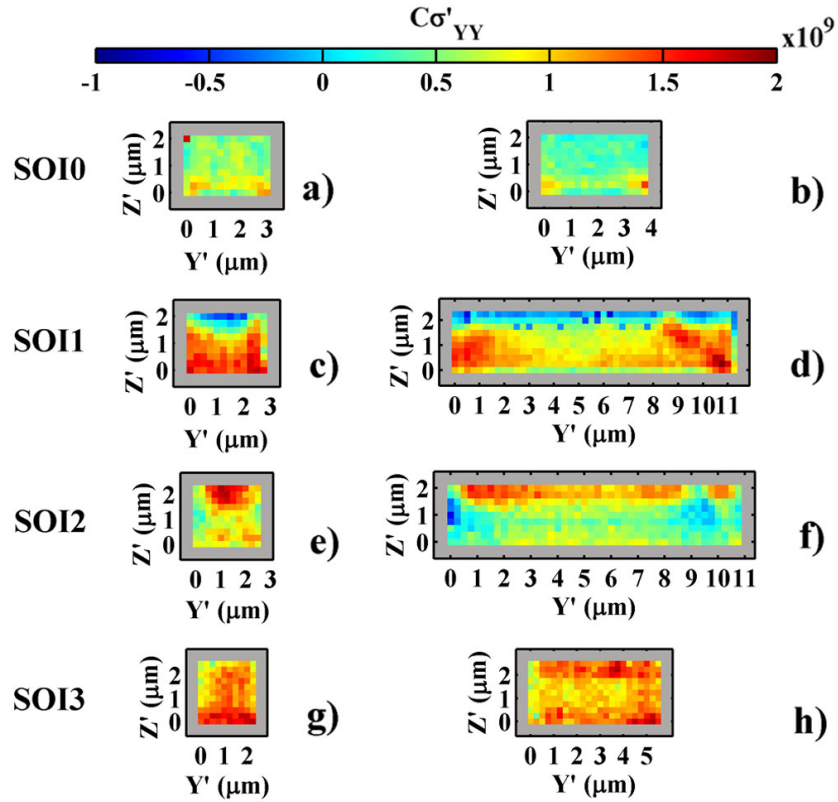


Figure 2.10: Stress maps ($C\sigma'_{YY}$) measured for different widths of SOI waveguides: a-b) without SiN claddings (SOI0), c-d) with a tensile SiN stressing cladding (SOI1), e-f) with a compressive SiN stressing cladding (SOI2), g-h) with a compensated SiN stressing cladding (SOI3) [67].

Thus, the BOX acts like a stressing layer but its effect is weaker compared to the deformations caused by the SiN films in the other samples. Most of the stress appears on the edges of the maps, but overall the waveguide is unstrained. Hence, the reference samples show that a residual stress exerted by the SiO_2 is present and so the BOX layer may have a relevant role in the stressing of the silicon waveguide, as it will be show in the other samples.

The stress maps change when a stressing SiN overlayer is deposited on the silicon waveguide. In the **SOI1** waveguides (Fig. 2.10.c,d), a non-uniform stress distribution is observed. It changes from being compressive ($\sigma'_{YY} < 0$) near the silicon/silicon nitride interface to being tensile ($\sigma'_{YY} > 0$) near the interface silicon/BOX. This result reveals clearly a breaking of silicon crystal symmetry due to

the presence of a non-zero stress-gradient in the Z' -direction. Moreover, the tensile stress due to the Si_3N_4 layer is higher at the edges of the waveguide with respect to the center. This result is in agreement with simulations and measurements reported in literature [66,68,80] for similar structures. Note that the combined action of the stressing overlayer and of the BOX layer causes a deep penetration of the stress in the core of the waveguide. An effect which is observed both for the narrow as well as for the wide waveguides.

The **SOI2** samples (Fig. 2.10.e,f), prepared by PECVD method, are characterized by a more uniform stress distribution, mainly of tensile type. This is due to the concurrent action of the stressing overlayer and of the BOX layer which have both the same kind of stress. However, since the induced stress is different for the two layer, a stress-gradient is present: the stress is visibly larger at the top than at the bottom of the waveguide. Thus, the stress increases long the waveguide cross-section, contrary to the case of the SOI1 samples. Note that the stress in the central part of the waveguide is weaker for the wide waveguide than for the narrow waveguide. In fact, the wide waveguide shows an almost unstrained central region.

The nominally stress-compensated **SOI3** samples (Fig. 2.10.g,h) have a stress distribution radically different from the unstrained SOI0 samples. SOI3 samples show the most uniform stress distribution in the waveguide core among all studied waveguides. Hence, the strain-gradient is smaller compared to the other two types of samples.

Simulations of the the stress distribution in these samples carried out with a finite element analysis (COMSOL Multiphysics) by C. Schriever of the SiLi-nanoMartin group from Luther-Universität (Halle-Wittenberg) have shown a qualitative agreement with the experimental maps.

2.4.2 Polarized measurements

Polarized micro-Raman experiments have been carried out on the wide **SOI1** waveguide in order to determine quantitatively the stress tensor element and, then, calcu-

late the strain tensor elements by means of the Hooke's law. An optical polarizer has been added to the experimental setup selecting the same polarization for incident and back-scattered light, i.e. $\mathbf{e}_0 \parallel \mathbf{e}_s$. The measurements have been performed using light polarized parallel to the Y' -axis. According to the polarization selection rules (see Eq. 2.3.8 and Eq. 2.3.2) only the scattering from the third phonon is observed in this configuration, as shown in Fig. 2.11.

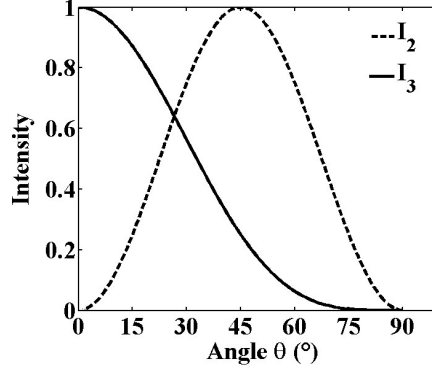


Figure 2.11: Selection rules for the intensity Raman peak components (I_i) versus angle (θ), which is the angle between the polarization direction and the direction $Y'=[-110]$. Choosing the direction at 0 degree as the polarization parallel to $Y'=[-110]$, the angle dependent selection rules are estimated by using the rotated polarization unit vectors $\mathbf{e}_0 \parallel \mathbf{e}_s = \mathbf{e}(\theta)$. Hence, $I_1 = 0$, $I_2 \propto \sin^2(2\theta)$ (dashed line) and $I_3 \propto \cos^4(\theta)$ (solid line) in d^2 units [67].

By using Eq. 2.3.16, the strain components ϵ'_{XX} , ϵ'_{YY} and ϵ'_{ZZ} have been calculated and their resulting distribution maps are shown in Fig. 2.12. The ϵ'_{XX} component is negligible in comparison to the other two strain components. This is because only a near plane stress is investigated in the Raman measurements. Since an uniaxial stress model is considered, the ϵ'_{YY} component is dominant in the system and has a distribution similar to the stress map shown in Fig. 2.10d. It is interesting to note also that qualitatively ϵ'_{YY} and ϵ'_{ZZ} are characterized by complementary variations. This is explained by the theory of elasticity according to which a material compressed in one direction, usually tends to expand in the other perpendicular directions and vice versa, as described in Sec. 2.1.

Interestingly, when comparing the stress maps obtained through unpolarized and

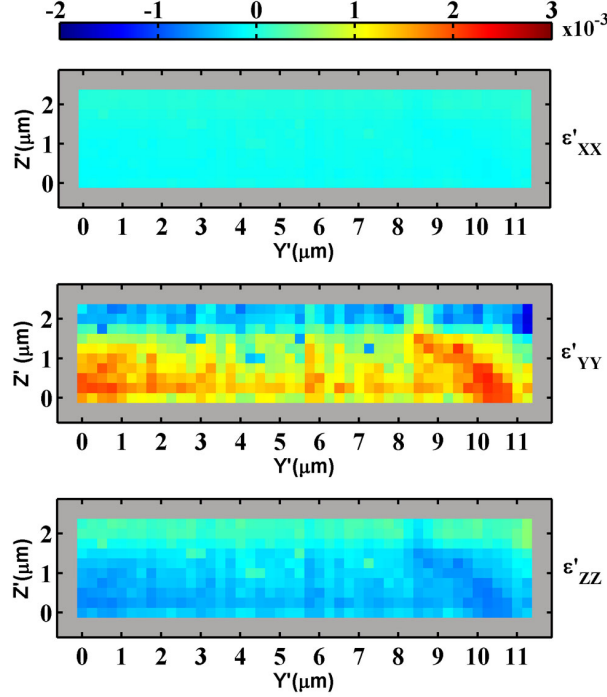


Figure 2.12: Maps of strain tensor components, ϵ'_{XX} , ϵ'_{YY} and ϵ'_{ZZ} , calculated by means of Hooke's law for SOI1 sample [67].

polarized Raman measurements the unknown factor C in Eq. 2.4.2 has been found almost constant with a mean value of $(4.7 \pm 1.3) \text{ Pa}^{-1}$. As a result, this C factor value can be used to estimated more quantitatively the ϵ'_{YY} distribution also in the case of unpolarized measurements.

2.5 Conclusions

In this chapter the mechanical stress resulting from the deposition of a thin film on a thicker substrate has been described. The extent and the sign of the stress in the film depend on the technique of deposition and, in particular, on process steps. Two main stress components are present: the extrinsic component, which is mainly caused by the thermal expansion coefficients mismatch, and the intrinsic component, which is determined by physical and chemical changes during the deposition process. The particular cases of silicon oxide and silicon nitride thin overlayers have been studied.

It has been shown that silicon oxide has mainly a tensile stress when it is deposited on silicon, while the extent and the sign of the stress inside a silicon nitride film can be varied by using two deposition techniques (LPCVD and PECVD) and different recipes.

Two standard stress measurement methods have been also described discussing their advantages and limitations. The curvature method estimates the stress magnitude from the curvature radius of the wafer bending caused by the relaxation of the stress film. Instead, the X-ray diffraction method provides information on the variation of the lattice constant in presence of strain from the X-ray diffraction pattern.

A more detailed description of the micro-Raman spectrometry applied for stress characterization has been presented. The micro-Raman is a non-destructive technique that allows to map with micrometer spatial resolution the distribution of the local stress by measuring the Raman peak shift induced by the stress.

The general mathematical model that relates the Raman frequency shift with the stress tensor elements has been explained. The particular case of a stressed (001) silicon has been discussed showing the calculated relation between the Raman frequency shift measured in backscattering from the (110) plane and the stress component σ'_{YY} of the assumed uniaxial stress model.

Finally, the distributions of mechanical stress in SiN_x/SOI waveguides on the waveguide facets for unpolarized measurements have been shown. In particular, different deposition techniques, such as LPCVD and PECVD, have been investigated pointing out the completely different stress variations in the waveguide that they cause. It is worthwhile noting that a relevant role in the determination of the stress and of its distribution is also played by the BOX which indeed affects strongly the strain of the silicon waveguide. Hence, the combined action of the silicon nitride overlayer and the silicon oxidized buried layer strains the whole silicon core of the waveguides.

From an application point of view, the non-uniform stress distributions corre-

sponding to a non-uniform strain distribution, reveal the breaking of the silicon centro-symmetry and, hence, the observation of a non-zero second order susceptibility ($\chi^{(2)}$) may be expected.

Chapter 3

Second harmonic generation in strained silicon waveguides

Thanks to the ability of silicon to amplify, generate and process optical signals by means of nonlinear optical phenomena, nonlinear silicon photonics is a promising technology still in development. However, due to its centrosymmetry, silicon lacks second order nonlinearity, which is an essential component of nonlinear optics. Previous studies have shown how, by making use of a mechanical deformation, this nonlinearity could be enhanced at the silicon surface or in the bulk of silicon waveguides, where the linear electro-optics effect has been demonstrated [42, 43].

In this chapter the experimental results of all optical experiments carried out in strained silicon waveguides, where the strain-induced $\chi^{(2)}$ has been reflected in pump light spectral conversion by means of a Second Harmonic Generation (SHG) process, are presented.

Before discussing the experimental results, the first two sections briefly introduce the basic concepts of nonlinear optics and the generation of a second harmonic (SH) signal, where the problem of the material dispersion, that limits the efficiency of the phenomenon, and the relative common solutions are discussed. Subsequently, a brief overview of the SHG process in silicon is given, describing in particular the enhancement of the SH signal by means of mechanical stress. Finally, the details of

the set-ups and the experimental results are presented and discussed.

3.1 Introduction to nonlinear optics

As definition, *nonlinear optics is the study of phenomena that occur as a consequence of the modification of the optical properties of a material system by the presence of the light* [81]. Therefore, the nature of the modified optical properties of the medium is strongly determined by the characteristics of the interacting light and the specific material that constitutes the medium.

The general theory describing the interaction of the light with the matter is based on the wave equation for the propagation of the light through a nonlinear optical medium derived by the Maxwell equations. Assuming a nonmagnetic, electrically neutral (no free charge, $\tilde{\rho} = 0$) and nonconducting (no free current, $\tilde{\mathbf{J}} = 0$) medium, the optical wave equation assumes the general form [81]

$$\nabla \times \nabla \times \tilde{\mathbf{E}} + \frac{1}{c^2} \frac{\partial^2 \tilde{\mathbf{E}}}{\partial t^2} = -\frac{1}{\varepsilon_0 c^2} \frac{\partial^2 \tilde{\mathbf{P}}}{\partial t^2} \quad (3.1.1)$$

where c is the speed of light in vacuum, ε_0 is the permittivity of free space and $\tilde{\mathbf{P}}$ is the polarization vector that is induced inside the medium by the presence of the electric field $\tilde{\mathbf{E}}^1$ of the propagating light.

Thanks to the curl property for which $\nabla \times \nabla \times = \nabla(\nabla \cdot) - \nabla^2$, the form of Eq. 3.1.1 can be simplified. In fact, although in nonlinear optics the term $\nabla \cdot \tilde{\mathbf{E}}$ does not vanish because of the general relation between the vector $\tilde{\mathbf{D}}$ and $\tilde{\mathbf{E}}$ ($\tilde{\mathbf{D}} = \varepsilon_0 \tilde{\mathbf{E}} + \tilde{\mathbf{P}}$), if the amplitude of the electric field is slowly varying compared to the rapidly oscillating part of the wave, the first term on the left-side of Eq. 3.1.1 can be considered negligible. Under such assumption, the wave equation takes the simplified form

$$\nabla^2 \tilde{\mathbf{E}} - \frac{1}{c^2} \frac{\partial^2 \tilde{\mathbf{E}}}{\partial t^2} = \frac{1}{\varepsilon_0 c^2} \frac{\partial^2 \tilde{\mathbf{P}}}{\partial t^2} \quad (3.1.2)$$

¹The tilde (\sim) denotes a quantity that varies rapidly in time.

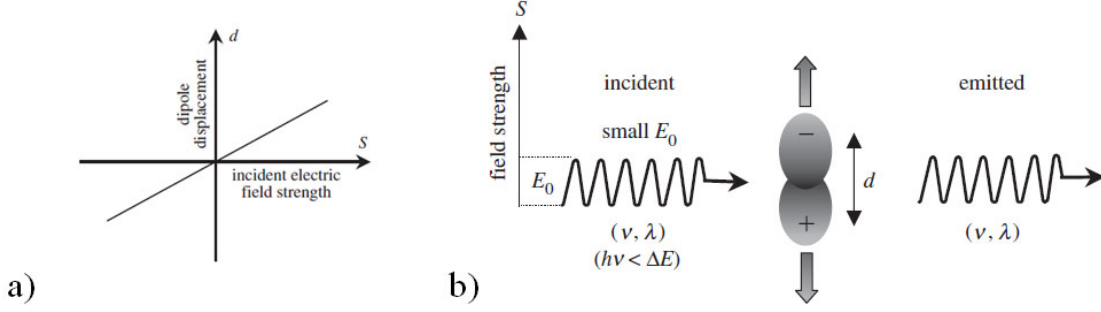


Figure 3.1: Medium linear optical response: a) dipole displacement as a function of the electric field strength; b) due to the linear response the dipole emits a radiation with the same frequency of the incident light, when the propagation is within the medium transparency range ($h\nu < \Delta E$, where ΔE is the energy that must have a photon to be absorbed by the medium). Adapted from [82].

In linear optics regime, i.e. when the light intensity is small, the induced dipole moment per unit volume $\tilde{\mathbf{P}}$ in the right-side of Eq. 3.1.2 is linearly dependent on the local value of the electric field strength as

$$\tilde{\mathbf{P}} = \tilde{\mathbf{P}}_1 = \varepsilon_0 \chi^{(1)} \tilde{\mathbf{E}} \quad (3.1.3)$$

where $\chi^{(1)}$ is the tensor of rank two describing the linear part of the susceptibility of the medium. The effects of this polarization are included through the refractive index and the attenuation coefficient.

Within this regime, the atoms of the medium respond to the applied electric field creating an oscillating dipole moment, whose displacement is linearly dependent on the strength of the electric field (Fig. 3.1.a). As a result, the dipoles emit a radiation with the same frequency of the interacting light (Fig 3.1.b).

Contrarily, when the electric field has intensity sufficiently high, the medium polarization $\tilde{\mathbf{P}}$ possesses an additional component that nonlinearly depends on the strength of the electric field ($\tilde{\mathbf{P}}_{NL}$). Therefore, $\tilde{\mathbf{P}}$ can be written as

$$\tilde{\mathbf{P}} = \tilde{\mathbf{P}}_1 + \tilde{\mathbf{P}}_{NL} \quad (3.1.4)$$

In presence of this component, the wave equation for an isotropic dispersionless

material assumes the form [81]

$$-\nabla^2 \tilde{\mathbf{E}} + \frac{\varepsilon^{(1)}}{c^2} \frac{\partial^2 \tilde{\mathbf{E}}}{\partial t^2} = -\frac{1}{\varepsilon_0 c^2} \frac{\partial^2 \tilde{\mathbf{P}}_{NL}}{\partial t^2} \quad (3.1.5)$$

where $\varepsilon^{(1)}$ is the relative permittivity of the medium and $\tilde{\mathbf{P}}_{NL}$ can be expanded in power series of the electric field as

$$\tilde{\mathbf{P}}_{NL} = \varepsilon_0 (\chi^{(2)} \tilde{\mathbf{E}} \tilde{\mathbf{E}} + \chi^{(3)} \tilde{\mathbf{E}} \tilde{\mathbf{E}} \tilde{\mathbf{E}} + \dots) \quad (3.1.6)$$

where $\chi^{(2)}$ is the second order of the nonlinear susceptibility, that is a tensor of rank three, and $\chi^{(3)}$ is a tensor of fourth-rank related to the third order of the nonlinear susceptibility.

In this regime, the inhomogeneous term $\partial^2 \tilde{\mathbf{P}}_{NL} / \partial t^2$ of Eq. 3.1.5 can be interpreted as a radiation source term. In fact, it establishes that the charges of the material suffer an acceleration by the electric field, therefore, according to the Larmor's theorem, they represent a source of new electromagnetic radiations. In terms of dipole emission, the displacement is no longer linear, so that a dipole irradiation occurs not only at the frequency of the input light, but also at higher and lower frequencies (Fig. 3.2). This implies that in presence of a nonlinear response of the material the propagation of an intense light induces the generation of new spectral components.

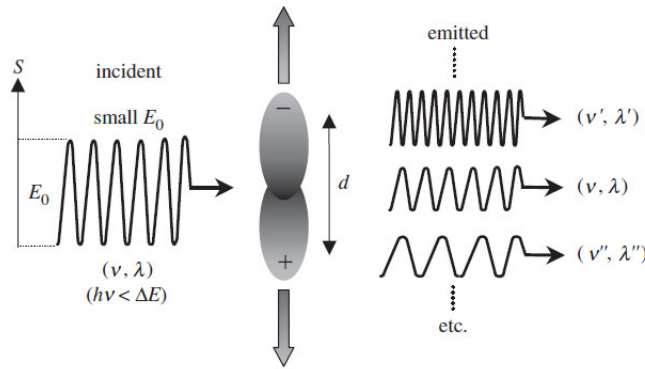


Figure 3.2: The nonlinear optical response of the medium determines the dipole emission of additional radiations with frequencies different from incident light [82].

It is worth noting that in the case of nonlinear regime the dipole displacement is imposed by the specific crystallographic orientation of material. Therefore, the nature of nonlinear optical phenomena occurring in the medium are determined by its structural properties.

The nonlinear media can be distinguished into two main categories, the *centrosymmetric* and the *non-centrosymmetric* materials, on the basis whether or not the material possesses a center of inversion symmetry.

A simple model that allows to explain the differences in the behavior of these two categories is the Lorentz model of the atom. Treating the atoms as harmonic oscillators, this model is generally able to describe the linear optical properties of a non-metallic material. However, by introducing nonlinearities in the restoring force exerted on the electron, it can be extended for describing also the nonlinear optical properties.

Hence, in a non-centrosymmetric medium the electronic restoring force can be given in scalar approximation as [81]

$$\tilde{F}_{res} = -m\omega_0^2\tilde{x} - ma\tilde{x}^2 \quad (3.1.7)$$

where a is the parameter that quantifies the strength of the nonlinearity in the electron displacement \tilde{x} . Then, the corresponding potential energy function is described by [81]

$$U(\tilde{x}) = \frac{1}{2}m\omega_0^2\tilde{x}^2 + \frac{1}{3}ma\tilde{x}^3 \quad (3.1.8)$$

As a result, the actual potential energy function deviates from a perfect parabola (Fig. 3.3.a) and contains even and odd powers of \tilde{x} . Hence, this potential is such that $U(\tilde{x}) \neq U(-\tilde{x})$.

Instead, in case of centrosymmetric media, the restoring force has the form [81]

$$\tilde{F}_{res} = -m\omega_0^2\tilde{x} + mb\tilde{x}^3 \quad (3.1.9)$$

where b is the parameter that quantifies the strength of the nonlinearity. The

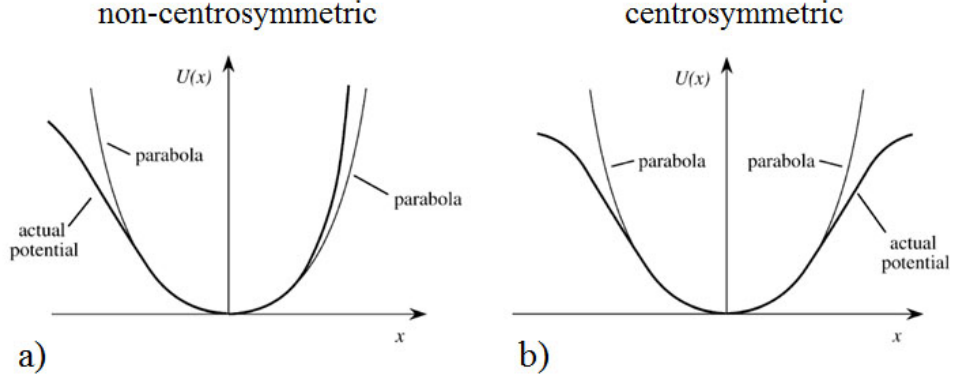


Figure 3.3: Potential energy function for a) a non-centrosymmetric and b) a centrosymmetric material [81].

potential energy function related to this restoring force is then [81]

$$U(\tilde{x}) = \frac{1}{2}m\omega_0\tilde{x}^2 - \frac{1}{4}mb\tilde{x}^4 \quad (3.1.10)$$

In this case, the potential energy function is maintained parabolic (Fig. 3.3.b), so that it is symmetric under spatial inversion $\tilde{x} \rightarrow -\tilde{x}$: $U(\tilde{x}) = U(-\tilde{x})$, because $-mb\tilde{x}^4/4$ represents the lowest-order correction term to the parabolic potential.

Based on these considerations, in electric-dipole approximation a non-centrosymmetric material can support both even and odd orders of nonlinear phenomena, whereas the lowest order of nonlinearity possible in a centrosymmetric medium is related to the third order of the nonlinear susceptibility. In fact, if the second order nonlinear polarization in scalar approximation is considered

$$\tilde{P}_2(t) = \varepsilon_0\chi^{(2)}\tilde{E}^2(t) \quad (3.1.11)$$

and if the sign of the electric field is changed, due to the inversion symmetry of the medium, the sign of the polarization also changes:

$$-\tilde{P}_2(t) = \varepsilon_0\chi^{(2)}[-\tilde{E}(t)]^2 \quad (3.1.12)$$

that can be rewritten as

$$-\tilde{P}_2(t) = \varepsilon_0\chi^{(2)}\tilde{E}^2(t) \quad (3.1.13)$$

Therefore, if Eq. 3.1.11 and Eq. 3.1.13 are compared, the two polarizations should be equal, thus $\tilde{P}_2(t)$ must be equal to zero. The only possibility to have such condition is when the second order of the nonlinear susceptibility $\chi^{(2)}$ vanishes [81].

3.1.1 Properties of the nonlinear susceptibility

Due to the tensorial nature, the nonlinear susceptibility possesses formal symmetry properties, whereas its non-zero elements are determined by the symmetry properties of the medium.

In a dispersive material the electric field and the nonlinear polarization must be represented as the sum of the various spectral components as

$$\tilde{\mathbf{E}}(\mathbf{r}, \mathbf{t}) = \sum_n \tilde{\mathbf{E}}_n(\mathbf{r}, \mathbf{t}) = \sum_{\mathbf{n}} \mathbf{E}_{\mathbf{n}}(\mathbf{r}) e^{-i\omega_{\mathbf{n}}\mathbf{t}} + \text{c.c.} \quad (3.1.14)$$

$$\tilde{\mathbf{P}}^{NL}(\mathbf{r}, \mathbf{t}) = \sum_n \tilde{\mathbf{P}}_n^{NL}(\mathbf{r}, \mathbf{t}) = \sum_{\mathbf{n}} \mathbf{P}_{\mathbf{n}}^{NL}(\mathbf{r}) e^{-i\omega_{\mathbf{n}}\mathbf{t}} + \text{c.c.} \quad (3.1.15)$$

in this way, the second order nonlinear polarization can be written in tensorial form as [81]

$$P_i(\omega_n + \omega_m) = \varepsilon_0 \sum_{jk} \sum_{(nm)} \chi_{ijk}^{(2)}(\omega_n + \omega_m, \omega_n, \omega_m) E_j(\omega_n) E_k(\omega_m) \quad (3.1.16)$$

where i, j, k are the Cartesian coordinates components of the fields and (n,m) denotes the summation over n and m for a fixed sum $\omega_n + \omega_m$.

Reality of the field

Since both the nonlinear polarization and the electric field are purely real quantity, the second order nonlinear susceptibility has the property that [81]

$$\chi_{ijk}^{(2)}(-\omega_n - \omega_m, -\omega_n, -\omega_m) = \chi_{ijk}^{(2)}(\omega_n + \omega_m, \omega_n, \omega_m)^* \quad (3.1.17)$$

Intrinsic permutation symmetry

Since the indices j, k, m and n are arbitrary, they can be interchanged, so that [81]

$$\chi_{ijk}^{(2)}(\omega_n + \omega_m, \omega_n, \omega_m) = \chi_{ikj}^{(2)}(\omega_n + \omega_m, \omega_m, \omega_n) \quad (3.1.18)$$

Full permutation symmetry

If the Cartesian indices are simultaneously interchanged, all the frequency arguments can be freely interchanged [81]

$$\chi_{ijk}^{(2)}(\omega_3 = \omega_1 + \omega_2) = \chi_{jki}^{(2)}(-\omega_1 = \omega_2 - \omega_3) \quad (3.1.19)$$

$$= \chi_{kij}^{(2)}(\omega_2 = \omega_3 - \omega_1) \quad (3.1.20)$$

$$= \chi_{jki}^{(2)}(\omega_1 = -\omega_2 + \omega_3) \quad (3.1.21)$$

Kleinman's symmetry

If the applied fields have frequencies much smaller than the resonance frequency ω_0 , the $\chi^{(2)}$ can be assumed frequency independent, therefore the Cartesian indices can be permuted without the interchange of the frequencies. This property is valid only in case of a dispersiveless medium [81]

$$\chi_{ijk}^{(2)}(\omega_3 = \omega_1 + \omega_2) = \chi_{jki}^{(2)}(\omega_3 = \omega_1 + \omega_2) = \chi_{kij}^{(2)}(\omega_3 = \omega_1 + \omega_2) \quad (3.1.22)$$

$$= \chi_{ikj}^{(2)}(\omega_3 = \omega_1 + \omega_2) = \chi_{jik}^{(2)}(\omega_3 = \omega_1 + \omega_2) \quad (3.1.23)$$

$$= \chi_{kji}^{(2)}(\omega_3 = \omega_1 + \omega_2) \quad (3.1.24)$$

Contracted notation

When the Kleinman's symmetry is valid, the second order susceptibility is generally substituted by a tensor d_{ijk} , called *nonlinear coefficient*, through the relation

$$d_{ijk} = \frac{1}{2}\chi_{ijk} \quad (3.1.25)$$

where the factor 1/2 has historical origins [81]. In this way, the second order nonlinear polarization becomes

$$P_i(\omega_n + \omega_m) = \varepsilon_0 \sum_{jk} \sum_{(nm)} 2d_{ijk} E_j(\omega_n) E_k(\omega_m) \quad (3.1.26)$$

Assuming the tensor d_{ijk} symmetric with respect the indices j, k, a contracted matrix notation d_{il} can be also introduced:

jk:	11	22	33	23,32	31,13	12,21
l:	1	2	3	4	5	6

Generally, for simplicity, the nonlinear coefficient is contracted from a tensor to a scalar quantity d_{eff} as follows [83]

$$d_{\text{eff}} = \hat{e}_3 \cdot \mathbf{d} : \hat{e}_1 \hat{e}_2^* \quad (3.1.27)$$

where \hat{e}_h with $h = 1, 2, 3$ are the unit vectors of the polarizations of the involved waves. Due to the permutation symmetry described before, this parameter quantifies the strength of any particular nonlinear interaction, that is thus determined by the polarizations of interacting waves and the geometry of the nonlinear medium.

3.2 Introduction to second harmonic generation

One of the possible nonlinear phenomena that occur inside a nonlinear non-centrosymmetric medium interacting with an intense travelling light is the second harmonic generation (SHG).

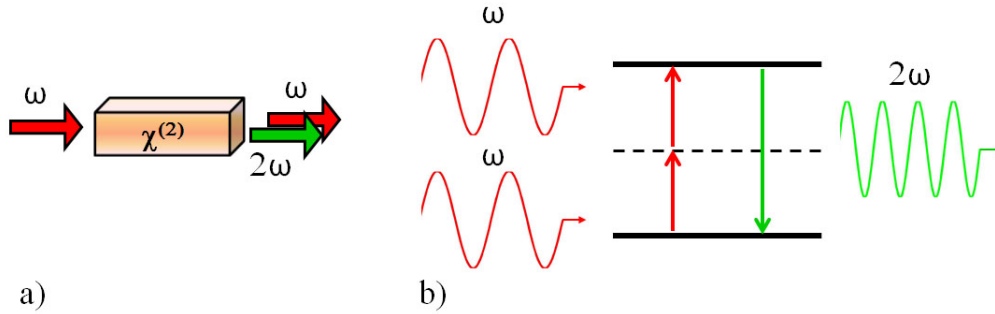


Figure 3.4: Second Harmonic Generation: a) geometry of the process; b) energy-level diagram describing the process. Two photons at frequency ω are annihilated by way of a virtual energy level (dash line) to create a single photon at frequency 2ω .

This process can be defined as the generation of a new spectral component with the half of the input optical wavelength (or with twice the input optical frequency)

(Fig. 3.4.a). Or else, with the quantum mechanical description, two photons of the input wave with frequency ω are destroyed and a new photon with frequency equal to 2ω is simultaneously created (Fig 3.4.b).

Let us consider a nonlinear material with propagation direction along the z-direction. The total electric field present inside the medium is

$$\tilde{E}(z, t) = \tilde{E}_\omega(z, t) + \tilde{E}_{2\omega}(z, t) \quad (3.2.1)$$

where each component is expressed in term of complex amplitude $E_i(z)$ with slowly varying amplitude $A_i(z)$ with $i = \omega, 2\omega$:

$$\tilde{E}_i(z, t) = E_i(z)e^{-i\omega_i t} + c.c. = A_i(z)e^{i(k_i z - \omega_i t)} + c.c. \quad (3.2.2)$$

where k_i is the propagation constant of the traveling wave relative to the medium with refractive index n_i at frequency ω_i .

Therefore, the nonlinear polarization is composed by two components

$$\tilde{P}_{NL}(z, t) = \tilde{P}_\omega(z, t) + \tilde{P}_{2\omega}(z, t) \quad (3.2.3)$$

where each component can be written as $\tilde{P}_i(z, t) = P_i(z)e^{-i\omega_i t} + c.c.$, with $i = \omega, 2\omega$.

Assuming a dispersiveless medium, so that the Kleinman's symmetry is valid, and fixing the geometry of the process, i.e. the waves polarizations and the propagation direction, the nonlinear polarization amplitude $P_i(z)$ can be written in term of the effective nonlinear coefficient d_{eff} as follows [81]

$$P_\omega(z) = 4\varepsilon_0 d_{\text{eff}} A_{2\omega} A_\omega^* e^{i(k_{2\omega} - k_\omega)z} \quad (3.2.4)$$

$$P_{2\omega}(z) = 2\varepsilon_0 d_{\text{eff}} A_{2\omega}^2 e^{2ik_\omega z} \quad (3.2.5)$$

As can be seen in Eq. 3.2.4, the amplitude of nonlinear polarization $P_\omega(z)$ depends on the slowly varying amplitude $A_{2\omega}$ of the SHG wave. This coupling between the fundamental and generated wave causes a variation of their amplitude as they propagate into the medium. The equations describing this effect is derived by substituting each competent $\tilde{E}_i(z, t)$ and $\tilde{P}_i(z, t)$ into the respective inhomogeneous

wave equations (Eq. 3.1.5). The obtained equations are called *coupled amplitude equations* and have the form [81]

$$\frac{dA_\omega}{dz} = \frac{2i\omega^2 d_{\text{eff}}}{k_\omega c^2} A_{2\omega} A_\omega^* e^{-i\Delta k z} \quad (3.2.6)$$

$$\frac{dA_{2\omega}}{dz} = \frac{4i\omega^2 d_{\text{eff}}}{k_{2\omega} c^2} A_\omega^2 e^{i\Delta k z} \quad (3.2.7)$$

where $\Delta k = 2k_\omega - k_{2\omega}$ is the parameter that quantifies the wavevector mismatch. In fact, because of the material dispersion, the wavevectors of the fundamental and SHG signal are different, so that the two waves travel into the medium with different speeds. From the microscopic point of view, this means that each atomic dipole does not oscillate in phase with the others, therefore the irradiated wave does not add constructively to the waves emitted by the other dipoles. On other words, during the propagation, the fundamental and the SHG fields periodically interchange energy, as they periodically go out of phase. In case of correct phase relation, energy is extracted from the fundamental wave and transferred to the generated SHG wave. As the waves propagate, the dispersion destroys the phase relation. Consequently, the energy transfer becomes less efficient, until the phase is shifted by π and the energy extraction changes direction, i.e. it flows from the SHG signal to the fundamental (Fig. 3.5.a). As a result, the intensity of the SHG signal does not rise while propagating through the nonlinear material, but periodically oscillates (Fig. 3.5.b).

The distance over which the SHG intensity reaches the maximum and the phase shift is equal to π is called *coherence length* (l_c) [81]

$$l_c = \frac{\pi}{\Delta k} \quad (3.2.8)$$

In condition of undepleted fundamental wave (i.e. its power remains approximately constant) and generic phase mismatch Δk , the conversion efficiency of the process can be determined by computing the optical power of the two waves:

$$P_i = \int I_i dS \quad (3.2.9)$$

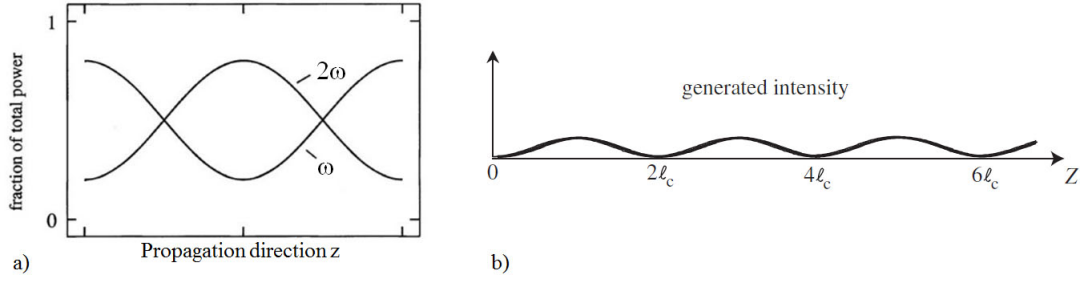


Figure 3.5: Second Harmonic Generation in unphase-matched conditions: a) as the two wave propagate along the medium, they exchange energy. The direction of the transfer periodically oscillates according to the phase relation established by the medium dispersion. Adapted from [81]; b) the SHG intensity oscillates between a minimum when $z = 2nl_c$ and a maximum when $z = (2n+1)l_c$, where n is an integer number and l_c is the coherence length [82].

where I_i with $i = \omega, 2\omega$ is the intensity of each interacting wave obtained by solving Eq. 3.2.6 and S is the area of the beam.

Hence, the conversion efficiency is given by [83]

$$\eta = \frac{P_{2\omega}}{P_\omega} = \frac{8 \pi^2 d_{\text{eff}}^2 L^2 P_\omega}{\varepsilon_0 n_\omega^2 n_{2\omega} c \lambda_\omega^2 S} \frac{\sin^2(\frac{\Delta k L}{2})}{(\frac{\Delta k L}{2})^2} = \eta_0 \text{sinc}^2(\frac{\Delta k L}{2}) \quad (3.2.10)$$

where n_ω and $n_{2\omega}$ are the refractive indices of the fundamental and SHG waves, respectively, λ_ω is the fundamental wavelength and L is the length of the medium.

Because of the presence of the term $\text{sinc}^2(\Delta k L/2)$, the conversion efficiency results strongly dependent on the wavevector mismatch Δk of the interacting waves. In fact, as illustrated in Fig. 3.6.a, the squared-sinc function is characterized by a main maximum at $\Delta k L/2 = 0$ and other maxima for $\Delta k L/2 \neq 0$, that are much lower intense. This implies that for $\Delta k \neq 0$ the conversion efficiency of the process is drastically reduced from its maximum value η_0 (Fig. 3.6.b). The range of $\Delta k L/2$ values, where the squared-sinc function is reduced to 0.5, is identified as the *phase matching bandwidth*, i.e. the range of values of wavevector mismatch such that $\Delta k_{BW} = 2.784/L$ [83].

Based on these consideration, an efficient interaction between the fundamental and the generated signal can be achieved only if the phase mismatch is controlled and compensated. Nowadays, there are many techniques that allow to achieve the phase

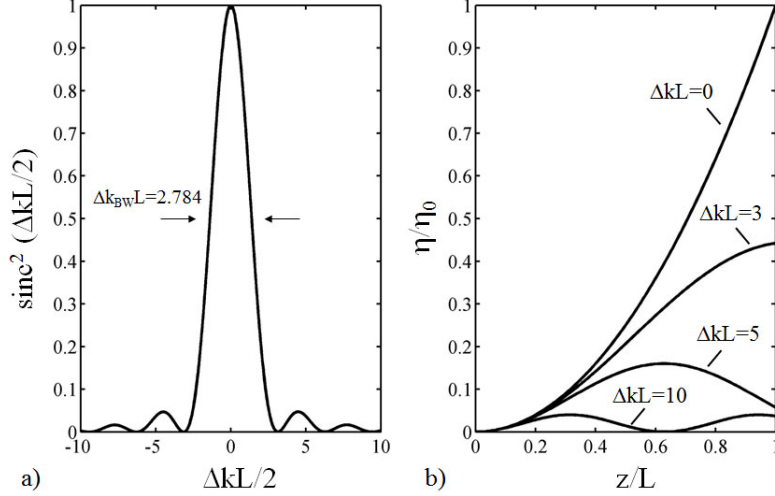


Figure 3.6: Second Harmonic Generation in unphase-matched conditions: a) plot of the sinc² function; b) normalized conversion efficiency as a function of the position z/L inside the medium for $\Delta kL = 0, 3, 5, 10$.

matching condition depending on the characteristic of the used nonlinear medium.

The most common technique makes use of the birefringence property that many crystals exhibit. In a birefringent material, the refractive index depends on the direction of the polarization and propagation of the interacting light. Thus, waves with different polarization states travel in the medium at different speeds.

In a crystal, the refractive index is related to the symmetric tensor that describes the linear dielectric constant. By choosing a proper orthogonal coordinates system, the dielectric tensor can be diagonalized ($\varepsilon_{ij} = \varepsilon_{ii}\delta_{ij}$), so that its diagonal elements define the principal dielectric constants and the axes of the coordinates system the principal axes of the medium [83]. Similarly, the principal refractive indices are obtained through the principal dielectric constants (ε_{ij}).

The anisotropic media are generally classified on the base of their principal refractive indices. A crystal is defined *biaxial* when $n_{XX} \neq n_{YY} \neq n_{ZZ}$ or *uniaxial* when $n_{XX} = n_{YY} \neq n_{ZZ}$, which means that the medium possesses two or only one axis of symmetry, respectively.

Generally, the refractive indices of an uniaxial crystal are distinguished in *ordi-*

ordinary index ($n_o = n_{XX} = n_{YY}$) and in *extraordinary* index ($n_e = n_{ZZ}$). Therefore, its birefringence is defined as the difference between the extraordinary and ordinary refractive index: $\Delta n = n_e - n_o$. When $\Delta n > 0$ the crystal is denoted as *positive* or *negative* when $\Delta n < 0$.

The most common technique to balance the phase mismatch by exploiting the birefringence is the angle tuning. This method is based on the fact that the amount of birefringence depends on the angle of the light propagation into the medium. Therefore, the angular orientation of the crystal is carefully adjusted with respect to the propagation direction of the incident radiation to achieve the proper birefringence. For the SHG process the momentum conservation ($\Delta k = 0$) reduces to a condition imposed to the refractive indices of the fundamental and the SHG signals

$$n_{2\omega} = n_{\omega} \quad (3.2.11)$$

Based on the choice of the polarization of the fundamental wave, the condition expressed in Eq. 3.2.11 can be satisfied by using two different types of phase matching:

- type I phase matching: the polarization of the fundamental wave forms an angle θ with the symmetry axis [85]

$$n_e(\theta, \omega) = n_o(2\omega) \quad (3.2.12)$$

where [81]

$$\frac{1}{n_e^2(\theta)} = \frac{\sin^2(\theta)}{\bar{n}_e^2} + \frac{\cos^2(\theta)}{n_o^2} \quad (3.2.13)$$

with \bar{n}_e is the principal value for the extraordinary index.

- type II phase matching: the fundamental wave includes an ordinary and an extraordinary waves [85]

$$\frac{1}{2}[n_e(\theta, \omega) + n_o(\omega)] = n_o(2\omega) \quad (3.2.14)$$

However, this phase matching technique is ineffective in case of cubic crystal, because they lack the birefringence property due to their optical isotropy.

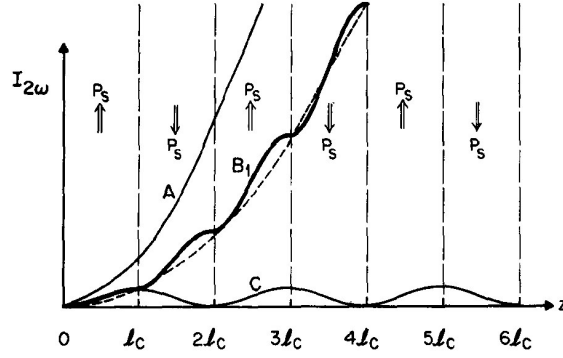


Figure 3.7: Intensity of Second Harmonic signal in condition of perfect phase matching (curve A), QPM (curve B) and unphase matching (curve C). P_s is the nonlinear polarization that is spontaneously created during the process [84].

An alternative method is the quasi phase matching (QPM) that involves a periodic modification of the property of the nonlinear medium. The modulation is fabricated such that it gives rise to a spatial variation of the nonlinear susceptibility every coherent length, i.e. at the beginning of the energy reflow from the SHG signal towards the fundamental light.

The requirement of momentum conservation ($\Delta k = 0$) is then satisfied with less restrictive condition. If the spatial modulation of the nonlinear property has a period Λ , this grating possesses a wavevector $\Delta k_G = 2\pi/\Lambda$ with $\Lambda = 2l_c$ that participates in the momentum balance

$$\Delta k - \Delta k_G = 2k_\omega - k_{2\omega} - \frac{2\pi}{\Lambda} = 0 \quad (3.2.15)$$

As a result, the SHG intensity monotonically grows as the signal propagates into the medium (curve B of Fig. 3.7).

An effective poled structure is the one that causes a reversion of the sign of the second order of the nonlinear susceptibility every coherence length ($\chi^{(2)} \rightarrow -\chi^{(2)}$). In ferroelectric materials (the most common are the lithium niobate (LiNbO_3) and the lithium tantalate (LiTaO_3)), for example, this kind of QPM is achieved by means of the electric-field poling method. In this method a static electric field is applied to metallic electrodes that are deposited on the surface of the material

with a periodic pattern [84]. Furthermore, since the QPM does not require the birefringence property, it can be applied even to isotropic materials. In case of semiconductors with a weak or null birefringence, such as gallium arsenide (GaAs), the dispersion compensation can be obtained by means of a periodical structure fabricated by growing the crystal with different crystallographic orientations [84].

3.3 Second harmonic generation from silicon surface

Due to its cubic crystalline structure, silicon belongs to the category of the centrosymmetric materials. Hence, in bulk silicon the second order dipole response ($\chi^{(2)}$) is zero and the second order nonlinear phenomena can arise only through higher order nonlinearities, like bulk electric-quadrupole or magnetic-dipole. However, the appearance of a SHG signal measured in reflection from the silicon surface indicates the presence of a violation of its symmetry [87–92]. In silicon, and more in general in every centrosymmetric crystal, the lattice symmetry is broken by the presence of the free surface, like the external surface at which the crystal terminates, or by the interface with another material, because it represents a crystal discontinuity [93, 94].

When the silicon is bonded to another material and an intense light is incident on the structure, a SHG signal is generated from a very thin layer (few tenth nanometers [94]) at the interface region (Fig. 3.8). In this process the induced surface nonlinear polarization is determined by two main sources

$$P_{NL}^s = P_{NL}^s(P_s, P_b)$$

the surface dipolar polarization (P_s) induced in the interfacial layer and the uniform bulk nonlinear polarization P_b , that is the result of the superposition of the effects of a stack of thin slabs with nonlinear polarization similar to P_s [92].

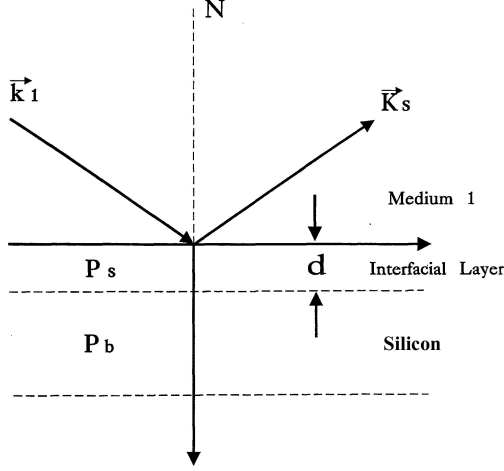


Figure 3.8: Geometry of SHG in reflection from the interface between silicon and a generic medium 1. \vec{k}_1 is the wavevector of the incident light, \vec{k}_s is the SH wavevector, d is the thickness of the interfacial layer. P_s and P_b are the surface dipolar polarization and the uniform bulk nonlinear polarization, respectively. The z -direction is parallel to surface normal and is positive in silicon. Adapted from [92].

An explicit form for P_{NL}^s is in cgs units [92]

$$P_{NL}^s(2\omega, z) = P_d(2\omega, z) + \nabla \cdot \mathbf{Q}(2\omega, z) \quad (3.3.1)$$

where z is the normal direction to the surface, ω is the frequency of the incident light, P_d is the electric-dipole polarization and \mathbf{Q} is the electric-quadrupole polarization. Expanding these two polarizations in series of the electric field and its derivative, they become [92]

$$\begin{aligned} P_d(2\omega, z) = & \chi_s^d(2\omega, z=0) : E(\omega, z=0)E(\omega, z=0)\delta(z) \\ & + \chi_d^q(2\omega, z) : E(\omega, z)\nabla E(\omega, z) \\ & + \chi_d^d(2\omega, z) : E(\omega, z)E(\omega, z) \end{aligned} \quad (3.3.2)$$

$$\mathbf{Q}(2\omega, z) = \chi_q^q(2\omega, z) : E(\omega, z)E(\omega, z) \quad (3.3.3)$$

The first term on the right side of Eq. 3.3.2 that depends on $\chi_s^d(2\omega, z=0)$ counts the contribution of the surface dipolar effect that arises from the lack of the inversion symmetry at the interface, which is treated in the limit of vanishing thickness (d

$\rightarrow 0$). The other two terms are instead bulk contributions (χ_d^q, χ_d^d). Due to the adhesion of materials with different refractive indices, a discontinuity in the normal components of the electric field occurs at the interface. As a result, the non local electric quadrupole related to the gradient of the electric field plays an active role in the surface nonlinearity and acts as an effective dipole source χ_d^q [93]. This term can be varied by controlling the electric field gradient, i.e. it is reduced (enhanced) when the difference between the refractive indices of the two materials becomes smaller (higher). The second bulk contribution, instead, has been introduced on the fact that, although silicon has an inversion symmetry, in presence of inhomogeneous strain the bulk dipole nonlinearity (χ_d^d) can be enhanced and varied. This effect will be discussed soon. The last term in Eq. 3.3.1 arises from the discontinuity that occurs at the interface also in the tensor components of the bulk quadrupolar susceptibility (χ_q^q). Therefore, this term is governed by the gradient of χ_q^q and it represents a bulk contribution. In fact, when integrated across the interface, it yields the difference of bulk susceptibilities of the two materials [93]. However, since the several contributions can not be experimentally separated, the surface second order nonlinearity is commonly described by an effective nonlinear surface tensor $\chi^{(2)} = \chi_{s,\text{eff}}^{(2)}(2\omega)$.

Thanks to the fact that the form of the $\chi_{s,\text{eff}}^{(2)}$ tensor and the values of its components reflect the surface symmetry and are strongly dependent on the materials defining the interface, the generated SHG is used as a surface-specific probing signal in nonlinear surface spectroscopy [90, 95–97].

For example, as happens in the other centrosymmetric materials, the intensity and the angular distribution of surface SHG is critically sensitive on chemical modifications occurring at the surface when the dangling-bond states are eliminated or strongly altered by chemical reactions [90, 98–101]. For example, in oxidized surface the formation of Si-O bonds increases the SHG response because of the effect of the chemical polarization induced by the polarity of the formed bonds.

Furthermore, the second order nonlinearity of the silicon surface has been found

to be greatly enhanced also in presence of inhomogeneous mechanical deformations [87–89, 91, 92, 102]. The microscopic origin of this contribution can be associated to the distortion of the Si-Si bond length and angle [92, 103]. Currently, two theoretical models having a similar approach exists to describe the relation between the strain and the second order susceptibility at the microscopic scale [87, 92]. These models are based on the bond activity model, where the nonlinear response of a unit cell is decomposed in the geometrical superposition of the contributions of each bond [92]. The bonds are assumed to be created through the sp^3 hybridization of the orbitals of the central atom with its neighbors. Therefore, only a Coulomb interaction between nearest neighbors is considered, ignoring the long-range nature of Coulomb force [87]. With this model Govorkov et al. have estimated the contribution of strain-induced $\chi^{(2)}$ to the total surface second order nonlinearity by comparing the intensity of the strain-induced SHG to that of the bulk-quadrupole contribution [87]. The model assumed a rapid decrease of the strain in the bulk with a decay length δ of about a thin film thickness [91]

$$\sigma = \sigma_0 e^{-z/\delta} \quad (3.3.4)$$

where σ_0 is the stress value at the surface and z is the distance from the surface along the normal direction. As a result, they have found that in case of small variations of the strain in the depth of the substrate the ratio between the two intensity is small, indicating an only weak contribution of $\chi^{(2)}$. Contrarily, in presence of highly inhomogeneous deformation, the $\chi^{(2)}$ contribution is enhanced causing a strong growth of the measured SHG intensity and the introduction of anisotropy in the rotational dependence of the of the SHG intensity with respect to unstrained silicon (Fig. 3.9).

The enhancement ratio has been found to be related to the strength of the stress in all the investigated samples. In case of silicon (111) strained by means of ion implantation (B^+ , P^+ and As^+), increasing the dopant concentration (which is linearly proportional to the strain), the SHG intensity has accordingly grown arriving to a maximum enhancement of about 2.5 orders of magnitude for As^+ implantation with a dose $D = 1.8 \times 10^{16} \text{ cm}^{-2}$ [87]. Furthermore, for silicon (111) strained by

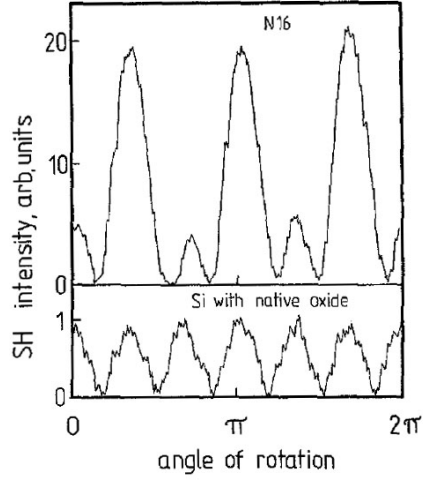


Figure 3.9: Rotational dependence of the SH intensity for a silicon (111) with 50 nm-thick SiO₂ layer that applies a strain of 0.007. The lower curve shows the rotational dependence of the SH intensity for a silicon (111) covered by native oxide [91].

a deposition of a SiO₂ layer and for silicon (001) deformed by a Si_xNi_y layer, the SHG intensity rise has been estimated by a factor 20 and 200, respectively. In this case the applied stress has been 1 GPa and 1.5 GPa for SiO₂- and Si_xNi_y-covered samples, respectively [87]. In addition, a quadratic dependence of the SHG intensity on the applied strain has been found for silicon stripes under external cylindrical strain [88]. In fact, with the sp³ orbital model the stress-induced $\chi^{(2)}$ is predicted proportional to the stress (strain) gradient

$$\chi^{(2)} \propto \nabla \cdot \sigma \sim \frac{\sigma_0}{\delta} \quad (3.3.5)$$

and thus $I_{SHG} \propto |\chi^{(2)}|^2 \propto |\sigma_0|^2$. Recently the linear relationship of Eq. 3.3.5 has been experimentally verified by measuring the SH signal reflected from a silicon (111) surface stressed by a SiO₂ layer grown by a thermal process [89].

The values reported for the stress-induced second order nonlinear susceptibility are orders of magnitude larger compared to the bulk quadrupole contribution ($\sim 5 \times 10^{-14}$ esu [87]). In fact, the $\chi^{(2)}$ has been estimated ranging between $\sim 6 \times 10^{-10}$ esu (equivalent to ~ 0.2 pm/V) for a strain of about 6×10^{-4} [88] to about $\sim 2 \times 10^{-8}$ esu (equivalent to ~ 8 pm/V) for a strain of about 1×10^{-2} [87].

3.4 Second harmonic generation in strained silicon waveguides: experimental results

The non-uniform stress distributions, that have been measured in the cross-section of the strained silicon waveguides, have revealed a significant modification of the silicon crystalline structure and thus the breaking of the centro-symmetry. As already described in Section 3.3, an inhomogeneous strain is able to induce a bulk dipole second order nonlinear susceptibility, as clearly measured through SHG experiment in reflection from a strained silicon surface. Hence, the penetration of the strain in the core of the waveguides suggests the possibility to have a non-zero dipole second order susceptibility deep in the silicon waveguide. To investigate the second order susceptibility of the strained silicon waveguides, SHG experiments in transmission have been carried out. The measurements have been accomplished in two different experiments. The first experiment aimed to study the presence of the $\chi^{(2)}$, whereas the second one to further examine the observed second order nonlinearity. In this section the experimental results of both experiments are presented and discussed.

3.4.1 Experimental set-ups

The two SHG experiments have been carried out by using two distinct set-ups. The first set-up is characterized by a ns pump laser and an InGaAs photomultiplier interfaced to a photon-counting multichannel scaler, whereas the second one by a fs pump laser and a Fourier Transform IR spectrometer. In this subsection the two set-ups are described in detail.

A. Fundamental signal at ns regime

The SHG experiments at ns regime have been carried out by using the experimental set-up illustrated in Fig. 3.10.

The laser source is an Optical Parametric Oscillator (OPO, Newport Spectra-

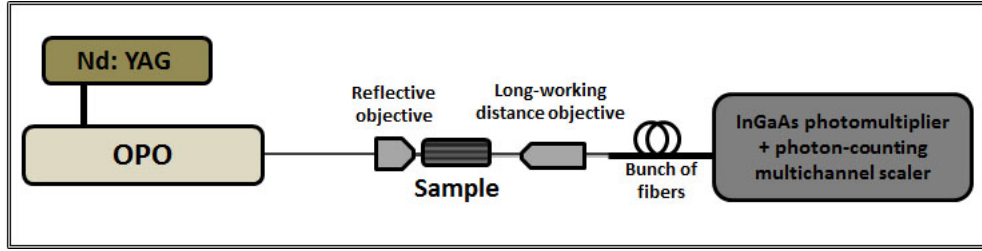


Figure 3.10: Description of the experimental set-up with the laser source at ns regime.

Physics MOPO-PO 710) pumped at 355 nm by a Nd:yttrium aluminium garnet laser. The OPO emits 4 ns-long pulses and operates at 10 Hz repetition rate. The spectral emission covers the visible window (“Signal” emission from 410 to 690 nm) and the infrared (“Idler” emission from 735 to 2400 nm).

The TE radiation has been injected into the waveguide by making use of a gold-coated 74× reflective objectives (Davin Optronics, model 5007-000) and collected with a long-working distance objective coupled to an IR camera (IR VIDICON camera, C2741-03) to visualize the guided optical mode.

The signal transmitted by the waveguide has been analysed by a fibre-coupled monochromator equipped with a liquid-nitrogen-cooled InGaAs photomultiplier (Hamamatsu) interfaced to a photon-counting multichannel scaler (model SR430 from Stanford Research Systems) triggered by the pump laser pulses. The InGaAs photomultiplier is sensitive in the 800 - 1.700 nm range.

B. Fundamental signal at fs regime

The SHG experiments at fs regime have been carried out by using the experimental set-up illustrated in Fig. 3.11.

The laser source is a $\lesssim 100$ fs laser, which is made up by a travelling-wave optical parametric amplifier (TOPAS-C from Light Conversion) pumped by a regenerative amplifier (Newport Spectra-Physics SPITFIRE) operating in pulsed mode with 35 fs-long pulses at 1 kHz repetition rate.

The source has a two beams emission between 1100-1600 nm (“Signal” spectral

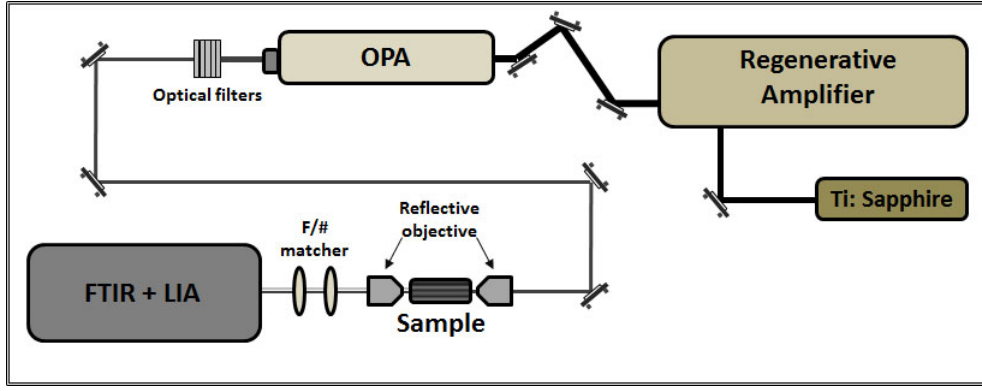


Figure 3.11: Description of the experimental set-up with the laser source at fs regime.

emission, TM polarized) and 1600-2400 nm (“Idler” spectral emission, TE polarized) and its total output average power is approximately divided in 2/3 carried by “Signal” beam and 1/3 by “Idler” beam. Despite the simultaneous emission of two beams, a one pump beam experiment can be carried out thanks to proper selectors, that limit the OPA output to a single beam.

The coupling of the input beam and the collection of the output beam into and from the waveguide have been obtained by means of two gold-coated $74\times$ reflective objectives (Davin Optronics, model 5007-000). These objectives have been chosen because they offer high magnification, longer working distance and higher damage threshold compared to the standard refractive objectives. Moreover, the design of their Schwarzschild-type optical system ensures the correction of the primary aberrations, which is a fundamental requirement when signals in a very different spectral region are involved in the experiments (more details about these objectives are given in Appendix C.2). Before starting each experiment, the two objectives have been aligned with respect the input entrance of the detection system, so that their transversal position has been maintained unaltered.

The waveguide alignment has been realized by vertically and horizontally moving the sample holder relative to the two objectives and longitudinally translating the input and the output objectives in order to find their focus points. The coupling of the fundamental beam has been controlled on line by an IR camera (IR VIDICON

camera, C2741-03), which has allowed to visualize the optical guided mode.

An optical system has been used to match the $F/\#$ of the collection objective with the $F/\#$ of the parabolic mirror at the entrance of the detector. This element is marked as $F/\#$ matcher in Fig. 3.11.

The waveguide transmission spectrum has been analyzed by a Fourier Transform Infrared (FTIR) spectrometer (model Vertex70v, Bruker), which is equipped with a 77-K-cooled InSb detector interfaced to a lock-in amplifier (LIA, Stanford Research System, SR830) in order to improve the signal/noise. The InSb detector has a wide detection spectral region, that ranges between 1000 nm to 5000 nm.

3.4.2 Second harmonic generation results: first experiment

The first SHG experiment has been performed by using the samples described in Section 1.1 (whose stress characterization results have been discussed in Chapter 2) and both experimental set-ups illustrated in Subsection 3.4.1.A and 3.4.1.B. In particular, the first set-up (Subsection 3.4.1.A) has been used for the experiments involving the 1 cm-long waveguides and the second one (Subsection 3.4.1.B) with the 2 mm-long waveguides. In both cases the input fundamental beam has been TE-polarized and no polarization control on the transmitted signals has been applied.

Despite the standard procedure in reflection to detect the SH signal generated in a thin layer of the surface of a silicon wafer, this experiment has been carried out by acquiring the transmission spectrum of the waveguide. In case of a non-zero bulk dipole second order susceptibility, a SH signal is expected to be generated and transmitted inside the waveguide.

Fig. 3.12.a shows typical transmission spectra acquired from the SOI1 (sample covered by a tensile stressing overlayer) 2 mm-long and 10.7 μm -wide waveguide in fs-pulses regime. In addition to the residual spectrum of the fundamental signal, that is centred at about 2.100 nm, a clear peak appears at short wavelengths, i.e. at 1.050 nm, the half the fundamental wavelength, as expected for a SH signal. By varying the fundamental signal, the generated peak linearly shifts according to

the theoretical relationship over 300 nm range of variation of the fundamental peak (Fig3.12.b). It is worth noting that the wavelength dependence excludes the possibility to have recorded a luminescent signal after the absorption of the fundamental wave and thus demonstrates the origin of this peak as a SHG process.

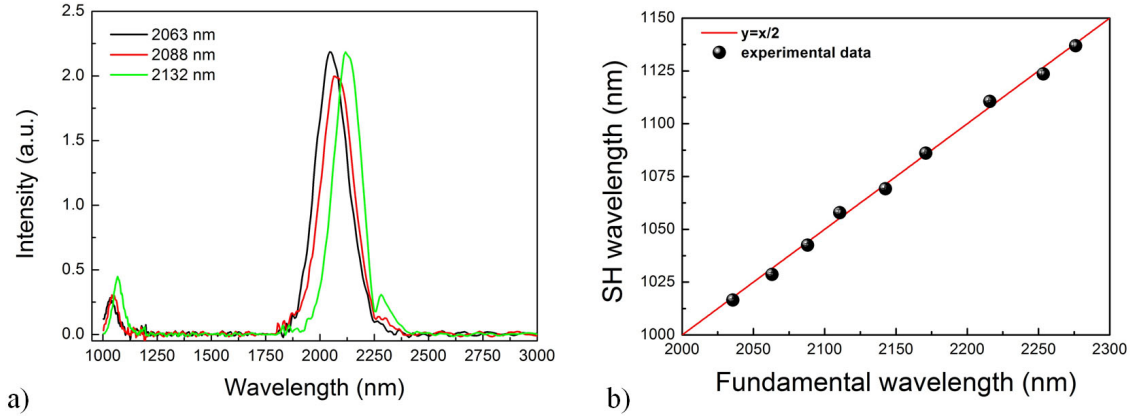


Figure 3.12: SHG measurements: a) SOI1 (sample covered by a tensile stressing overlayer) 10.4 μm -wide waveguide transmission spectra with a fs pump and peak power of 3 kW. The spectra have been corrected by the spectral response function of the detection system (Section B.2); b) Second-harmonic peak tunability curve with fs-pumping peak power 2 kW on SOI1 10.7 μm -wide waveguide. The data are measured values and the line shows the expected relationship between $\lambda_{2\omega}$ and λ_{ω} [103].

In case of fs regime, due to the sensitivity of the detection system only to the average power of the signals and the weakness of the SH signal, that does not allow to measure the temporal duration with an autocorrelator, the conversion efficiency of the process might be estimated only with the assumption of the temporal duration of the SH peak. Simulations of the group delay suggest that SH peak might be generated on the ps regime and from the analysis of the SH spectral bandwidth the SH signal results ~ 3 times narrower than the fundamental one, indicating a longer temporal duration. Nevertheless, the computation is drastically dependent on the value assumed for the SH temporal duration. For example, by converting the SH intensity from a.u. to average power Watts, the calculated peak power varies by one

order of magnitude in the range of temporal width between 1 ps and 10 ps. Hence, because of this relevant uncertainty, values of the conversion efficiency in fs-pump regime will not be reported.

Contrarily, thanks to the InGaAs photomultiplier interfaced to a photon-counting multichannel scaler used as a detector in combination with the ns pump laser, the SH peak power generated in the 1 cm-long waveguides has been directly measured [45]. Table. 3.1 reports the conversion efficiency (η) estimated for the $\sim 2 \mu\text{m}$ - and the $\sim 10 \mu\text{m}$ -wide waveguides of the various samples. The values have been computed as the ratio between the SH peak power over the fundamental peak power coupled into the waveguide, estimated on the basis of the measured coupling losses. The fundamental coupled peak power has been quantified as high as (0.7 ± 0.1) W for all the measurements.

Sample	Waveguide width (μm)	η (W/W)
SOI1	2.1	$(3 \pm 2) \times 10^{-8}$
	10.7	$(5 \pm 3) \times 10^{-8}$
SOI2	2.5	$(1 \pm 0.5) \times 10^{-8}$
	11.7	$(4 \pm 2) \times 10^{-10}$
SOI3	2.0	$(6 \pm 3) \times 10^{-9}$
	11.7	$(5 \pm 3) \times 10^{-9}$

Table 3.1: SHG conversion efficiency for the differently stressed samples at 2313 nm, where SOI1 refers to a tensile stressing overlayer, SOI2 refers to the compressive stressing overlayer and SOI3 refers to the stress-compensated overlayer.

The conversion efficiency shows a clear sample dependence. In particular, by varying the characteristic of the stressing layer, the conversion efficiency varies. Its maximum value has been found for the sample SOI1 (sample with a tensile stressing overlayer) and corresponds to few 10^{-8} W/W. Instead, the other two samples (SOI2 and SOI3, with a compressive and stress-compensated overlayer, respectively) have similar values, which are approximately one order of magnitude lower than the case

of the SOI1 sample. It is worth noting that no similar features in this pump power range have been observed on control measurements on SOI0 waveguides, where no stressing overlayer is present.

Since no specific phase matching mechanism has been designed for these waveguides, to extract the $\chi^{(2)}$ values from the measured conversion efficiencies the standard model for the unphase-matched SHG process has been applied [83]. This model predicts a spectral and longitudinal spatial periodic dependence of $\chi^{(2)}$ [83, 104]. The numerical solution of the nonlinearly coupled equations for pump and second-harmonic waves including dispersion at both harmonics [105] has shown that the 10 nm pump laser bandwidth completely masks the fast spectral oscillations, whereas the characteristic periodic oscillations of the SH intensity are still present every coherent length (analysis carried out by the Electromagnetic Fields and Photonics Group, University of Brescia). Therefore, the sample lengths have been assumed exactly equal to an odd multiple of the coherence length (which is $\sim 6 \mu\text{m}$ for the SOI1 10.7- μm -wide waveguide)

Furthermore, a rigorous procedure should consider the dependence of the efficiency on the overlap integral between the fundamental and the SH modal profiles with the $\chi^{(2)}(Y', Z')$ distribution. The $\chi^{(2)}$ is indeed expected to be nonuniform because of the inhomogeneity of the strain field in the waveguide cross-section (Y', Z'). However, an explicit theory relating the second order nonlinear susceptibility with the local strain at macroscopic scale currently lacks, therefore the action of the transverse distribution of $\chi^{(2)}$ has been assumed by means of an equivalent effective spatially averaged $\chi_{\text{eff}}^{(2)}$ coefficient.

Based on these assumptions, Eq. 3.2.10 becomes

$$\eta = \frac{8 \pi^2 (\chi_{\text{eff}}^{(2)})^2 P_\omega}{\varepsilon_0 c n_\omega^2 n_{2\omega} A \lambda_\omega^2 \Delta k^2} \frac{1}{\Delta k^2} \quad (3.4.1)$$

where P_ω is the peak power of the fundamental beam, A is the modal cross-section, which for simplicity has been taken to be equal to half the waveguide cross-section, Δk is the phase mismatch between the fundamental and the second-harmonic signal

calculated with the effective refractive indices n_ω and $n_{2\omega}$ for the fundamental guided modes at the pump and second-harmonic wavelengths, respectively.

The values calculated from Eq. 3.4.1 and listed in Table 3.2 demonstrate that a $\chi_{\text{eff}}^{(2)}$ of several tens of picometers per volt can be achieved by cladding the silicon waveguides with a silicon nitride overlayer.

Sample	Waveguide width (μm)	$\chi_{\text{eff}}^{(2)}$ (pm/V)
SOI1	2.1	20 ± 15
	10.7	40 ± 30
SOI2	2.5	11 ± 8
	11.7	4 ± 3
SOI3	2.0	9 ± 6
	11.7	14 ± 10

Table 3.2: Effective second order susceptibility $\chi_{\text{eff}}^{(2)}$ for the differently stressed samples at 2313 nm, where SOI1 refers to a tensile stressing overlayer, SOI2 refers to the compressive stressing overlayer and SOI3 refers to the stress-compensated overlayer.

Interestingly, the largest $\chi^{(2)}$ value has been estimated in the SOI1 waveguides, where the stress characterization had revealed a strong stress gradient along the height of the waveguides due to the sign inversion of the stress from the top to the bottom of the waveguide. This observation is in qualitative agreement with the results obtained with ab initio calculations, that have computed the second-order nonlinear optical response from strained bulk silicon by time-dependent density-functional (TDDF) theory in a supercell approximation with periodic boundary conditions (simulations carried out by the Nanostructures Modeling Group, University of Modena and Reggio Emilia). The results have shown that, by modifying the length and the angle of the Si-Si bond to simulate a pure tensile stress field (such as in SOI2 and SOI3 samples), the second order susceptibility ($\chi^{(2)} \sim 6$ pm/V) is more than one order of magnitude lower than the condition when both tensile and compressive stresses are applied ($\chi^{(2)} \sim 200$ pm/V), such as in SOI1.

An apparent $\chi^{(2)}$ dependence on the geometrical dimensions of the waveguides has been also observed. However, the origin of this relation is not yet clarified. A possible explanation might arise from the differences observed in the degree of inhomogeneity of the stress distribution among waveguides of the same sample but with diverse widths and in the diverse optical properties associated to the geometrical dimensions of the waveguides. In fact, the latter influences the value of the conversion efficiency, and thus of the extracted effective $\chi^{(2)}$, as well as the stress distribution by means of the overlap integral between the spatial profiles of the fundamental and SH modes and the $\chi^{(2)}$ distribution.

3.4.3 Second harmonic generation results: second experiment

The second SHG experiment has been performed by using the samples described in Section 1.2 and the experimental set-up involving the fs-pulses laser combined with the FTIR spectrometer (Section 3.4.1.B). In this experiment only the 2 mm-long waveguides have been measured with a TE-polarized input fundamental beam. Also in this case the polarizations of the transmitted signals have not been analyzed.

This experiment aimed to obtain a better comprehension of the second order nonlinear optical properties of the strained silicon waveguides. With this purpose, the role of pure interface and stress-induced contributions, originated by the presence of the cladding layer, have been investigated utilizing samples fabricated with diverse materials and different covering configurations. The nonlinear optical performances of the samples have been compared by studying the SHG conversion efficiency, defined in this experiment as

$$\eta = \frac{I_{2\omega}M}{I_{\omega}^2} \quad (3.4.2)$$

with $[\eta] = [\text{a.u.}/(\text{a.u.})^2]$ and where M is the value of the M factor introduced by the F/# matcher (see Appendix B.1) and $I_{2\omega}$ and I_{ω} are the intensities of the transmitted spectra of SH and fundamental signals, respectively. In particular, the conversion

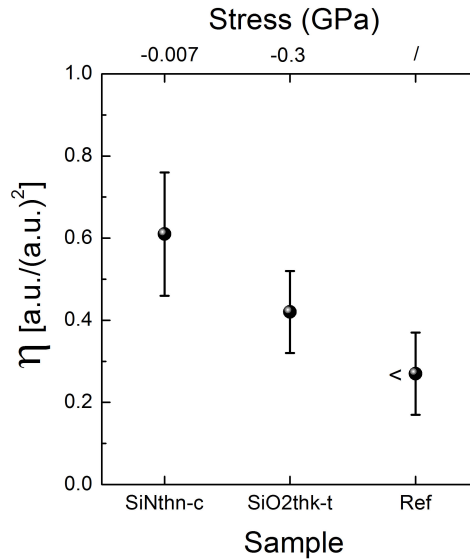


Figure 3.13: Study of stress-induced and interface effects by means of the conversion efficiency measured at 2244 nm for 10 μm -wide waveguides. *Ref* refers to the sample where the waveguide are not covered by a cladding layer; *SiO2thk-t* is the sample where a 500 nm-thick silicon oxide layer applies a stress of -300 MPa; *SiNthn-c* is the sample where the waveguides are completely covered by a 50 nm-thick silicon nitride layer with negligible stress.

efficiency values have been calculated averaging over the results obtained for five different waveguides of every sample, where for each waveguide the SH signal has been acquired at different coupled pump powers, typically in the range between tens of nano Watts up to 0.15 μW of average power.

Although widely studied in the past, the first interface investigated has been the silicon and native silicon oxide interface of the sample composed by waveguides without a cladding layer (**Ref** sample). As expected by the fact that in this sample the SHG process is dominated by surface and bulk quadrupole effects, a very weak SH signal has been measured only at high pump power. In fact, at difference the other samples, the pump power has been increased close to the power threshold for generation of spurious signals in the detection system (see Appendix B.3). On the contrary, in the sample where the silicon oxide layer has been used to deform the waveguides exerting a stress of -300 MPa (**SiO2thk-t**), the SH conversion efficiency

has appeared larger than value for the **Ref** sample (Fig. 3.13). This result confirms the significant role of the stress in influencing the second order nonlinear response of the waveguides and, thus, it can be interpreted as the evidence of a pure stress-related effect in the enhancement of the SHG process.

As the strained silicon waveguides can be also realized by utilizing the silicon nitride as basic material of stressing layer, the effect of the interface between silicon and silicon nitride has been investigated by means of waveguides completely covered by a 50 nm-thick silicon nitride layer, where the stress effect can be considered negligible (**SiNthn-c**). In fact, the overlayer stress has been quantified to be -7 MPa. Surprisingly, a conversion efficiency comparable to that one found in the SiO2thk-t sample has been measured (Fig. 3.13). The origin of such strong SH signal is not yet clear, but possible explanations may be analyzed.

Previous studies of second order nonlinearity in silicon nitride have shown that SH can be generated in silicon nitride ring resonators utilizing an effective second order susceptibility of $\chi^{(2)} \sim 0.04$ pm/V which is induced at the interface between the the silicon nitride and the silicon oxide [106]. Further, a SH signal can be generated at the interface of thin film Bragg reflectors fabricated in various compositions of amorphous silicon nitride to induce a resonant enhancement of the surface effect through microcavities [107]. In addition, resonant surface SHG effect has been reported in high-quality amorphous silicon nitride (a-Si_{1-x}N_x:H) Fabry-Pérot microcavities as well as in multi-layer silicon-oxy-nitride (SiON) waveguides [108,109]. However, although these observation might justify the SH signal measured in the SiNthn-c sample, the reported $\chi^{(2)}$ value might be not sufficient to explain the similarity with the SiO2thk-t sample.

A recent study has reported the observation of a strong SH from PECVD silicon nitride films grown on fused silicon oxide substrate. The dominant component of the $\chi^{(2)}$ tensor has been estimated to be 2.5 pm/V. It was assigned to a bulk origin has been interpreted from the SH intensity dependence on the film thickness. Nevertheless, although this value may be sufficiently high to explain the high detected SH

signal, the high contrast index of the studied waveguide causes a strong confinement of the guided mode, which excludes the possibility of a penetration of the mode inside the silicon nitride layer.

Tentatively, the second order nonlinearity observed in this sample might be related to the physical and chemical properties of the PECVD silicon nitride. In fact, a PECVD silicon nitride is characterized by a high concentration of hydrogen in the film due to the silane precursor gas. Thus, the hydrogenated silicon bond polarization, although lower than oxidized silicon bonds [90], might have influenced the second order response [93]. Moreover, contribution from a very thin layer of SiON, grown between the silicon and the silicon nitride during PECVD deposition [110], can be excluded. Careful attention has been paid during the sample fabrication to avoid such contamination. On the other hand, the nonlinearity at the interface might have been improved by structural modifications due to defects formed in the silicon nitride by the ion bombardment during the low frequency plasma deposition [87, 111, 112]. Nevertheless, a more solid interpretation of the nonlinear signal would have been obtained from the comparison with a no stressing LPCVD silicon nitride layer. Unfortunately, this sample was not available.

As a consequence of the information deduced from the SiO₂thk-t and SiNthn-c samples, the nonlinear response of silicon waveguides stressed by silicon nitride overlayers may be explained as the results of the superposition of interface and stress-related effects. In fact, by increasing the stress exerted by the silicon nitride film, the SH conversion efficiency grows independently on the sign of the stress, i.e. positive or negative, in confirmation of the results obtained in the first SHG experiment (Fig. 3.14).

Another interesting result has come from the comparison between top (**SiNthk-t**) and completely covered (**SiNthk-c**) samples. Different covering configurations should influence differently the second order nonlinearity of the waveguide due to the variations of the strain field distribution. Mechanical simulations have shown that the penetration of the stress is more effective in the SiNthk-c sample, but the

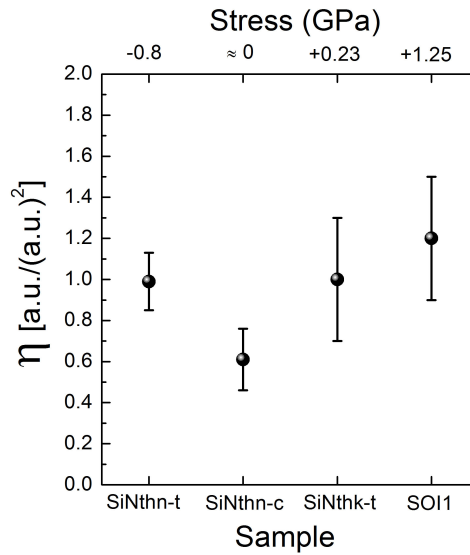


Figure 3.14: Study of the conversion efficiency enhancement due stress-induced effects. The measurements have been carried out at 2244 nm for 10 μm -wide waveguides. *SiNthn-t* refers to the sample where a 50 nm-thick silicon nitride overlayer covers the top surface of the waveguide and applies a stress of -800 MPa; *SiNthn-c* is the sample where the waveguides are completely covered by a 50 nm-thick silicon nitride layer with negligible stress; *SiNthk-t* is the sample where a 500 nm-thick silicon nitride overlayer covers the top surface of the waveguide and applies a stress of +226 MPa; *SOI1* is one of the 2 mm-long samples used in the first SHG experiment, where a 150 nm-thick silicon nitride overlayer covers the top surface of the waveguide and applies a stress of +1.25 GPa.

distribution is more inhomogeneous in the SiNthk-t sample. However, no measurable benefit in having a specific configuration has been found, although the top covering might appear slightly more efficient compared to the completely covering (Fig. 3.15). Finally, an apparent reduction of the conversion efficiency with the waveguide width has been observed in most investigated samples, similarly to what has been obtained in the first SHG experiment (Fig. 3.15).

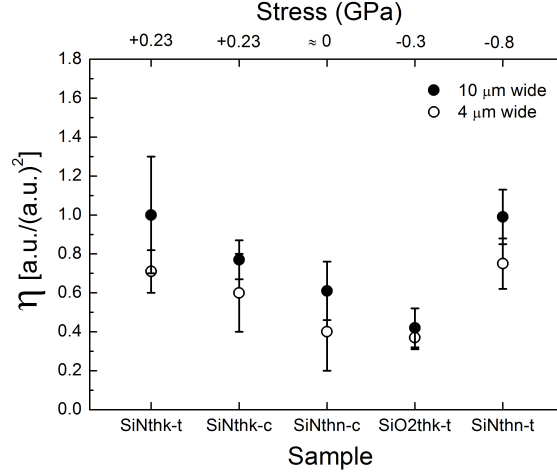


Figure 3.15: Second order nonlinearity comparison for different covering configurations and waveguide widths. The measurements have been carried out at 2244 nm for 10 μm -wide (solid circle) and 4 μm -wide (empty circle) waveguides. *SiNthk-t* and *SiNthk-c* refer to the samples where 500 nm-thick silicon nitride overlayer covers the top surface and the whole waveguide, respectively. In both cases the applied stress is +226 MPa; *SiNthn-c* is the sample where the waveguides are completely covered by a 50 nm-thick silicon nitride layer with negligible stress; *SiO2thk-t* is the sample where a 500 nm-thick silicon oxide layer applies a stress of -300 MPa; *SiNthn-t* is the sample where a 50 nm-thick silicon nitride overlayer covers the top surface of the waveguide and applies a stress of -800 MPa.

3.5 Conclusions

In this chapter the second order nonlinear optical properties of bulk silicon have been discussed. Due to symmetry reasons, silicon lacks a bulk second order susceptibility ($\chi^{(2)} = 0$), thus frequency conversion processes like SHG are governed by higher-order nonlinearities. Generally, two main contributions to the second order nonlinear optical polarization are indicated for a silicon crystal: the surface electric dipole nonlinearity, arising from the breaking of the crystal symmetry at the free surface or interface with another material, and the bulk electric quadrupole nonlinearity. Consequently, the SH process can occur only in a very thin layer at the silicon surface region. Therefore the typical method to detect the SH signal involves measurements in reflection from the silicon surface. Several studies have shown the possibility to

enhance the second order nonlinear response of the silicon surface, for example, by making using of chemical or physical modifications of the surface itself. In particular, a relatively high increase of the surface $\chi^{(2)}$ value has been found in presence of inhomogeneous mechanical stress applied by a thin film deposited on the silicon wafer. In fact, the stress-induced structural deformation of the surface yields to the breaking of the inversion symmetry and the arising of an electric dipole nonlinearity in the bulk of the surface layer.

The experimental characterization of the stress distribution carried out on the cross-section of the strained silicon waveguides have shown a penetration of the stress inside the core of the waveguide, indicating the breaking of the centrosymmetry of the silicon bulk and thus the possibility of a non zero bulk electric dipole nonlinearity.

The investigation of the second order nonlinear response of the strained silicon waveguides has been accomplished through SHG experiment in transmission configuration. Two different experiments have been carried out and various typologies of strained waveguides have been studied with a ns and a fs pump laser. The results of the first SHG experiment have shown the generation of a clear SH signal with a maximum SH conversion efficiency of the order of 10^{-8} (at ns pump regime). Under the assumption of the standard model for the unphase-matched SHG process, because no specific phase matching mechanism has been designed during the sample fabrication, a waveguide length equal to an odd multiple of the coherence length and an uniform distribution of second order susceptibility on the waveguides cross-section, an effective $\chi_{\text{eff}}^{(2)}$ value of several tens of picometers per volt has been estimated. The $\chi_{\text{eff}}^{(2)}$ has shown a strong dependence on the characteristic of the stressing silicon nitride layer. Its maximum value, corresponding to 40 pm/V, has been found for the sample SOI1, which is the sample covered by a tensile stressing overlayer. Instead, the other two samples (SOI2 and SOI3, with a compressive and stress-compensated overlayer, respectively) are characterized by lower values. This dependence is qualitatively in agreement with the results obtained by the first principle calculations of the second order nonlinear response of strained bulk silicon

by time-dependent density-functional (TDDF) theory in a supercell approximation with periodic boundary conditions [103]. The simulation have shown that the most favorable stressing condition to enhance a strong $\chi_{eff}^{(2)}$ is the simultaneous action of a tensile and a compressive stress, as in the SOI1 sample.

Although in this experiment the interface effects can not be ruled out, the observed dependence of the $\chi^{(2)}$ on the stressing layer and the high inhomogeneity of the strain measured across the core of the waveguide suggest a high enhancement of the stress-induced bulk component of the $\chi^{(2)}$ susceptibility in the core of the waveguides.

The second SHG experiment has studied the role of interface and stress-induced contributions by making use of samples fabricated with different materials and covering configurations. The comparison between the conversion efficiencies measured for standard waveguides and waveguides covered by a stressing layer of silicon oxide has confirmed the pure stress-related effect in the second order nonlinear properties of the silicon waveguides. Contrary, waveguides covered by silicon nitride layer, whose stress is negligible, have shown a non negligible contribution of the interface between silicon and silicon nitride to the SHG process. In fact, a conversion efficiency comparable to the one measured in the sample covered by the stressing silicon oxide layer has been found. The origin of such strong surface effect is not yet clear, therefore a more insight into this contribution is necessary. Nevertheless, samples covered by layers of silicon nitride that exert a stress on the underlying waveguide have shown an increase of the conversion efficiency. This indicates that in case of stressing silicon nitride layer the second order nonlinearity arises from the superposition of interface and stress-induced effects. Moreover, the comparison of different covering configurations has not shown evidence of a preferable configurations, though the stress distribution in the various cases is different. Finally, an apparent nonlinearity dependence on the geometrical dimensions of the waveguides has been observed. In fact, in both experiments the largest waveguides have been characterized by a stronger efficiency compared to the narrower ones.

Chapter 4

Second order nonlinearity: analysis and discussion

In this chapter theoretical studies of the second order nonlinear optical properties in strained waveguide are presented. These analyses do not interpret the results achieved in both SHG experiments, but provide more information for the comprehension and future studies of the second order nonlinearity in strained silicon waveguides.

They consist in exploring the possibility of an intrinsic phase-matching mechanism arising from the multimodal property of the measured waveguides and in determining how the conversion efficiency is influenced by the strain distribution.

4.1 Analysis of possible modal phase matching

As explained in Section 3.2, an efficient nonlinear interaction in a medium requires a proper phase relationship between the interacting waves along the propagation direction to balance the effect of the dispersion of the medium. In case of a broad band fundamental (FF) pulse, the phase-matching condition involves not only the control of the zero-order term of the dispersion, i.e. the phase relation between the central frequencies of the FF and the generated signals (in this thesis the SH signal),

but also the higher-orders. In fact, the mismatch between the group velocities causes the loss of temporal overlap of pulses, that severally reduces the nonlinear interaction. As a consequence, only a small portion of the spectrum of the FF pulses can satisfy the phase matching condition, causing a limitation on the bandwidth of SH spectrum. Therefore, the SH may result spectrally much narrower than the FF.

In addition to the most common birefringence and QPM methods, another technique that can be used to impose the proper phase relation between the two interacting waves in wave-guiding structures is the *modal phase matching* (MPM) [106, 113–116]. The MPM consists in matching the effective refractive indices of the FF (n_{ω}^{eff}) and SH ($n_{2\omega}^{\text{eff}}$) optical modes through the dispersion of the guided modes. In fact, the phase matching condition

$$n_{\omega,n}^{\text{eff}} = n_{2\omega,m}^{\text{eff}} \quad (4.1.1)$$

can be satisfied if the two waves propagate in suitable higher orders modes n and m , with $n < m$. Generally, the MPM is engineered such that the FF propagates in the fundamental mode (i.e. $n = 0$), whereas the SH in the higher-order mode that maximizes the overlap integral between the two modal profiles. However, this technique requires a proper design of the waveguide, which is characterized by a general small tolerance, that limits the MPM application in the development of efficient frequency conversion devices as well as the low achievable conversion efficiency determined by the overlap integral between the FF fundamental and SH higher-orders modes.

Nevertheless, this phase matching mechanism may be intrinsically present in highly multimode waveguides, even though it has not been specifically designed. In fact, thanks to possibility of the waveguide to guide more than one mode, the generated SH can naturally phase match with one of the higher-order modes. For this reason, the possibility to have “intrinsic” MPM in the waveguides used in this thesis has been examined. It is worth noting that the analysis has only the aim of a generic theoretical investigation, because no experimental evidences of MPM have been observed, as no beam profiler measurements of the SH signal have been carried

out. Moreover, clear indication of MPM can not be extracted from the spectral width of the SH, because possible temporal walk off effects in case of fs pump pulses can not be ruled out.

The MPM analysis has consisted in simulating the dispersion of the effective index of the guided modes at the FF and SH wavelength with a 2D-geometry mode solver based on the finite element method (Comsol Multiphysics) and searching for possible combinations of effective indices of FF and SH modes that satisfy the phase matching conditions of Eq. 4.1.1. The simulations have been carried out assuming negligible variations in the geometrical dimensions of the waveguides along the propagation direction and using the refractive index of silicon in unstrained conditions. Possible stress-induced change in the refractive index has been included in the tolerance parameter Δn . This parameter represents the maximum difference between the effective indices of the FF and SH wave defining the range of $n_{2\omega,m}^{\text{eff}}$ values within which Eq. 4.1.1 may be considered satisfied:

$$n_{\omega,n}^{\text{eff}} - \Delta n \leq n_{2\omega,m}^{\text{eff}} \leq n_{\omega,n}^{\text{eff}} + \Delta n \quad (4.1.2)$$

A reasonable maximum value of Δn has been chosen equal to 0.005. This value has been selected based on the consideration that a strain of about $\pm 2 \times 10^{-3}$, that corresponds to the maximum value obtained in the strain characterization measurements, induces a change of the silicon refractive index of about ± 0.004 at both FF and SH wavelengths. This value has been estimated by considering that in a cubic crystal medium, the strain-induced change in the refractive index can be expressed for a light polarized along the i -axis of the waveguide cross-section as [?]

$$n_i - n_0 = -\frac{1}{2}n_0^3 p_{ij} \epsilon_j \quad (4.1.3)$$

with $i = 1 \rightarrow xx, 2 \rightarrow yy$ and where n_0 is the refractive index in unstrained condition, p_{ij} are the elements of the photoelastic tensor ($p_{11} = -0.101$ and $p_{12} = 0.0094$) and ϵ_j is the element of the strain tensor.

The simulation results have shown that both wide (10 μm -wide) and narrow (4 μm -wide) waveguides are highly multimode and may support MPM between the FF

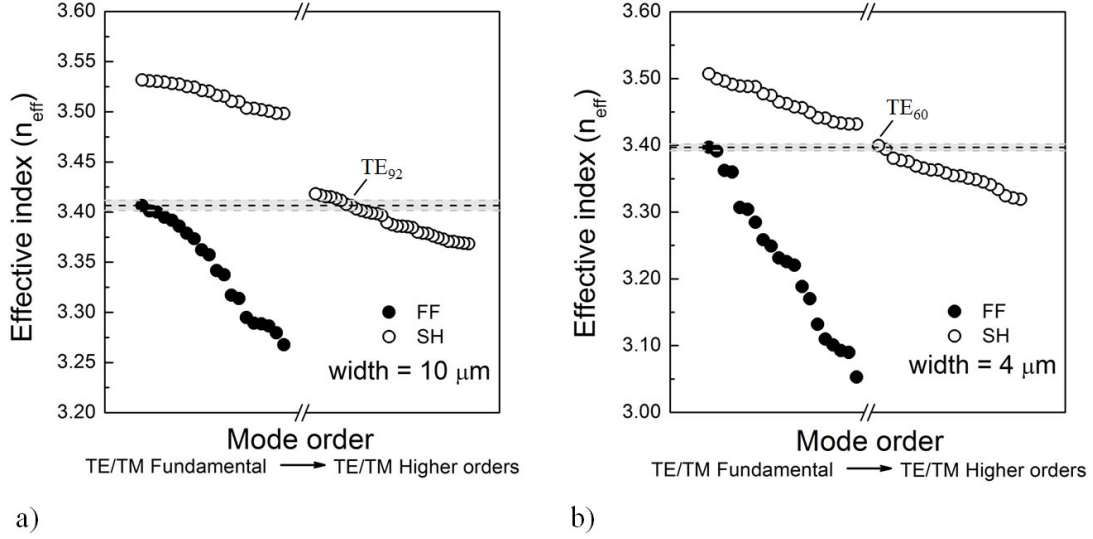


Figure 4.1: Effective indices of the FF (at 2244 nm, solid circle) and the SH (at 1120 nm, empty circle) signal as a function of the order of the TE and TM guided modes for a) 10 μm - and b) 4 μm -wide waveguide covered by 500 nm-thick silicon nitride layer. The order of the guided modes is reported such that it increases from the zero (fundamental mode) to higher values. The dashed lines are an example of possible combination of effective indices of FF and SH, where the modal phase matching may be satisfied with the lowest as possible Δn ($\Delta n = 0.001, 0.003$ for the SH mode $\text{TE}_{92}^{(SH)}$ and $\text{TE}_{60}^{(SH)}$ for the 10 μm - and 4 μm -wide waveguides, respectively). The light grey area denotes the range of values defined by Eq. 4.1.2 with $\Delta n = 0.005$.

(at 2244 nm) and SH (at 1120 nm) modes of various higher-orders, even for the TE fundamental mode ($\text{TE}_{00}^{(FF)}$) of the FF wave (note that during the SHG experiments the alignment of the waveguide has been carried out by maximizing the propagation of FF beam in the fundamental mode). Analysing in detail the modes where SH is phase matched with the $\text{TE}_{00}^{(FF)}$, the order is higher in the wider waveguide with respect to the narrower one. For example, in the 10 μm -wide waveguide the MPM is achieved between the modes $\text{TE}_{00}^{(FF)}$ and $\text{TE}_{92}^{(SH)}$, with an effective index difference of about $\Delta n \sim 0.001$ (Fig. 4.1.a), whereas in the 4 μm -wide waveguide with the $\text{TE}_{60}^{(SH)}$ mode, with a $\Delta n \sim 0.003$ (Fig. 4.1.b).

From the point of view of the waveguide nonlinear properties, the participation

of lower-order modes indicates a better overlap integral of the modal profiles in the narrower waveguide, which may determine a higher conversion efficiency, in contradiction with the experimental results achieved in the SHG experiments, where the highest conversion efficiency has been measured in the widest waveguides.

Nevertheless, by comparing the dispersion curves at the SH wavelength for the two waveguide widths, the variation of the SH effective index from one mode and the nearest neighbor is smaller in the broader waveguide, which means that within the same Δn a higher number of SH modes may be in phase matching with the $\text{TE}_{00}^{(FF)}$ mode in comparison with the narrower waveguide. As a result, the SH signal might travel in a higher number of phase matched optical modes, which constructively interfere during their propagation along the waveguide.

Moreover, due to the high number of optical modes that the waveguides can sustain, possible minor contributions to the generation of SH waves might come also from the phase matching with higher-orders modes of the FF wave. In fact, despite of the maximization of the fundamental mode and thus its dominant contribution, higher order modes excitation can not be excluded.

Although a clear understanding of the apparent dependence of conversion efficiencies on the waveguide widths observed in the SHG experiments has not yet been accomplished, the simulation results represent the first attempt to build a path to achieve a deeper knowledge on the complexity of the SHG in the measured strained silicon waveguides.

4.2 Theoretical analysis of conversion efficiency

The investigation of a possible MPM in the measured strained silicon waveguide has provided helpful information for a further analysis of the SHG process. This new analysis includes, in addition to the optical guiding properties, the characteristics of the mechanical deformation observed in the strained waveguides. As already mentioned in Section 3.4.2, the conversion efficiency is actually determined not only

by the overlap integral between the FF and the SH modal profiles but also with the $\chi^{(2)}(\mathbf{Y}, \mathbf{Z})$ distribution.

Currently, a macroscopic theoretical model able to strictly relate the $\chi^{(2)}$ with the local strain still lacks. In the nineties, when the strain-induced surface second order nonlinearity has been widely studied, theoretical models, both based on the sp^3 orbital model, have been developed to describe the $\chi^{(2)}$ and the strain relationship at microscopic scale [87, 92]. These models have been able to reproduce the results of the experiments used to verify them, but appear in disagreement with each other. In fact, the two models predict different $\chi^{(2)}$ values for similar structures stressed by approximately 1 GPa: $\chi^{(2)} \sim 0.4$ pm/V for the model proposed in [92] and $\chi^{(2)} \sim 8$ pm/V in [87]. Recently, a heuristic model based on the classical anharmonic oscillator model has been proposed in the study of a possible QPM mechanism achievable for strain-induced $\chi^{(2)}$ processes by using a periodic arrangement of stressing films deposited along a silicon waveguide [117]. Unlike the sp^3 orbital-based models, where the $\chi^{(2)}$ has been theorized proportional to the strain gradient, this model assumes a linear proportionality between the $\chi^{(2)}$ and the total strain (integrated strain gradient) and appears able to reproduce the order of magnitude of the $\chi^{(2)}$ value measured in [42]. In this model, the linearity with the total strain has been derived considering a highly uniform distribution of the strain and thus the strain gradient integration reduces to a linear integration along the center of the waveguide.

Based on these models, a theoretical study of the conversion efficiency of the various measured samples has been carried out by analyzing the overlap integral through the normalized conversion efficiency. In fact, assuming a phase-matched process, the analysis of the conversion efficiency can be reduced to the analysis of the normalized conversion efficiency (η_{norm}), which is defined as [118]

$$\eta_{norm} = \frac{8 \pi^2}{n_\omega^2 n_{2\omega} c \varepsilon_0 \lambda_\omega^2} \frac{|\iint_{Si\ core} d_{eff} E_\omega^2 E_{2\omega}^* dS|^2}{|\iint |E_\omega|^2 dS|^2 \iint |E_{(2\omega)}|^2 dS} \quad (4.2.1)$$

where $d_{eff} = d_{eff}(\mathbf{Y}, \mathbf{Z})$ is the effective nonlinear coefficient and E_ω and $E_{2\omega}$ are the

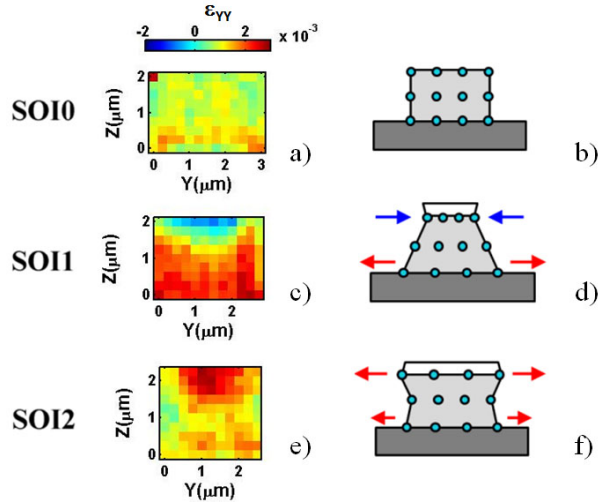


Figure 4.2: Reconstructed strain maps and lattice deformation sketches for waveguides: a, b) without cladding (SOI0), c, d) with tensile-stressing cladding (SOI1) and e, f) with compressive-stressing cladding (SOI2). The arrows show the type of observed strain.

modal profiles of fundamental and second-harmonic waves, respectively.

Considering a fundamental wave at 2313 nm and a SH at 1157 nm (like in the first SHG experiment at ns-pump regime), the normalized conversion efficiency has been estimated for the SOI1,2,0 waveguides with a 2 μm -width. This estimate is not here reported for the waveguides with a 10 μm -width due to the higher number of possible SH phase-matched modes, which complicates the analysis.

The overlap integral has been evaluated by using the strain maps reconstructed by micro-Raman spectroscopy (Fig. 4.2) and calculating the MPM conditions similarly to Section 4.1. In the analysis of the MPM, a common combination of FF and SH modes has been found, in this way only the effect of different strain distributions on the η_{norm} value could be studied. The MPM combination has consisted of the $\text{TE}_{00}^{(FF)}$ mode for the FF signal and the $\text{TE}_{22}^{(SH)}$ and $\text{TM}_{22}^{(SH)}$ for the SH modes in the SOI1,2 waveguides (Fig. 4.3.a,b,c). Unfortunately, only the $\text{TM}_{22}^{(SH)}$ mode has been found satisfying the phase matching condition for the SOI0 waveguide, while this modes combination is not present in the SOI3 sample.

Two different relationships between the d_{eff} and the strain has been assumed:

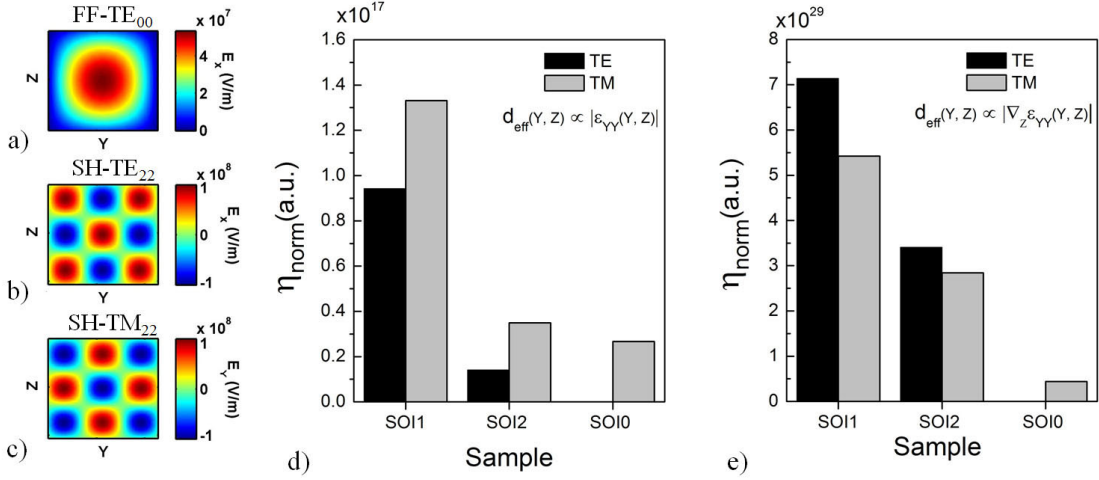


Figure 4.3: Normalized conversion efficiency study: a) modal distribution of the $\text{TE}_{00}^{(FF)}$ mode for FF wave at 2313 nm in SOI1 sample; b,c) modal distribution of the $\text{TE}_{22}^{(SH)}$ and $\text{TM}_{22}^{(SH)}$ mode for SH at 1157 nm in SOI1 sample, respectively; d) normalized conversion efficiency for SOI1,2,0 samples calculated assuming a linear relation between d_{eff} and the strain; e) normalized conversion efficiency for SOI1,2,0 samples calculated assuming a linear relation between d_{eff} and the strain gradient.

- 1) a linear relation with the strain, as hypothesized in [117]

$$d_{\text{eff}}(Y, Z) \propto |\epsilon_{YY}(Y, Z)| \quad (4.2.2)$$

- 2) a linear relation with the gradient of strain along the normal direction to the top surface of the waveguide, as hypothesized in [87, 92]

$$d_{\text{eff}}(Y, Z) \propto |\nabla_Z \epsilon_{YY}(Y, Z)| \quad (4.2.3)$$

where the absolute values of the strain and the strain gradient have been used assuming a local relation independent on the sign of the strain.

Both models shows that the highest normalized conversion efficiency is achievable in the SOI1 waveguide, independently on the polarization of the SH mode (Fig. 4.3.d,e), whereas lower values are expected in case of a mainly tensile-like strain distribution, like in SOI2 sample. Instead, the lowest normalized conversion efficiency

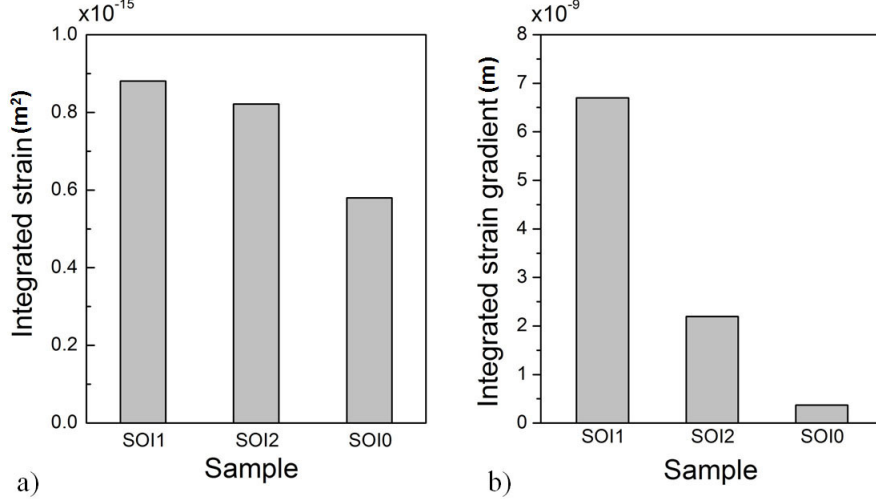


Figure 4.4: Strain analysis: a) integrated strain for the SOI1,2,0 samples; b) integrated strain gradient for the SOI1,2,0 samples.

has been predicted for the SOI0 sample, where a clearer η_{norm} decrease has been obtained for the model assuming a proportionality of d_{eff} with the strain gradient.

As the overlap integral can be considered independent on the modal distributions due to the common combination of the modal-phase-matched modes, the differences observed in the η_{norm} values can be explained arising from the diverse strain conditions of the waveguides. In fact, the analysis of mechanical properties has shown high variations of the strain among the samples in terms of distribution. To more quantitatively compare the η_{norm} values with the strain state of the various samples, partially representative parameters might be introduced to quantify the extent and the inhomogeneity of the strain. These parameters are obtained by integration of the strain and the strain gradient over the waveguide cross-section.

From the comparison of the process efficiency with the introduced mechanical parameters, the most efficient sample (SOI1) results also the most strained one, both in the extent (integrated strain) and in the inhomogeneity (integrated strain gradient) (Fig. 4.4.a,b). Interestingly, this observation appears in agreement with the results obtained in the second SHG experiment, which have shown that the

stronger the stress, the higher the conversion efficiency. This is also consistent with the hypothesis that the higher the strain inhomogeneity, the higher the second order nonlinearity, as theorized from the results of the ab initio calculations.

4.3 Conclusions

In this chapter theoretical analyses of the second order nonlinear optical properties in strained waveguide have been carried out. In particular, the possibility of an intrinsic modal-phase-matching due to the multimodal characteristic of the measured waveguides and the normalized conversion efficiency variations with the strain distribution have been investigated.

The MPM analysis results have shown the existence of possible combinations of FF and SH higher-orders modes where the phase-matching condition for a SHG process may be satisfied for both simulated waveguide widths. Particularly, it has been observed that the wider the waveguide the higher the mode of the SH waves where the phase matching can be achieved. This indicates an expected poorer overlap integral between the FF and the SH modes, which should correspond to a lower conversion efficiency, in contradiction with the results of both SHG experiments. On the other hand, thanks to the smaller variation of the effective indices with the modes order observed in the wider waveguide, a higher number of SH higher-orders modes might be in phase matching condition with a single FF mode, suggesting the possibility of the guiding of a higher number of SH modes in the broader waveguides.

In order to comprehend the effect of different strain distributions, the normalized conversion efficiency has been investigated. In fact, in phase matching conditions, the study of the conversion efficiency reduces to that one of normalized conversion efficiency and thus to the overlap integral between the FF and SH modal profiles with the $\chi^{(2)}$ distribution. Thanks to a common combinations of modes satisfying the MPM found for the SOI1,2,0 2 μ m-wide waveguides, the relation between the nonlinear properties and the strain distribution of the waveguide could be analyzed.

The normalized conversion efficiency has been calculated using the strain maps reconstructed by micro-Raman spectroscopy and assuming two possible relationships between the $\chi^{(2)}$ (or d_{eff}) and the strain, as suggested by the existing theoretical models describing the strain-induced second order nonlinearity. The analysis has shown that the highest efficiency is expected in the sample that exhibits the strongest strain and strain gradient, in general agreement with the experimental observations and the theoretical hypothesis suggested by the first principle calculations.

Although a clear complete understanding of the SHG experiments results has not yet been accomplished, these theoretical analyses have provided a small step forward in the building of a deeper knowledge on the second order nonlinearity in the strained silicon waveguides.

Conclusions

The main aims of this thesis have been the demonstration of a frequency conversion and the characterization of the mechanical properties and the strain-induced second order nonlinearity in strained silicon waveguides.

Silicon is a semiconductor crystal with inversion symmetry, thus second order bulk nonlinearity is forbidden in electric-dipole approximation and frequency conversion processes like SHG are governed by higher-order nonlinear responses (bulk electric quadrupole and magnetic-dipole). On the other hand, modifications of the silicon interface, where the crystal symmetry is naturally broken, has been demonstrated giving rise to a strong enhancement of electric-dipole nonlinearity. In particular, in presence of an inhomogeneous strain, a second order electric dipole nonlinearity appears in the bulk of the strained surface layer.

This thesis has demonstrated the existence of a strain-induced bulk second order nonlinear dipolar susceptibility in silicon waveguides strained by silicon nitride cladding layers. In fact, the experimental characterization of the stress (strain) by micro-Raman spectroscopy, carried out on the cross-section of the strained silicon waveguides, has revealed the penetration of the stress inside the core of the waveguide due to the combined actions of the cladding overlayer and the buried oxide layer. The measurements have also pointed out a highly inhomogeneous stress, whose distribution strongly varies among the various samples, depending on the extent and the sign of the stress exerted by the cladding layer. This result has been interpreted as an indication of the breaking of the centrosymmetry of the silicon bulk and, thus, the possibility of a non zero bulk electric dipole nonlinearity.

To demonstrate the second order nonlinear response of the strained silicon waveguides, SHG experiments have been accomplished in transmission configuration. These experiments have shown the generation of a clear SH signal with a maximum conversion efficiency of the order of 10^{-8} at ns pump regime (even though a phase matching mechanism has not been specifically designed for the studied process) corresponding to an effective $\chi_{\text{eff}}^{(2)}$ value of several tens of picometers per volt. The most favorable stress condition has been observed in the presence of the simultaneous action of a tensile and compressive stress, in qualitative agreement with theoretical results obtained by ab initio calculations. The observed dependence of the $\chi_{\text{eff}}^{(2)}$ on the characteristic of the stressing silicon nitride layer has been explained to be caused by the presence of a stress-induced bulk component of the $\chi^{(2)}$ in the inhomogeneously strained core of the waveguides. In fact, a pure strain-related effect has been clearly demonstrated in waveguides strained by silicon oxide layer. Instead, a further investigation of the second order nonlinear response of waveguides strained by silicon nitride overlayer has pointed out a non negligible contribution of the interface between silicon and silicon nitride to the SHG process, indicating a superposition of the interface and stress-induced nonlinearities. Interestingly, an apparent nonlinearity dependence on the geometrical dimensions of the waveguides has been also observed. Counter-intuitively, in fact, the highest nonlinear conversion efficiency has been measured in the largest waveguides.

Furthermore, although it has not been experimentally confirmed, a theoretical analysis has suggested the possibility of an intrinsic phase-matching mechanism determined by the multimodal properties of the investigated waveguides. Possible combinations of fundamental and second harmonic higher-orders modes may indeed satisfy the modal phase-matching condition for a SHG process.

Finally, theoretical investigation has been carried out to determine the influence of the strain distribution on the conversion efficiency. The analysis has shown that the largest conversion efficiency is achievable in presence of a strong strain and strain gradient, in general agreement with the experimental observations and the

theoretical results obtained by the first principle calculations.

In general, the results discussed in this thesis have been represented the first attempt for the achievement of an understanding of the second order nonlinearity in strained silicon waveguides. However, more theoretical and experimental investigations are still necessary. For example, the future efforts should be spent in the development of a suitable theoretical model able to macroscopically provide the relationship between the $\chi^{(2)}$ and the strain. More experiments should be performed to better comprehend the influence of the waveguide geometrical dimensions and the origin of the high nonlinearity at the silicon and silicon nitride interface, as the silicon nitride represents the most effective material for the stressing layer thanks to its high stress-engineering flexibility. Moreover, experimental demonstration of quasi phase matching by making use of a stressing-periodical-poling would be highly desirable for the power boosting of $\chi^{(2)}$ generated signals.

The precise control of the second order nonlinear response of strained silicon waveguide would enable the fabrication of a new class of nonlinear devices for broadband wavelength conversion and indicate silicon as a competitive nonlinear optical materials.

Appendix A

Experimental characterization of the laser source

The characterization of the laser source has been accomplished to determine the principal parameters of the emitted pulsed beams: the beam waist radius and the temporal width of the pulses.

The waist radius has been derived from the measurements of the beam divergence carried out with two methods. By using the 86% and 99% criterions the beam divergence has been estimated by measuring the radius of a pinhole in several positions along the optical path of the laser beam.

The pulse duration of the “Signal” beam emitted by the OPA has been estimated from the autocorrelation signal obtained with an autocorrelator working in the spectral range between 1100 nm and 1600 nm. Moreover, the temporal width of the pulses belonging to the “Idler” beam emitted by the OPA with wavelengths longer than 1600 nm has been estimated by means of the temporal-bandwidth product of the beam.

A.1 Beam waist and divergence

The emission of the fs laser source used in this thesis is characterized by two optical beams with gaussian spatial profile. Therefore, their normalized field pattern is defined as [120]

$$u(x, y, z) = \sqrt{\frac{2}{\pi}} \frac{\exp[-jkz + j\psi(z)]}{w(z)} \exp\left[-\frac{x^2 + y^2}{w(z)^2} - jk\frac{x^2 + y^2}{2R(z)}\right] \quad (\text{A.1.1})$$

where z is the spatial coordinate along the propagation axis, k is the wavevector of the radiation in the medium in which the beam is propagating, while $w(z)$, $R(z)$ and $\psi(z)$ are the radius, the radius of curvature and the phase of the beam, respectively (Fig. A.1.a). These parameters can be expressed in terms of only two fundamental parameters, the waist radius and the radiation wavelength:

$$w(z) = w_0 \sqrt{1 + \left(\frac{z}{z_R}\right)^2} \quad (\text{A.1.2})$$

$$R(z) = z + \frac{z_R^2}{z} \quad (\text{A.1.3})$$

$$\psi(z) = \tan^{-1}\left(\frac{z_R}{z}\right) \quad (\text{A.1.4})$$

where w_0 is the waist radius, i.e. the minimum value of beam radius at $z = 0$, and z_R is the Raleigh distance, which is the distance at which the beam radius $w(z)$ enlarges to $\sqrt{2}w_0$:

$$z_R = \frac{\pi w_0^2}{\lambda} \quad (\text{A.1.5})$$

where λ is the wavelength of radiation.

As a result, the beam parameters vary during the beam propagation along z . The radius of curvature is infinite at $z = 0$, decreases to a minimum value at $z = z_R$ and then rises again toward infinity as z is further increased. Instead, the beam radius $w(z)$ asymptotically increases with z , causing an enlargement of the transverse irradiance profile of beam (Fig. A.2.b) that is defined as [120]

$$I(r, z) = \frac{2P}{\pi w(z)^2} e^{-\frac{2r^2}{w(z)^2}} \quad (\text{A.1.6})$$

where P is the total power in the optical beam.

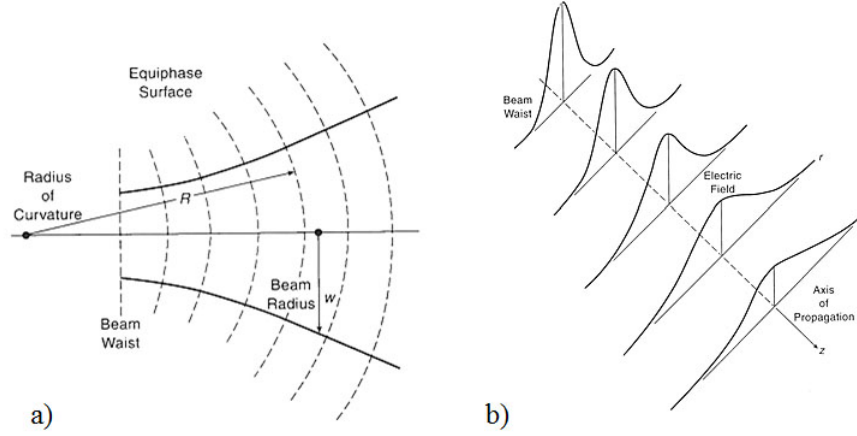


Figure A.1: Gaussian beam description: a) definition of the beam parameters: beam radius, beam waist, which is the position at which the beam radius is at its minimum, and radius of curvature ; b) enlargement of transverse irradiance profile of beam due to the growth of the beam radius during propagation along the z direction [119].

The parameter that quantifies how fast the beam radius expands far from the waist radius is the beam divergence (θ in radians):

$$\theta = \frac{w(z)}{z} = \frac{\lambda}{\pi w_0} \quad (\text{A.1.7})$$

It is worth noting that this equation is valid only for a high quality beam, i.e. for beam with the minimum possible divergence dictated by its wavelength (diffraction-limited beam). In case of inferior quality beams, the minimum divergence θ is multiplied by the M^2 factor, which is the parameter that quantifies the quality of the beam.

For the laser source used in this thesis, the quality factor is defined as the product of the M^2 values of the OPA source and its pump, $M^2 = M^2(\text{TOPAS}) \times M^2(\text{Spitfire})$, where $M^2(\text{TOPAS}) = 1.3$ [121], $M^2(\text{Spitfire}) < 1.3$ [122] and thus, $1.3 \leq M^2 < 1.69$. The beam divergence is then expected in the interval $0.17 \text{ mrad} \leq \theta \leq 0.35 \text{ mrad}$ for a beam waist radius ranging between 0.2 cm and 0.3 cm, as shown in Fig. A.2.a.

The estimation of the waist radius and the divergence of the laser source has been carried by using two methods. Based on the linear relation between the beam radius and the distance z (Eq. A.1.7), the two methods consist of measuring the

beam radius at different positions along the optical path by means of the 86% and 99% criterions relative to the aperture size of a pin-hole. When a circular aperture with radius r is placed along the beam optical path and centered with respect to the beam spot size w , the fraction of the beam power (T) passing through the aperture can be written as [120]

$$T = 1 - e^{-\frac{2r^2}{w(z)^2}} \quad (\text{A.1.8})$$

Therefore, the 86% power transmission corresponds to an aperture with radius $r = w$ (method 1), while $T = 99\%$ (method 2) to an aperture with radius $r = (\pi/2)w$.

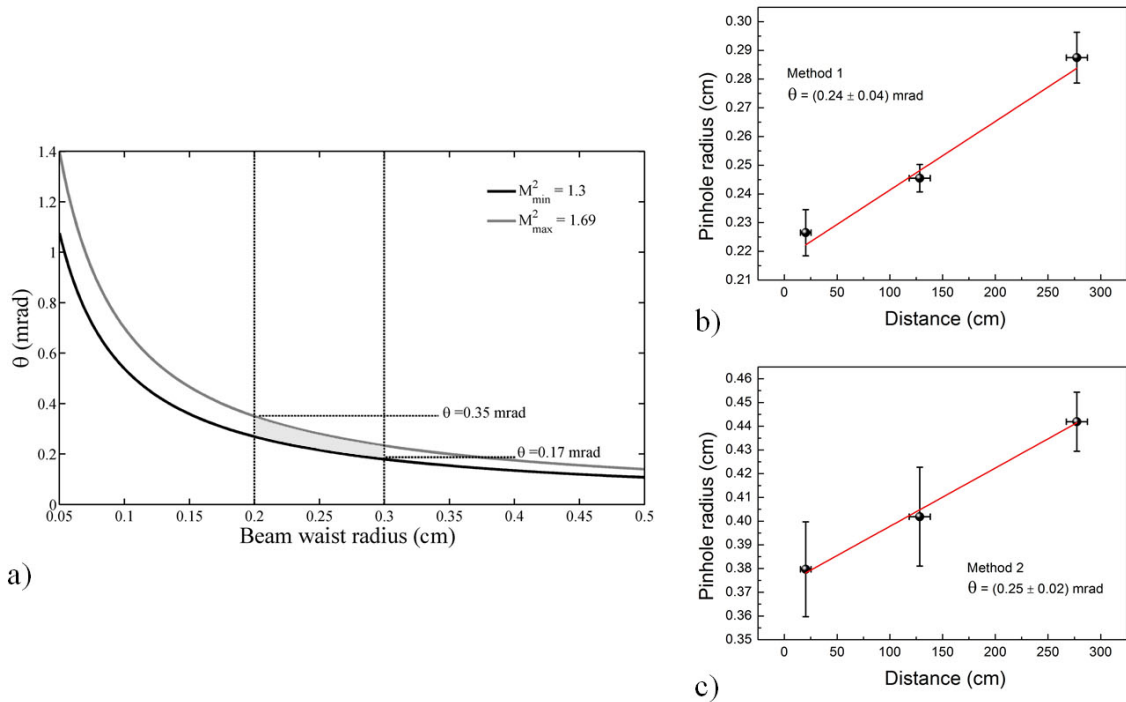


Figure A.2: Beam divergence: a) range of theoretical beam divergence expected for a laser source at 1300 nm with a quality factor $1.3 \leq M^2 \leq 1.69$. The vertical dot lines enclose the range of expected value of the beam divergence (light grey area) for a beam waist ranging between 0.2 and 0.3 cm; b-c) experimental values of pinhole radius measured at several distances from the laser output by using b) the 86% criterion (method1) and c) the 99% criterion (method 2) at 1300 nm of beam wavelength. The beam divergence is the slope of the linear fit (red lines) of the experimental data (dots).

The two methods have given beam divergence values that result in good agree-

ment. By using a beam wavelength of 1300 nm, the beam divergence has been quantified as $\theta_1 = (0.24 \pm 0.04)$ mrad with method 1 (Fig. A.2.b.) and $\theta_2 = (0.25 \pm 0.02)$ mrad with method 2 (Fig. A.2.c). Moreover, since θ is dependent on the beam waist radius according to Eq. A.1.7, the beam waist radius has been estimated from the measured beam divergence values. A waist radius of about 0.25 cm has been derived as the mean value of the set of the possible radii relative to the possible values of M^2 .

A.2 Pulse duration

The temporal duration of the pulses emitted by a 40 fs-pumped OPA has been measured by using an autocorrelator (Newport PulseScout). The autocorrelator has been equipped with an IR detector module with operation spectral range between 1000 nm and 1600 nm. Thus, the pulse duration of OPA’s “Signal” beam (nominal emission range between 1100 nm and 1550 nm) has been measured.

The measurements have been carried out by coupling the “Signal” beam with a quasi-perpendicular incident angle into the optical assembly operating in collinear conditions. In order to satisfy the phasematching condition of the nonlinear crystal, the rotation of the beam polarization from vertical to horizontal has been necessary and it has been achieved through two mirrors mounted 45° to the beam. Afterward, the beam has been aligned by matching the visible beam back reflection with the cross wires at the control window. Once the autocorrelation trace has been clearly observed, it has been maximized by rotating the nonlinear crystal to find the optimal angle. Finally, the noncollinear configuration has been selected to measure the full-width-at-half-maximum (FWHM) of the autocorrelation signal, as shown in Fig. A.3.

The temporal width of the pulses has been derived by correcting the FWHM of the autocorrelation signal with 0.7 deconvolution factor due to the assumption of a pulse gaussian shape. As shown in Table A.1, the pulses of the OPA’s “Signal”

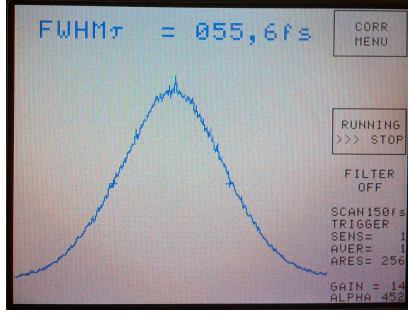


Figure A.3: Example of the envelope of the autocorrelation signal measured at 1400 nm. The 56 fs-FWHM corresponds to about 40 fs of the pulse duration.

beam have temporal width shorter than 100 fs. These short temporal widths match reasonably well with the expected values calculated from the FWHM of the spectra measured by the FTIR considering a temporal-bandwidth product (TBWP) 1.2 ÷ 1.5 times the TBWP of a bandwidth-limited pulses [121].

Beam wavelength	Pulse duration Autocorrelator	Pulse duration TBWP
1200 nm	~ 70 fs	~ 55 ÷ 65 fs
1280 nm	~ 55 fs	~ 60 ÷ 75 fs
1370 nm	~ 40 fs	~ 50 ÷ 65 fs
2000 nm	-	~ 55 ÷ 70 fs
2130 nm	-	~ 50 ÷ 65 fs
2240 nm	-	~ 35 ÷ 45 fs
2330 nm	-	~ 40 ÷ 50 fs

Table A.1: Pulse duration for several beam wavelengths measured with an autocorrelator and estimated assuming a TBWP equal to 1.2 ÷ 1.5 times the TBWP of a bandwidth-limited gaussian pulses.

Although a direct measure of pulse temporal duration of the OPA’s “Idler” beam (nominal emission range between 1600 nm and 2600 nm) has not been possible as a detector module operating in this spectral range is not available for the used

autocorrelator, an estimation can be derived from the spectral width on the basis of the results obtained for the “Signal” beam. From the calculated values listed in Table A.1 the “Idler” beam is expected to have pulse duration approximatively similar to the “Signal” beam.

Hence, the nonlinear optics experiments have been accomplished with input beams in $\lesssim 100$ fs-regime.

Appendix B

Experimental characterization of the detection system

When a nonlinear optics experiment is performed, an important role in the experimental set-up is played by the detection system. Therefore, a characterization of its principal elements have been performed. Particularly, the effect of the optical system that matches the $F/\#$ of the collection objective and the optical element at the entrance of the FTIR have been studied. Moreover, due to the broad spectral range covered by the InSb detector and the high powers that may be involved in the experiments, the calibration of the spectral response by means of a conventional procedure and the investigation of undesired spurious nonlinear signals generated by the system have been accomplished. Finally, for a quantitative estimation of the measured average power, the system has been calibrated in order to convert the a.u. of the spectra into average power units.

B.1 $F/\#$ matcher

As described in Section 3.4.1, an optical system has been used to match the $F/\#$ of the collection objective with the $F/\#$ of the parabolic mirror at the entrance of the FTIR. Since this optical system is removed during the sample alignment

procedure and put back for detecting the sample transmission spectrum, its effect on the spectrum intensity has been investigated.

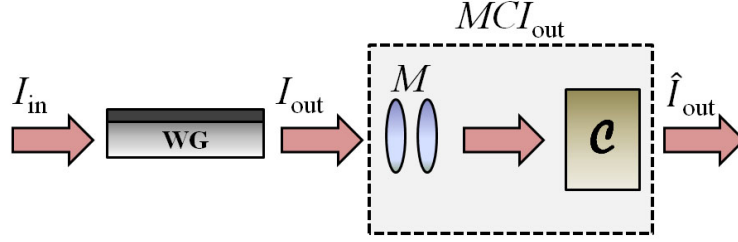


Figure B.1: Sketch of waveguide transmitted signal (I_{out}) measurement.

By modeling the detection system used in this thesis through a M factor, that describes the $F/\#$ matcher effect, and a function C related to the response of the FTIR interfaced with the LIA (Fig. B.1), the transmitted signal from a waveguide (I_{out}) may be described as a detected intensity \hat{I}_{out} such that

$$\hat{I}_{out} = MCI_{out} \quad (\text{B.1.1})$$

where \hat{I}_{out} is the measured intensity by the FTIR.

For every nonlinear optics measurements, the C is constant (see Section B.2), while the M factor value depends on the alignment. For this reason, M factor has been estimated by using the “check signal” function of the FTIR in Rapid Scan mode¹, as it allows an online fast measure of the intensity of the detected signal. In this way, the M factor has been calculated as the ratio between the intensities measured when the $F/\#$ matcher is aligned and when the $F/\#$ matcher is not included in the detection system.

The accuracy of this method has been verified by measuring the signal spectrum in Step Scan mode² interfaced with the LIA and evaluating the M factor as ratio of

¹The Rapid Scan mode is the data collection of a continuous-scan interferometry. The spectrum is calculated from the interferogram achieved by translating the moving mirror within the interferometer at constant velocity to modulate the infrared radiation.

²In Step Scan mode the interferometer’s moving mirror is translated stepwise to fixed positions, where the light intensity is recorded at equispaced time intervals Δt_j . A series of interferograms is then reconstructed from the two dimensional matrix of the recorded intensities ($I_{ij}(x_i, \Delta t_j)$, where x_i is the i -position of the mirror and Δt_j is the j -time interval) and successively Fourier-transformed.

the intensities of the peak spectra measured with and without the $F/\#$ matcher. As shown in Table B.1, the M values estimated with the Rapid Scan mode agrees with the M values extracted from the spectra measured in the Step Scan mode interfaced with the LIA.

Coupled average power	Rapid Scan M	Step Scan M
30 nW	2.4 ± 0.7	2.4 ± 0.5
40 nW	2.0 ± 0.6	1.8 ± 0.4

Table B.1: Comparison between M values estimated by using the Rapid Scan and Step Scan modes at 2130 nm for two different coupled average powers.

The linear relation of Eq. B.1.1 has been then verified by measuring the spectrum intensity \hat{I}_{out} for several alignments of the $F/\#$ matcher that have been obtained by rotating the optical system from the position of the maximum alignment (Fig B.2.a).

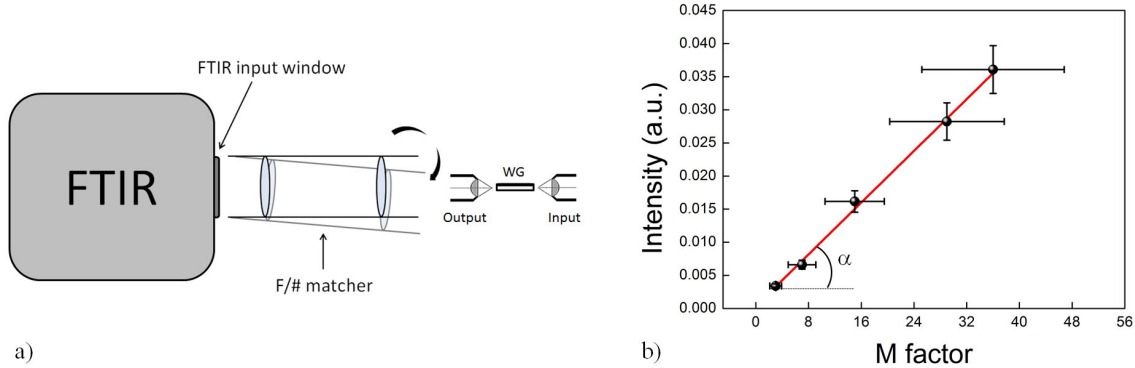


Figure B.2: Study of variation of $F/\#$ matcher M factor: a) Set-up sketch for the M factor variation; b) measured intensity \hat{I}_{out} versus M factor for coupled average power of 40 nW in a 2 mm-long waveguide at 2130 nm. The dot circles are the experimental data and the red line is the linear fit of the data with slope α .

As shown in Fig. B.2.b, the spectrum intensity \hat{I}_{out} linearly scales with the M factor value, demonstrating the linearity of the system with respect to the geometrical alignment of the $F/\#$ matcher. Therefore, according to Eq. B.1.1, the

corresponding slope α represents a direct measure of the transmitted signal I_{out} and in fact it linearly varies with the coupled average power (Fig. B.3.a).

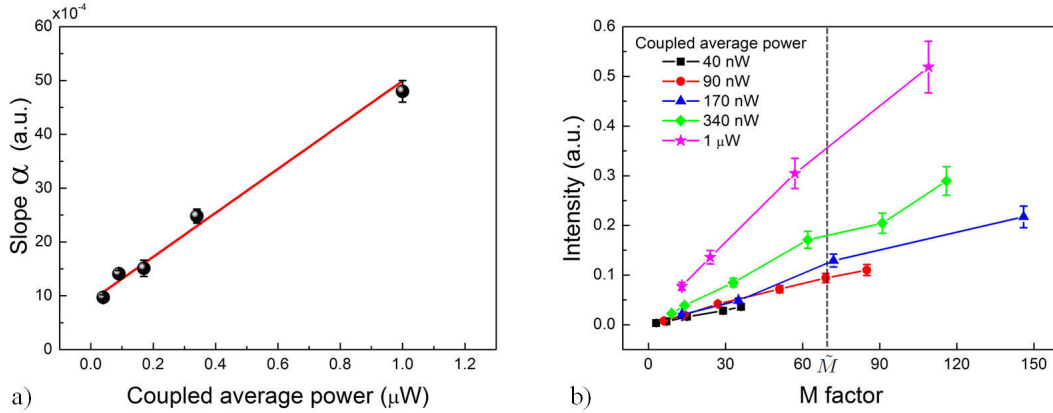


Figure B.3: Study of the slope α : a) linear dependence of the slope α on the coupled average power at 2130 nm; b) Variation of M value for different coupled average power at 2130 nm. The vertical dotted line indicates the intensity \hat{I}_{out} corresponding to a certain \tilde{M} value for different coupled powers.

As a consequence of the linear relations found between the measured intensity \hat{I}_{out} and the M factor, the acquisition of transmission spectra, and thus the detection of the transmitted signal I_{out} , can be performed just knowing only one value of M factor measured at the beginning of every experiment. In fact, if $M = \tilde{M}$ is measured for a certain alignment of the F# matcher and at a given coupled average power, all the subsequent intensities measured at different powers will be automatically scaled (Fig. B.3.b). Naturally, based on these results, if a comparison of data acquired in distinct sets of measurements, that implies diverse F# matcher alignment, have to be performed, the spectra must be scaled with respect to the corresponding M factor value.

B.2 Spectral response

The calibration of the spectral response of a detection system might be carried out by mathematically modeling the optical spectrum provided by the detection

system. The model has to take into account the influence of all the possible optical and electronic components of the system. Thus, its equations may contain many parameters that cannot be calculated only theoretically. A more efficient method for calibrating the spectral response consists of the combination of a mathematical model and the detection of the radiation emitted by a calibrated source, such as a black-body (BB) radiator.

The electromagnetic radiation emitted by a BB radiator in thermal equilibrium at a definite temperature T is described by the Planck's law as

$$L(\nu, T) = 2hc^2\nu \frac{1}{e^{\frac{hc\nu}{kT}} - 1} \quad (\text{B.2.1})$$

where $L(\nu, T)$ is the spectral radiance in $\text{W cm}^{-2} \text{sr}^{-1} \text{cm}^{-1}$, h is Planck's constant, c is velocity of light in vacuum, ν is wavenumber, k is Boltzmann constant and T is temperature. When the BB emission is detected, the measured radiance spectrum ($S(\nu)$) can be mathematically described by the following equation [123]

$$S(\nu) = R(\nu)[L(\nu) + G(\nu)] \quad (\text{B.2.2})$$

where $R(\nu)$ is the spectral response of the detection system, $L(\nu)$ is the spectral radiance of the signal that has to be analyzed, which in this case is the BB spectral radiance, and $G(\nu)$ is the spectral radiance of the background, which considers the contribution of the system components and the surrounding environment [123–125]. An example of how the detection system used in this thesis measures the BB radiator $L(\nu)$ is shown in Fig. B.4.a.

A conventional calibration procedure to determine the unknown instrumental functions $R(\nu)$ and $G(\nu)$ consists in measuring two spectral radiances $S_1(\nu)$ and $S_2(\nu)$ at two different temperatures T_1 and T_2 of the BB radiator. Thus, $R(\nu)$ and $G(\nu)$ are calculated as

$$R(\nu) = \frac{S_1(\nu) - S_2(\nu)}{L(\nu, T_1) - L(\nu, T_2)} \quad (\text{B.2.3})$$

$$G(\nu) = \frac{S_1(\nu)}{R(\nu)} - L(\nu, T_1) \quad (\text{B.2.4})$$

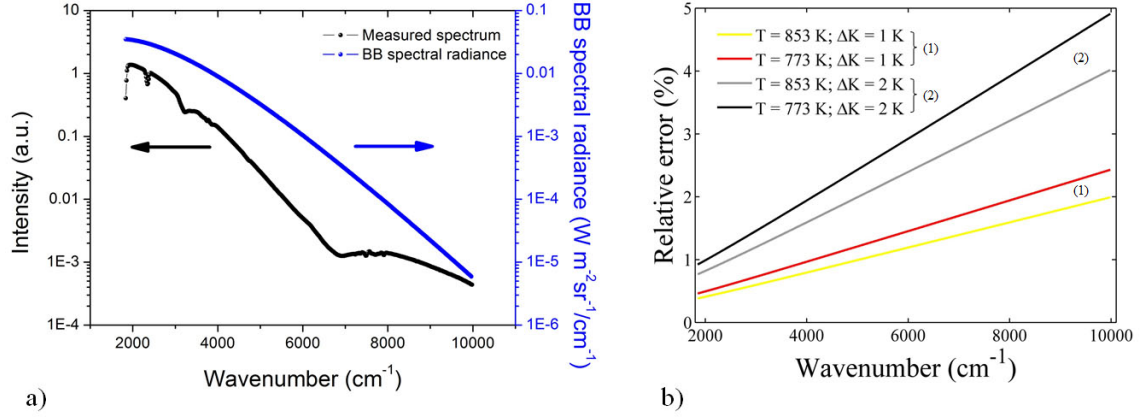


Figure B.4: BB radiator spectral radiance: a) comparison between the theoretical spectral radiance emitted by a BB source at $T = 853$ K (blue line) and the corresponding spectral radiance measured by the detection system used in this thesis (black line); b) relative error $[(L(T+\Delta T)-L(T))/L(T)]$ in the BB spectral radiance caused by the uncertainty in BB radiator temperature for (1) $\Delta T = 1$ K, at $T = 853$ K (yellow line), 773 K (red line) and (2) for $\Delta T = 2$ K at $T = 853$ K (grey line), 773 K (black line).

The accuracy in the estimation of $R(\nu)$ and $G(\nu)$ with this procedure is mainly determined by the temperature uncertainty (ΔT) in $L(\nu)$ and by the alignment of BB radiator with respect to the detection system.

The experimental error in the measurement of the BB radiator temperature (ΔT) causes an uncertainty in the estimation of spectral radiance $L(\nu, T)$. The error grows with the decreasing of the temperature of the BB radiator and the increasing of ΔT , reaching the maximum for the spectral region of the longest wavenumbers, as shown in Fig. B.4.b. As a result, deviations of few percents in the numerical values of the $L(\nu, T)$ may be reached. For example, in case of $T = 773$ K and $\Delta T = 2$ K, the deviation can be up to 5% in the spectral region of the longest wavenumbers.

Although the so called “three black-body sources” method may be applied to minimize the error caused by the limited accuracy of the temperature measurement [123], possible misalignments of the calibrated source with respect to the detection system result in an additional source of high experimental errors in the derivation of the instrumental functions. In fact, the instrumental functions are

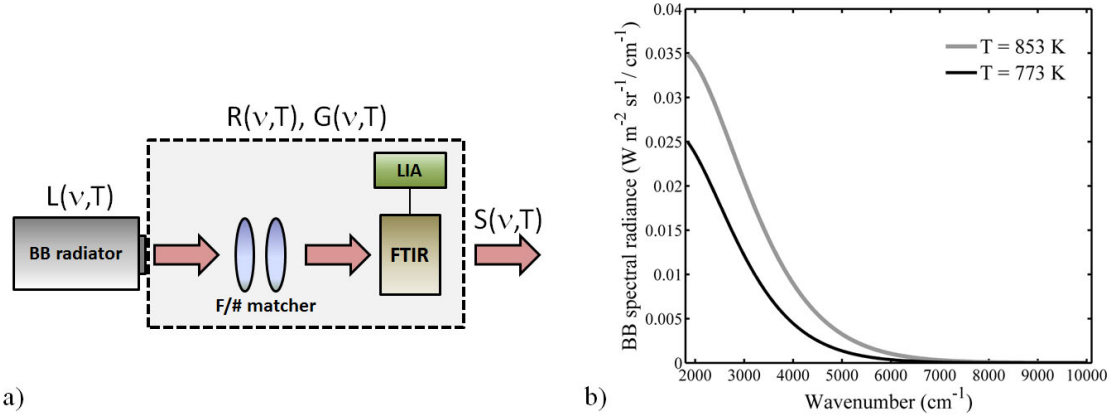


Figure B.5: a) Sketch of the mathematical model for the derivation of the instrumental function $R(\nu, T)$ and $G(\nu, T)$. All the elements composing the detection system have been considered as inner parts of a single instrument; b) BB spectral radiance at $T = 853$ K (grey line) and $T = 773$ K (black line) used for the derivation of the spectral response $R(\nu, T)$.

strongly dependent on the distance and the transversal position of the BB radiator relative to the input aperture of the detection system. The relative difference in $R(\nu)$ extracted from two different alignments (an accurate alignment and a misaligned condition) has been quantified as high as 40% for the detection system here calibrated. Consequently, the spectral response must be calibrated reproducing the same experimental conditions where the detection system is typically involved.

As described in Section 3.4.1, the detection system used in this thesis is composed by a) the FTIR and its inner optics components, b) the optical system to match the $F/\#$ of the collection objective with the $F/\#$ of FTIR entrance, c) the LIA and d) the position where generally the collection objective is placed during the nonlinear optics experiments. Thus, the calibration of the spectral response has been performed assuming all the previous parts as a single instrument (Fig. B.5.a).

The $R(\nu)$ calibration has been performed by using a BB radiator set at $T = 853$ K and $T = 773$ K, whose spectral radiances are shown in Fig. B.5.b. The BB radiator has been chopped at two different frequencies (123 Hz and 223 Hz) in order to take into account the contribution of the LIA in the detection system. As shown in Fig. B.6.a, the measured spectra $S(\nu)$ for both chopper frequencies

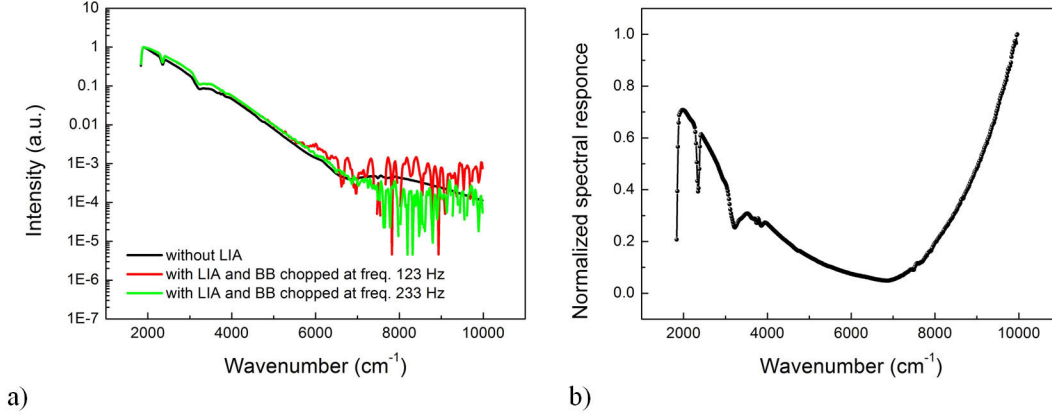


Figure B.6: a) Radiance spectrum $S(\nu, T)$ measured without LIA (black line) and with LIA for BB radiator chopped at 123 Hz (red line) and 223 Hz (green line) at $T = 853$ K; b) detection system spectral response $R(\nu)$ estimated by conventional calibration procedure.

have been affected by strong intensity fluctuations at high wavenumbers ($\nu > 6000$ cm^{-1}) that limit the accuracy of the $R(\nu)$ estimation. Contrarily, measurements carried out detecting the BB emission without the LIA have shown an acceptable signal/noise ratio in the spectral region of high wavenumbers, while maintaining a good agreement with the spectra measured with LIA for wavenumbers less than 6000 cm^{-1} . Therefore, the derivation of $R(\nu)$ function by means of Eq. B.2.3 has been carried out excluding the LIA in the detection system.

The obtained spectral response $R(\nu)$ is characterized by a concave shape and deep peaks of sensitivity reduction at about 2330 cm^{-1} and 3200 cm^{-1} (Fig. B.6.b). It is worth remarking that the calibration has not been performed in an IR inactive atmosphere, as the nonlinear optics experiments have not been carried out in purged environment with pure N_2 . Consequently, the BB emission has passed through air for 30 cm, from the BB radiator to the input of the FTIR, and in the optical path inside the FTIR. Therefore, the decrease in the sensitivity at 2330 cm^{-1} and 3200 cm^{-1} may be attributed to the strong absorption of CO_2 and OH, respectively. However, further contributions from the materials constituting the optical elements of the detection system may be also present.

B.3 Spurious signals

When very powerful beams are used in a nonlinear optics experiment, particular attention must be paid to study a possible undesired generation of spurious signals, for example due to the interaction of the pump beams with the detection system. Therefore, in order to check the presence of such unwanted signals and, if it is necessary, determine the condition where these signals are generated, a full characterization experiment has been performed.

The controlling measurement has been carried out by aligning the two objectives without the sample (configuration “1” in Fig. B.7.a) and detecting the transmitted beam for several average output powers (P_{out}^{obj})

$$P_{out}^{obj} = P_{in} T_{obj}^2 \quad (\text{B.3.1})$$

where P_{in} is the average power emitted by the OPA and attenuated by neutral reflective filters and T_{obj} is the measured transmittance of the reflective objectives (see Section C.2).

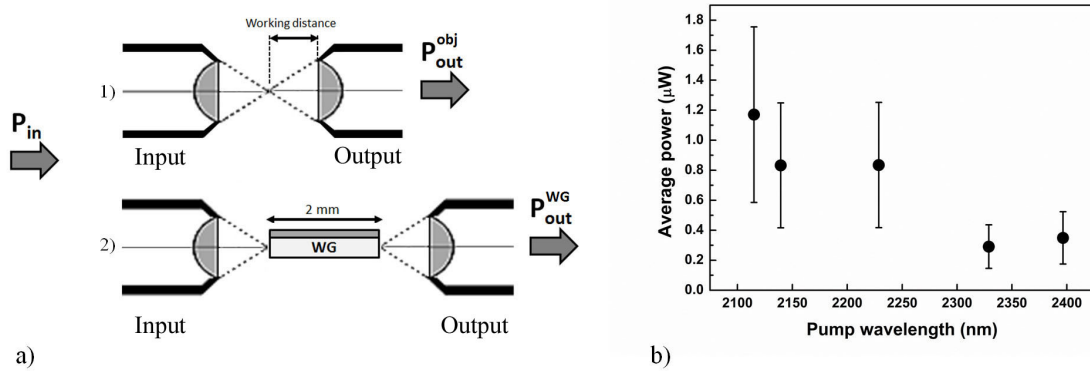


Figure B.7: Spurious signals characterization: a) controlling configurations where two reflective objectives coupled without (1) and with (2) the sample; b) SHG threshold for undesired generation of spurious signal measured for several pump wavelength.

For P_{out}^{obj} sufficiently high, a spurious signal has appeared at the spectral region of SH signal in the transmission spectrum. Since this is an undesired signal that contaminates the experimental results, the average power threshold over which this

signal is generated has been estimated. By varying the pump wavelength the average power threshold has been determined for the spectral region of interest of the nonlinear optics experiments. As shown in Fig. B.7.b, this threshold is wavelength dependent and it decreases from $\sim 1.2\mu\text{W}$ to $\sim 0.3\mu\text{W}$ as the wavelength becomes longer.

Based on these results, the SHG experiments have been carried out by carefully controlling the powers travelling inside the detection system. To this purpose the output power of the residual fundamental signal transmitted by the sample (configuration “2” in Fig. B.7.a) has been estimated as

$$P_{out}^{WG} = P_{in} T_{obj}^2 10^{-\frac{\alpha}{10}} \quad (\text{B.3.2})$$

where α is the coupling loss coefficient measured for every particular waveguide.

Therefore, the SHG experiments have been performed by keeping the power transmitted by the sample (P_{out}^{WG}) sufficiently lower the half of the threshold. In this way the experimental error in the estimation of the power threshold has been taken into account. Furthermore, the P_{out}^{WG} power has been also controlled by using an incident power P_{in} at the input objective lower than the input power P_{in} over which the spurious signal has been detected. This is a further precaution that has been taken especially in case of uncertainty on the coupling loss coefficient α .

B.4 Conversion factor from a.u. to Watts

The calibration of the FTIR in absolute power units has been fulfilled by estimating the conversion factor from arbitrary units to Watts in the spectral range of interest by acquiring the spectrum of a radiation source with known power.

Both beams of the OPA operating in single beam emission have been used as tunable calibrated input source. Due to the presence of internal gains of the LIA and the InSb detector of the FTIR, the calibration has been carried out by setting the detection system with the same parameters used in the nonlinear optical experiments.

By varying the power of the input beam at the entrance windows of the FTIR, the corresponding spectrum has been acquired and subsequently corrected with the spectral response of the detection system. In this way, the linear dependence of the spectrum peak intensity on the input power has been constructed (Fig. B.8.a) and the conversion factor has been evaluated as the slope of the linear fit.

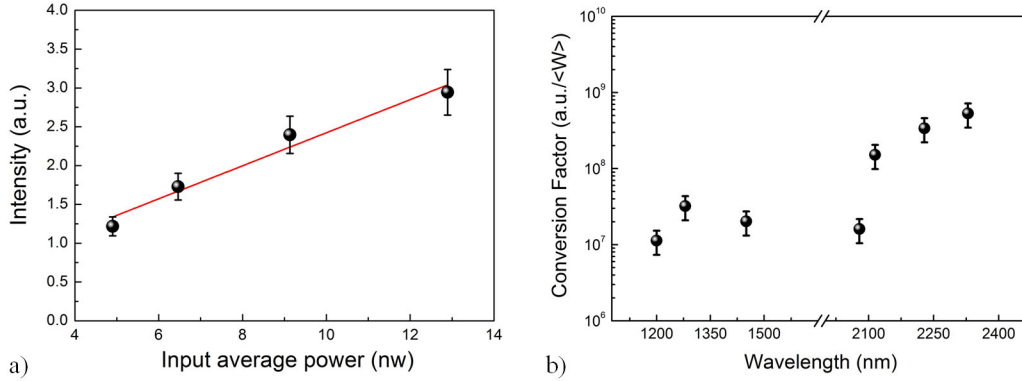


Figure B.8: Conversion factor determination: a) spectrum peak intensity (dots) as a function the input average power measured at 2115 nm. The conversion factor has been estimated as the slope of the linear fit (red line); b) conversion factor as a function of the wavelength.

Although the calibration has been accomplished in fs-pulsed regime, because of the limited temporal resolution of the detection system is sensitive to the average power of the input beam, the conversion factor is given in arbitrary unit per average power Watts units (a.u./<W>).

Due to the broad spectral range involved in the nonlinear optical experiments, the dispersion of the conversion factor has been also studied. As shown in Fig. B.8.b, the conversion factor exhibits an approximatively constant value for wavelengths shorter than 2100 nm, whereas for longer wavelengths an increase of about one order on magnitude, as a consequence of the rise of the FTIR internal optical path transmission.

Appendix C

Experimental characterization of the principal optical elements

In addition to the calibration of the laser source and detection system, the characterization of the principal optical elements constituting the experimental set-up of the nonlinear optics experiments have been performed. The tested elements are the reflective filters and objectives.

Since the control of the laser power has been achieved by reflective filters, their optical densities have been experimentally verified with a spectrophotometer, that is in a low-power-continuous regime, and with the OPA's beams to test them in a condition of high-power-pulsed pumping.

Due to the necessity of a low loss coupling and the selective excitation and collection of the light from a single waveguide, an efficient coupling system has been investigated. As the laser beam has been focused into the waveguide in free space, proper objectives have been selected. Thanks to their particular optical properties, reflective objectives are good candidates. Therefore, their performances have been tested and compared to those of standard microscope objectives.

C.1 Neutral optical filters characterization

During the nonlinear optics experiments the power of the laser source beam has been varied by means of neutral reflective filters. The value of the optical density (OD) has been tested both in conditions of low power continuous regime and in pulsed regime combined with very high peak power due to the ultrashort pulses of the used laser source.

In condition of low power and continuous regime, the optical density values have been extracted from the absorbance measurements carried out with a spectrophotometer covering the spectral range of interest. Instead, the filters OD have been verified in pulsed-high-power regime through the transmittance measurements of the OPA's beams.

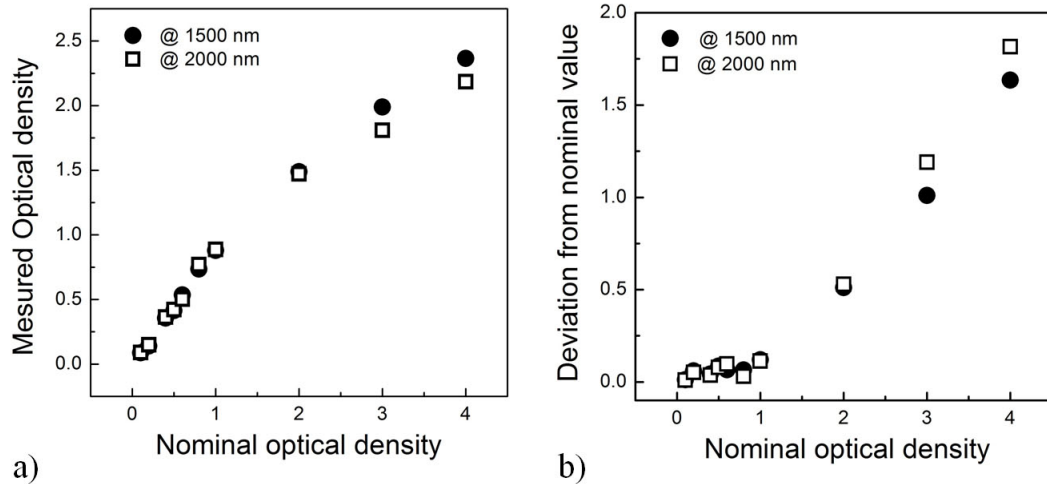


Figure C.1: Optical densities of neutral reflective filters characterization: a) optical densities measured at 1500 nm (solid dot) and 2000 nm (open square). The error bars are smaller than symbols; b) deviation of the measured OD from the nominal values at 1500 nm (solid dot) and 2000 nm (open square).

The obtained values are independent on the investigated regimes within the experimental error bar. Therefore, they have been averaged. A very weak dependence on the wavelength has been found as well as a significant deviation from the nominal

values (Fig. C.1.a). In particular, the differences from the nominal values can be considered negligible for ODs < 1 , but they rise as the ODs become higher (OD > 1) reaching a maximum discrepancy of 18 dB in case of nominal OD = 4 (Fig. C.1.b).

Hence, the average power attenuated by the filters has been estimated by assuming the OD values extracted experimentally.

C.2 Reflective objective characterization

Thanks to their unique optical properties, the reflective objectives have applications in many research areas, such as FTIR spectroscopy, photolithography, laser drilling and etching or laser pumping. In fact, compared to the standard refractive objectives, these objectives offer many advantages. For example, they possess longer working distance relative to the magnification, larger numerical apertures and coating to enhance the performance at specific spectral region. Nevertheless, the most significant property is represented by their total achromatism, which is a relevant characteristic when dealing with signals with very different wavelengths. In fact, due to their flexible optical system, the primary aberrations (spherical aberration, coma and astigmatism) are corrected from the deep-ultraviolet to the far-infrared. Furthermore, their high damage threshold makes these objectives good candidates for dealing with powerful laser source, such as the one used in this thesis.

A reflective objective consists of a small diameter *primary* mirror, held in position by a spider mount and a large diameter *secondary* mirror with a center aperture. The most common configuration is the Schwarzschild-type, where the mirrors are one convex and one concave with coincident centers (Fig. C.2.a). In paraxial approximation the system might be considered equivalent to a thin lens located at the center of curvature of the two mirrors with focal length equal to $f = (R_1 R_2) / [2(R_1 - R_2)]$ [127]. However, this assumption becomes invalid when in the optimization process the radii are slightly changed from the theoretical values. In fact, the op-

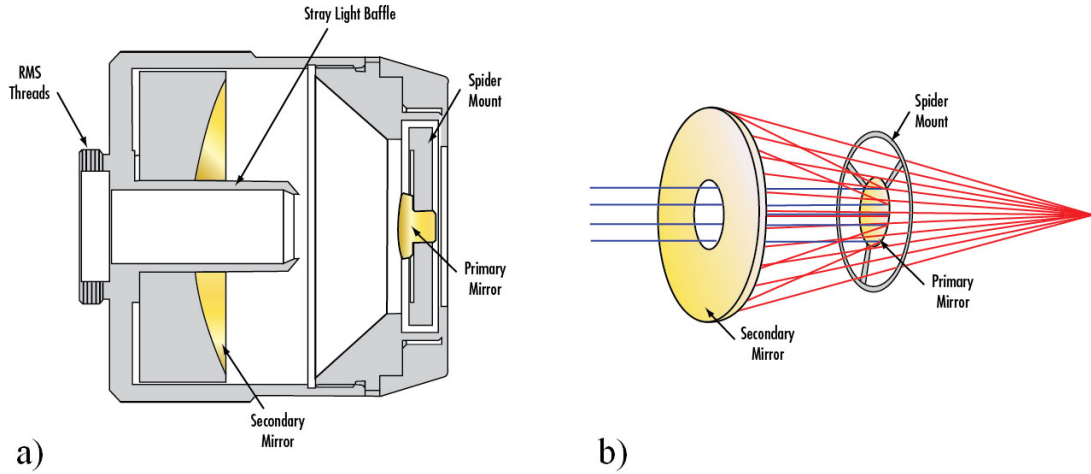


Figure C.2: Reflective objectives: a) anatomy of a reflective objective in Schwarzschild configuration; b) infinity-corrected reflective objective design [126].

tical properties are mainly determined by the radii of the two mirrors and their separation.

The reflective objectives used in this thesis have been in infinity-corrected configuration (Fig. C.2.b), i.e. a collimated light enters the objective through the aperture in the secondary mirror and is focused at a specified working distance. This design represents an efficient solution when the focusing of a collimated broadband or multiple laser sources to a single point is required.

Thanks to aberrations suppression these objectives are also potentially suitable for a tight focusing of a gaussian beam. In fact, although theoretically the beam radii obtained after the focalization by a reflective and refractive objective are similar in condition of high magnification (Fig. C.3), in case of standard microscope objectives the presence of aberrations may cause a deviation from the theoretical focalized spot size and the introduction of beam distortions due to the dispersive material of the lenses composing the objective.

Since a selective excitation and collection of the light from a single waveguide and the lowest possible coupling loss coefficient are necessary for an efficient experiment, the performances of reflective objectives have been compared to those of standard

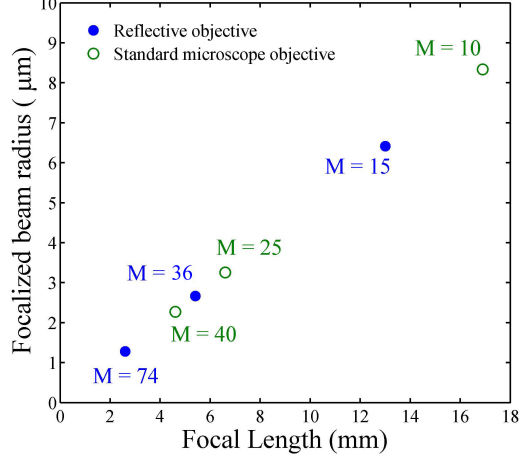


Figure C.3: Comparison of the focalized beam radius (w_f) theoretically calculated as $w_f = (\lambda f M^2)/(\pi w_i)$ assuming a collimated gaussian beam with diameter equal to the primary mirror diameter, i.e. $2w_i = 3$ mm, a laser quality factor $M^2 = 1.5$ and beam wavelength of 1500 nm for several objectives. The considered objectives are refractive objectives (green open dots) with magnification factor M and numerical aperture equal to $10\times/0.25$, $25\times/0.50$ and $40\times/0.65$ and reflective objectives (blue solid dot) with magnification factor M and numerical aperture equal to $15\times/0.28$, $36\times/0.50$ and $74\times/0.65$.

microscope objectives. For this purpose, measurements of insertion losses have been accomplished by making use of different combination of launch and collection objectives, whose technical specifications are listed in Table C.1.

A diode laser (LMP1550-05E, Newport Corp.) emitting an elliptical beam at 1550 nm with fixed power of 5 mW has been coupled into 10 μm wide and 2 mm-long waveguides and the transmitted light has been detected by a germanium photodetector (PH20-Ge, Gentec Electro-Optics Inc.). The tested couples of objectives have been $10\times/40\times$, $25\times/40\times$, $40\times/40\times$ and $74\times/74\times$, where the first magnification value refers to the launch objective and the second one to the collection objective. A pinhole with diameter of about 2 mm has been also included after the collection objective to limit the light detection to the area around the waveguide.

The measurements have been consisted in quantifying the insertion losses when the waveguide has been accurately aligned with respect to the coupled objectives

	M	NA	f (mm)	WD (mm)
Refractive objectives	10×	0.25	16.9	6.80
	25×	0.50	6.6	1.30
	40×	0.65	4.6	0.47
Reflective objectives	74×	0.65	2.6	2

Table C.1: Technical specifications of the tested objectives, where M is the magnification, NA is the numerical aperture, f is the focal length and WD is the working distance. The refractive objectives are from Melles Griot and the reflective objective from Davin Optronics (model 5007-000).

(situation WG) and when it has been moved to the left and right sides and up and down (situations LT , RT , UP , $DOWN$) of about $20 \mu\text{m}$ relative to the position of maximum alignment with the objectives (Fig. C.4).

As shown in Fig. C.5.a, the insertion losses measured with an accurate waveguide alignment with respect to the objectives for the combination $10\times/40\times$ are 10 dB higher than the other pairs of objectives, that have instead similar values. This result indicates that due to the limited power of focusing of the $10\times$ objective a poor coupling of the light into the waveguide occurs. In fact, if the conditions RT and LT are compared to WG , the insertion losses have similar values (Fig. C.5.b). This means that the presence of guided light into the waveguide has only a weak contribution and thus, the same amount of light is measured when the waveguide is not present.

On the other hand, when the couples $25\times/40\times$, $40\times/40\times$ and $74\times/74\times$ are considered, the insertion losses decrease to about 14 dB when the waveguide is aligned, indicating an increase of the guided light into the waveguide (Fig. C.5.a). In fact, when the waveguide is moved to the left or right side, the insertion losses are about 12 dB higher for the combination $25\times/40\times$ and $40\times/40\times$ and 17 dB in case of the couple $74\times/74\times$ (Fig. C.5.b).

When the waveguide has been down shifted, the insertion losses for the couple

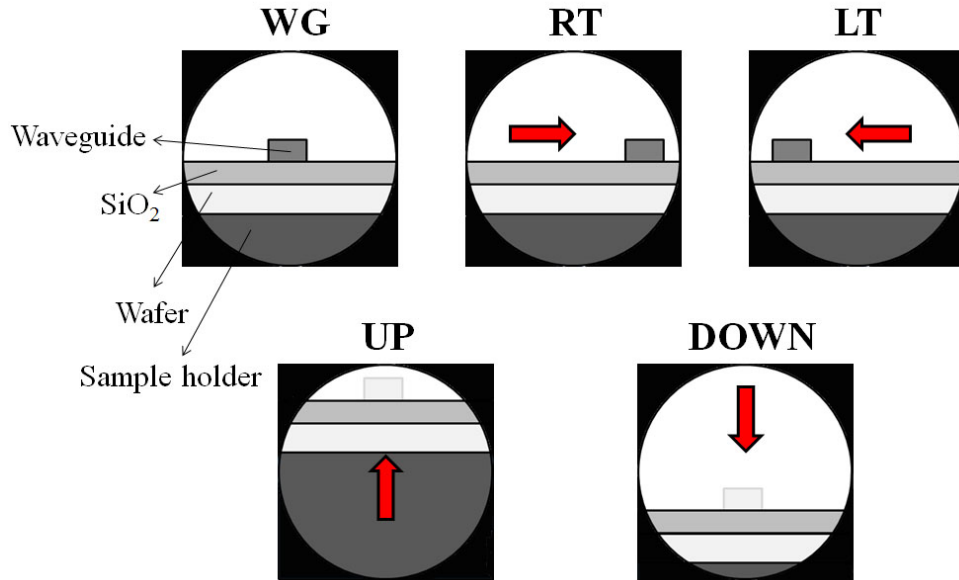


Figure C.4: Insertion losses measurement description: the insertion losses have been quantified for accurate waveguide alignment with respect to the coupled objectives (situation *WG*) and for a $\sim 20 \mu\text{m}$ misalignment to the left (*LT*) and right (*RT*) sides and up (*UP*) and down (*DOWN*) relative to the situation *WG*. The sketches are not to scale.

$74\times/74\times$ has not been affected, whereas more light has been collected when the $25\times$ and $40\times$ objectives have been used at the waveguide input causing a 5 dB increase of the the insertion losses (Fig. C.5.b). Interestingly, when the waveguide has pushed up (data available only for $25\times/40\times$ and $40\times/40\times$ combinations), a further decrease of the insertion losses have been found (Fig. C.5.b). This may be explained by the fact that part of the input light has been transmitted by the silicon wafer.

The overall performances of the investigated objectives pairs is assessed through the contrast parameter, which is defined as the difference between the insertion losses in presence of the waveguide and the averaged values when the waveguide has been pushed to left and right side. This parameter quantifies how selective and efficient is the coupling of the objectives with the waveguide, i.e. how much light that is not transmitted by the waveguide may be collected.

As shown in Fig. C.5.c, the contrast is an approximatively zero when the $10\times$

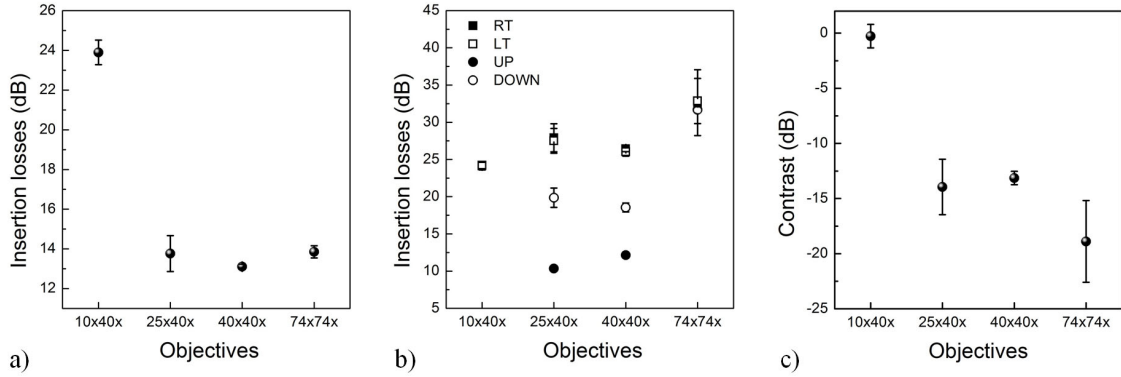


Figure C.5: Insertion losses measurement results: a) the insertion losses quantified for perfect waveguide alignment with respect to the coupled objectives (situation *WG*); b) for a $\sim 30 \mu\text{m}$ misalignment to the right *RT* (solid square) and left *LT* (open square) sides and up *UP* (solid circle) and down *DOWN* (open circle) relative to the situation *WG*; c) contrast parameter as a function of the investigated objective pairs.

objectives is at the input facet of the waveguide and rises with the increase of the magnification to a maximum of -20 dB in case of the reflective objectives. This high contrast may be explained by the fact that, on the contrary with respect the refractive objectives, the reflective objectives combine the high magnification, that limits the light collection from a smaller area, with a much longer working distance. As a result, the contribution of light that is not guided by the waveguide is significantly reduced.

Based on these results, the reflective objectives have been adopted in the non-linear optics experiments for the coupling of the pulsed laser with the waveguides.

Reflective objectives transmittance

In order to estimated the coupled and emitted power from a waveguide, the transmittance value of the reflective objectives has been necessary. Therefore, transmission characterization has been carried out for the range of wavelengths of interest. As shown in Fig C.6, the measured transmittance of a single objective shows a wavelength dependence. It is about 45% in the spectral region of the second harmonic signal and ranges from a minimum of about 25% at 2080 nm to a maximum of about

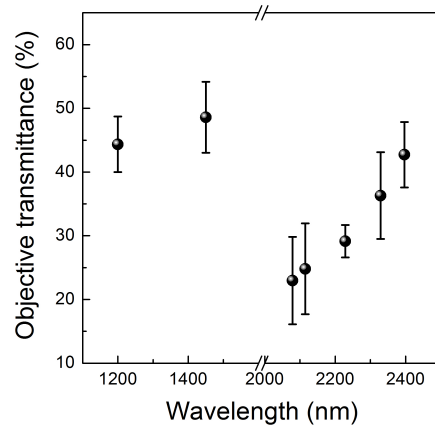


Figure C.6: Reflective objective transmittance as a function of the wavelength.

45% at 2400 nm in the wavelengths region of the fundamental signal.

Bibliography

- [1] Pavesi L. and D. J. Lockwood, *Silicon Photonics*, Springer Ed. (2004)
- [2] Lockwood D. J. and Pavesi L., *Silicon Photonics II: component and integration*, Springer Ed. (2011)
- [3] Liang D. and Bowers J. E., *Nature Photon.* **4**, 511-517 (2010)
- [4] Reed G. T., Mashanovich G., Gardes, F. Y. and Thomson D. J., *Nature Photon.* **4**, 518-526 (2010)
- [5] Michel J., Liu, J. and Kimerling L. C., *Nature Photon.* **4**, 527-534 (2010)
- [6] Leuthold J., Koos C. and Freude W., *Nature Photon.* **4**, 535-544 (2010)
- [7] Soref R., *Nature Photon.* **4**, 495-497 (2010)
- [8] Liu, X. Osgood, R. M. Jr, Vlasov, Y. A., Green, W. M. J., *Nature Photon.* **4**, 557-560 (2010)
- [9] Zlatanovic S. et al., *Nature Photon.* **4**, 561-564 (2010)
- [10] Jalali B., *Nature Photon.* **4**, 506-508 (2010)
- [11] Hochberg M. and Baehr-Jones T., *Nature Photon.* **4**, 492-494 (2010)
- [12] Claps R., Dimitropoulos D., Han Y. and Jalali B., *Opt. Express* **10**, 1305-1313 (2002)

- [13] Lin Q., Painter O. J. and Agrawal G. P., *Opt. Express* **15**(25), 16604-16644 (2007)
- [14] Dinu M., Quochi F. and Garcia H., *Appl. Phys. Lett.* **82**, 2954-2956 (2003)
- [15] Espinola R., Dadap J., Osgood R. Jr, McNab S. and Vlasov Y., *Opt. Express* **12**, 3713-3718 (2004)
- [16] Liu A., Rong H., Paniccia M., Cohen O. and Hak D. Net, *Opt. Express* **12**, 4261-4267 (2004)
- [17] Xu Q., Almeida V. and Lipson M., *Opt. Express* **12**, 4437-4442 (2004)
- [18] Sih V. et al., *Opt. Express* **15**, 357-362 (2007)
- [19] Raghunathan V., Borlaug D., Rice R. R., Jalali B., *Opt. Express* **15**, 14355-14362 (2007)
- [20] Boyraz O. and Jalali B., *Opt. Express* **12**, 5269-5273 (2004)
- [21] Rong H. et al., *Nature Photon.* **1**, 232-237 (2007)
- [22] Pavesi L., Dal Negro L., Mazzoleni C., Franzo G. and Priolo F., *Nature* **408**, 440-444 (2000)
- [23] Anopchenko A., Tengattini A., Marconi A., Prtljaga N., Ramírez J. M., Jambois O., Berencén Y., Navarro-Urrios D., Garrido B., Milesi F., Colonna J.-P., Fedeli J.-M. and Pavesi L., *J. Appl. Phys.* **111**, 063102 (2012)
- [24] Dekker R., Driessen A., Wahlbrink T., Moormann C., Niehusmann J. and M. Först, *Opt. Express* **14**, 8336-8346 (2006)
- [25] Dulkeith E., Vlasov Y. A., Chen X., Panoiu N. C. and Osgood R. M. Jr., *Opt. Express* **14**, 5524-5534 (2006)
- [26] Boyraz O., Indukuri T. and Jalali B., *Opt. Express* vol. 12, pp. 829- 834 (2004)

- [27] Hsieh I.-W., Chen X., Liu X., Dadap J. I., Panoiu N. C., Chou C. Y., Xia F., Green W. M., Vlasov Y. A. and Osgood R. M. Jr., *Opt. Express* **15**, 15242-15249 (2007)
- [28] Yin L., Lin Q. and Agrawal G. P., *Opt. Lett.* **32**, 391-393 (2007)
- [29] Foster M. A. et al, *Nature* **441**, 960-963 (2006)
- [30] Liu X., Osgood R. M., Vlasov J. A. and Green W. M. J., *Nature Photon.* **4**, 557-560 (2010)
- [31] Fukuda H., Yamada K., Shoji T., Takahashi M., Tsuchizawa T., Watanabe T., Takahashi J. and Itabashi S., *Opt. Express* **13**, 4629-4637 (2005)
- [32] Rong H., Kuo Y. H., Liu A., Paniccia M. and Cohen O., *Opt. Express* **14**, 1182-1188 (2006)
- [33] Lin Q. , Zhang J., Fauchet P. M. and Agrawal G. P., *Opt. Express* vol. **14**, 4786-4799 (2006)
- [34] Foster M. A, Turner A. C., Salem R., Lipson, M. and Gaeta A. L., *Opt. Express* **15**, 12949-12958 (2007)
- [35] Arghavani R. et al. *IEEE Trans. Electron Devices* **51**, 1740 (2004)
- [36] Sun Y., Sun G., Parthasarathy S. and Thompson S. E., *Mater. Sci. Eng. B* **135**, 179 (2006)
- [37] Ungersboeck E., Dhar S., Karlowatz G., Sverdlov V., Kosina H. and Selberherr S., *IEEE Trans. Electron Devices* **54**, 2183 (2007)
- [38] Ma F., Zhang T. W., Xu K. W. and Chu P. K. *Appl. Phys.Lett.* **98**, 191907 (2011)
- [39] Rim K. et al., *Solid-State Electronics* **47**, 1133-1139 (2003)

- [40] Schriever C., Bohley C., Schilling J. and Wehrspohn R. B., *Materials* **5**, 889-908 (2012)
- [41] Lea E. and Weiss B. L., *Electron. Lett.* **32**, 1577 (1996)
- [42] Jacobsen R. S., Andersen K. N., Borel P. I., Fage-Pedersen J., Frandsen L. H., Hanses O., Kristensen M., Lavrinenko A. V., Moulin G., Ou H., Peucheret C., Zsigri B. and Bjarklev A., *Nature* **441**, 199 (2006)
- [43] Chmielak B., Waldow M., Matheisen C., Ripperda C., Bolten J., Wahlbrink T., Nagel M., Merget F. and Kurz H. *Opt. Express* **19**, 17212 (2011)
- [44] Vanzetti L., Barozzi M., Giubertoni D., Kompocholis C., Bagolini A. and Bellutti P., *Surf. Interface Anal.* **38**, 723 (2006)
- [45] Master Thesis, E. Borga, *Second Harmonic Generation in Strained Silicon Waveguides*, University of Trento (2009)
- [46] Temple-Boyer P., Rossi C., Saint-Etienne E. and Scheid E., *J. Vac. Sci. Technol. A* **16**, 2003 (1998)
- [47] Landau L. D. and Lifshitz E. M. , *Theory of Elasticity*, Course of Theoretical Physics, Volume 7, Second Edition, Pergamon Press, Chap. 1 (1970)
- [48] Wortman J. J. and Evans R. A., *J. Appl. Phys.* **36**, 153 (1965)
- [49] Reddy J. N., *An Introduction to Continuum Mechanics*, Cambridge University Press, Chap. 6 (2007)
- [50] Auciello O., Krauss A. R., *In Situ Real-Time Characterization of Thin Films*, John Wiley & Sons Inc., Chap. 7 (2000)
- [51] Mittal K. L., *Adhesion Aspects of Thin Films*, Volume 1, VSP - An imprint of BRILL, Chap. 1 (2001)

- [52] Laconte J., Flandre D. and Raskin J. P., *Micromachined thin film sensor for SOI CMOS*, Springer, Chap.2 (2006)
- [53] Tu K. N., *Electronic thin-film reliability*, Cambridge University Press, Chap. 6 (2011)
- [54] Jones B. K. and Zhigal'skii G. P., *Physical Properties of Thin Metal Films*, CRC Press, Chap. 4 (2003)
- [55] Kobeda E. and Irene A., *J. Vac. Sci. Technol B* **4** (3), 720 (1985)
- [56] Toivola Y., Thurn J., Cook R. F. Cibuzar G. and Roberts K., *J. Appl. Phys.*, **94** (10), 6915-6922 (2003)
- [57] Tien C.L. and Lin T.W., *Applied Optics*, **51** (30), 7229-7235 (2012)
- [58] Morin P., Raymond G., Benoit D., Maury P. and Beneyton R., *Applied Surface Science* **260**, 69-72 (2012)
- [59] Claassen W., Valkenburg W., Wijgert W. and Willemsen M., *Thin Solid Films* **129**, 239-247 (1985).
- [60] Ohring M., *The materials science of thin films*, Academic Press, Chap. 9 (1992)
- [61] Maa C.-H., Huangb J.-H., Chena H., *Thin Solid Films* **418**, 73-78 (2002)
- [62] Yu P. Y. and Cardona M., *Fundamental of semiconductors*, Chap. 7 (2010)
- [63] Ganesan S., Maradudin A. A. and Oitmaa J., *Ann. Phys.* **56**, 556 (1970)
- [64] Loudon R., *Adv. Phys.* **13**, 423 (1964)
- [65] Cerdeira F., Buchenauer C. J., Pollak F. H. and Cardona M., *Phys. Rev. B* **5**, 580 (1972)
- [66] De Wolf I., Maes H. E. and Jones S. K., *J. Appl. Phys.* **79** (9), 7148 (1996)

- [67] Bianco F., Fedus K., Enrichi F., Pierobon R., Cazzanelli M., Ghulinyan M., Pucker G. and Pavesi L., *Semicon. Sci. Technol.* **27**, 085009 (2012)
- [68] De Wolf I., *Semicond. Sci. Technol.* **11**, 139 (1996)
- [69] Becker M., Scheel H., Christiansen S. and Strunk H. P., *J. Appl. Phys.* **101**, 063531 (2007)
- [70] WITec Focus Innovation, Product Catalogue, www.witec.de
- [71] McSkimin H. J., Bond W. L., Buehler E. and Teal G. K., *Phys. Rev* **83**, 1080 (1951)
- [72] Zuckervan A., *J. Acoust. Soc. Am.* **54**, 699 (1973)
- [73] McSkimin H. J. and Andreatch Jr. P. J., *J. Appl. Phys.* **35**, 2161 (1964)
- [74] Anastassakis E., Cantarero A. and Cardona M., *Phys. Rev. B* **41**, 7529 (1990)
- [75] Srikar V. T., Swan A. K., Ünlü M. S., Goldberg B. B. and Spearing S. M., *J. Microelectromech Syst.* **12**, 779 (2003)
- [76] Harris S. J., O'Neill A. E., Yang W., Gustafson P., Weber W. H., Majumdar B. and Ghosh S., *J. Appl. Phys.* **96**, 7195 (2004)
- [77] Miyatake T. and Pezzotti G., *J. Appl. Phys.* **110**, 093511 (2011)
- [78] Chandrasekhar E., Renucci J. B. and Cardona M., *Phys. Rev. B* **17**, 1623 (1978)
- [79] Narayanan S., Kalidindi S. R. and Schadler L. S., *Appl. Phys.* **82**, 2595 (1997)
- [80] Jain S. C., Harker A. H., Atkinson A. and Pinardi K., *J. Appl. Phys.* **78**, 1630 (1995)
- [81] Boyd R. W., *Nonlinear optics*, Third Edition, Academic Press, Chap. 1, 2 (2007)

- [82] Ebrahimzadeh M., *Phil. Trans. R. Soc. Lond. A* **361** (1813), 2731-2750 (2003)
- [83] Sutherland R. L., *Handbook of nonlinear optics*, Second Edition, CRC Press, Chap. 1, 2 (2003)
- [84] Hum D. S. and Fejer M. M., *C. R. Physique* **8**, (2007)
- [85] Butcher P. N. and Cotter D., *The elements of nonlinear optics*, Cambridge University Press, Chap. 7 (1990)
- [86] Tom H. W. K., Heinz T. F. and Shen R. F., *Phys. Rev. Lett.* **51**(21) (1983)
- [87] Govorkov S. V., Emel'yanov V. I., Koroteev N. I., Petrov G. I., Shumay I. L. and Yakolev V. V., *J. Opt. Soc. Am. B* **6**, 1117-1124 (1989)
- [88] Zhao Ji-H., Chen Q-D, Chen Z-G, Jia G., Su W., Jiang Y., Uan Z-X, Dolgova T. V., Aktsipetrov O.A. and Sun H-B., *Opt. Lett.* **34**, 3340-3342 (2009)
- [89] Schriever, C., Bohley, C. and Wehrspohn, R. B., *Opt. Lett.* **35**, 273-275 (2010)
- [90] Mitchell S. A., Mehendale M., Villeneuve D. M. and Boukherroub R., *Surf. Sci.* **488**, 367-378 (2001)
- [91] Govorkov S. V. , Koroteev N. I., Petrov G. I., Shumay I. L. and Yakolev V. V., *Appl. Phys. A* **50**, 439-443 (1990)
- [92] Huang, *Jpn. J. Appl. Phys.* **33**, 3878-3886 (1994)
- [93] Bloembergen N., *Appl. Phys. B* **68**, 289-293 (1999)
- [94] Sipe J. E., Moss D. J. and van Driel H. M., *Phys. Rev. B* **35**(3) (1987)
- [95] Shen Y. R., *Ann. Rev. Phys. Chem.* **40**, 327 (1989)
- [96] Hienz T. F. in: Ponath H.-E and Stegeman G. I., *Nonlinear surface electromagnetic phenomena*, Elsevier, Chap. 5 (1991)

- [97] Lüpke G., *Surf. Sci. Rep.* **35**, 75 (1999)
- [98] Mitchell S. A., Boukherroub R. and Anderson S., *J. Phys. Chem. B* **104**,7668 (2000)
- [99] Dadap J. I., Xu Z., Hu X. F., Downer M. C., Russell N.M., Ekerdt J. G. and Aktsipetrov O. A., *Phys. Rev. B* **56**, 13367 (1997)
- [100] Höfer U., *Appl. Phys. A* **63**, 533 (1996)
- [101] Pedersen K. and Morgen P., *Phys. Rev. B* **53**, 9544 (1996)
- [102] Lyubchanskii I. L., Dadoenkova N. N., Lyubchanskii M. I., Rasing Th., Jeong J.-W. and Shin S.-C., *Appl. Phys. Lett.* **76**(14) (2000)
- [103] Cazzanelli M., Bianco F., Borga E., Pucker G., Ghulinyan M., Degoli E., Luppi E., Véniard V., Ossicini S., Modotto D., Wabnitz S., Pierobon R. and Pavesi L., *Nature Materials* **11**, 148-154 (2012)
- [104] Fejer M. M., Magel G. A., Jundt D. H. and Byer R. L., *IEEE J. Quantum Electron.* **28**, 2631-2654 (1992)
- [105] Liu X., Qian L. J. and Wise F. W., *Phys. Rev. Lett.* **82**, 4631-4634 (1999)
- [106] Levy J. S., Foster M. A., Gaeta A. L. and Lipson M., *Opt. Express* **19**, 11415 (2011)
- [107] Lettieri S., Finizio S. D., Maddalena P., Ballarini V. and Giorgis F., *Appl. Phys. Lett* **81** (25), 4706-4708 (2002)
- [108] Descrovi E., Ricciardi C., Giorgis F., Léron del G., Blaize S. Pang C. X., Bachelot R., Royer P., Lettieri S., Gesuele F., Maddalena P. and Liscidini M., *Opt. Express* **15**(7), 4159-4167 (2007)
- [109] Logan D. F., Alamin Dow A. B., Stepanov D., Abolghasem P., Kherani N. P. and Helmy A. S., *Appl. Phys. Lett.* **102**, 061106 (2013)

- [110] Aberle A.G., *Solar Energy Materials and Solara Cells* **65**, 239-248 (2001)
- [111] Nasu H., Okamoto H., Kurachi K., Matsuoka J., Kamiyaitions K., Mito A. and Hosono H., *J. Opt. Soc. Am. B* **12**(4), 644-649 (1995)
- [112] Quiquempois Y., Martinelli G., Duthe'rage P., Bernage P., Niay P. and Douay M., *Optics Communications* **176**, 479-487 (2000)
- [113] Omenetto F. G., Taylor A. J., Moores M. D., Arriaga J., Knight J. C., Wadsworth W. J. and Russell P. S. J., *Opt. Lett.* **26**(15), 1158-1160 (2001)
- [114] Moutzouris K., Venugopal Rao S., Ebrahimzadeh M., De Rossi A., Calligaro M., Ortiz V. and Berger V., *Appl. Phys. Lett.* **83**, 620-622 (2003)
- [115] Oster B. and Fouckhardt H., *Appl. Phys. B* **73**, 535-540 (2001)
- [116] Van der Ziel J. P., Miller R. C., Logan R. A., Nordland W. A. Jr and Mikulyak R. M., *Appl. Phys. Lett.* **25**, 238-240 (1974)
- [117] Hon N. K., Tsia K. K., Solli D. R. and Jalali B., *Appl. Phys. Lett.* **94**, 091116 (2009)
- [118] Taira Y., Kita T., Teraoka E. Y. M. and Yamada H., *Jpn. J. Appl. Phys.* **51**, 04DG04, (2012)
- [119] Goldsmith P. F., *Quasioptical Systems*, IEEE Press. (1998)
- [120] Siegman A. E., *Lasers*, University Science Books, Mill Valley, CA, Chap. 17 (1986)
- [121] Ligth Conversion, Product Datasheet, www.lightcon.com
- [122] Spectra Physics (Division of Newport Corporation), Product Datasheet, www.newport.com/lasers
- [123] Lindermeir E., Haschberger P., Tank V. and Dietl H., *Appl. Opt.* **31** (22), 4527 (1992)

- [124] Tank V., *Infrared Phys.* **29**, 209-210 (1989)
- [125] Vastag B. J. and Hormann S. R., *International Conference on Fourier Transform Infrared Spectroscopy*, H. Sakai ed., Proc. Soc. Photo-Opt. Instrum. Eng. **289**, 74-79 (1981)
- [126] Edmund Optics, *Introduction to reflective objectives*, Learning and Support, www.edmundoptics.com
- [127] Bollanti S., Di Lazzaro P., Flora F., Mezi L., Murra D. and Torre A., *Appl. Phys. B* **85**, 603-610 (2006)